

DESIGN AND
IMPLEMENTATION OF A
COAXIAL LASER
TRIANGULATION SENSOR IN A
LASER METAL DEPOSITION
SET-UP

M.Sc. Thesis

Wouter Bos

February 26, 2021

UNIVERSITY OF TWENTE.

Design and implementation of a coaxial laser triangulation sensor in a laser metal deposition set-up

Faculty of Engineering Technology

Master Thesis

In fulfillment of the requirements for the degree of Master of Science in Mechanical Engineering

15th of march 2021

Author:

W. Bos

Supervisor:

Ir. S.J.L. Bremer

Graduation committee:

Chairman:

Prof.dr.ir. G.R.B.E. Römer

Internal member:

Dr. M. Feinaeugle

External member:

Dr.ir. R.G.K.M. Aarts

Preface

This report presents and discusses the results of my MSc thesis project, investigating the design and implementation of a height sensor to be used in a Laser Material Deposition set-up. This research has been carried out within the Chair of Laser Processing at the University of Twente.

During my investigation I was helped by and received aid from multiple persons. For these reasons I wish to thank my supervisors Leon Bremer and Gert-willem Römer for their aid in answering my questions and providing a different perspective. In addition, I wish to thank Martijn Stok and Leo Tiemersma for their aid in acquiring and testing the used optical components, and the manufacture of some required components. Lastly, I wish to thank Ralph Pohl for his aid in investigating the theoretical basis behind the optics used.

Wouter Bos
February 2021

List of abbreviations

AM	Additive Manufacturing
API	Application Programming Interface
BPP	Beam Parameter Product
CCD	Charge-Coupled Device
CLT	Coaxial Laser Triangulation
CMOS	Complementary Metal Oxide Semiconductor
CNC	Computer Numeric Control
CWL	Centre wavelength
DED	Directed Energy Deposition
DLD	Directed Laser Deposition
DLF	Directed Light Fabrication
FPS	Frames per Second
FWHM	Full Width at Half Maximum
IR	Infrared
LASER	Light Amplification by Stimulated Emission of Radiation
LED	Light Emitting Diode
LENS	Laser Engineered Net Shaping
LMD	Laser Metal Deposition
NA	Not applicable
OCT	Optical Coherence Tomography
PF-LMD	Powder-Fed Laser Metal Deposition
SNR	Signal to Noise Ratio
TLA	Three Letter Acronym
TR	Transmission Ratio
WB-LMD	Wire-Based Laser Metal Deposition
Yb:YAG	Yttrium Aluminium Garnet

Nomenclature

ϵ	Emittance []
θ	Beam divergence [rad]
λ	Wavelength [m]
λ_{probe}	Wavelength of probe laser [m]
σ	Stefan-Boltzmann constant $5.670367 \cdot 10^{-1}$ [$J s^{-1} m^{-2} K^{-4}$]
σ	Standard deviation []
ω	Width of beam [m]
ω_0	Width of beam in focal point [m]
A	Area of melt pool [m^2]
A	Area underneath Gaussian curve []
A	Amplitude of Gaussian curve []
a	Amplitude of Gaussian function []
b	Position of the center of a Gaussian function []
b_k	Offset of probe laser from optical axis [m]
c	Width of Gaussian function []
c	Speed of light 299792458 [$m s^{-1}$]
D_{optic}	Diameter of optic [m]
d	Propagation length [m]
dh	Axial movement caused by movement dS [m]
dS	Sensor pixel size [m]
e_k	Location of projected spot on sensor [m]
f	Focal length of lens [m]
h	Distance from focal point [m]
h	Planck's constant $6.62607004 \cdot 10^{-34}$ [$m^2 k g s^{-1}$]
h_{max}	Maximum distance from focal point achievable
$I(r)$	Power emitted by melt pool at radius r [W]
k_B	Boltzmann constant $1.380649 \cdot 10^{-23}$ [$J K^{-1}$]
M	Magnification of optical system []
M	Ray transfer matrix []
M_{add}	Magnification of telescope []
M_{cam}	Magnification of camera lens []
M^2	Beam quality factor []
N_{angle}	Amount of rays emitted by melt pool []
P	Thermal energy radiated by melt pool [W]
P_{probe}	Power emitted by probe laser [W]
S	Size of sensor [m]
s_k	Location of projected spot on target [m]
T	Transmittance of optical component []
T	Temperature of melt pool [K]
Z_R	Rayleigh range [m]

Summary

During the process known as Laser Metal Deposition (LMD), a stream of powder particles is molten by a laser and deposited on a substrate material forming a "bead". However, the geometry and dimensions of this bead changes due to undesirable environmental disturbances and varying process variables. Therefore, it is desirable to implement a sensor system able to measure some of the changes in the geometry in real-time. One of these geometrical changes is the height of the bead, which can be measured by measuring the distance between the laser processing head, and the deposited bead, known as the axial displacement.

In this thesis, several possibilities for sensors were identified that can be integrated onto the currently existing LMD set-up at the Chair of Laser Processing of the University of Twente. It was chosen to use the method known as Coaxial Laser Triangulation (CLT).

In coaxial laser triangulation a probe beam is "injected" into the optical path of the high-power laser beam, which reflects of the geometry of the bead, and generates an image on the coaxial camera if the axial displacement increases.

Over the course of the research, the CLT sensor method was implemented on the existing laser processing setup. In support of this, multiple models were created to examine the behaviour of the sensor. This included: a geometrical model, an optical transmittance model, and a ray tracing model. Using these models, an implementation of this sensor was designed. Next the sensor was implemented, and experiments were performed using this implementation.

From the results gathered, it was concluded that the created models were relatively accurate however, the behaviour of a diaphragm remained problematic. Furthermore, using the current implementation, the stated accuracy requirement of ± 0.1 mm could not be met, and a maximum accuracy, in ideal conditions, of $\pm 0.2-0.3$ mm was achieved. While in non-ideal conditions, an accuracy of $\pm 0.6-0.7$ mm was reached.

Overall, the final recommendations were to redesign the system to improve the overall rigidity, axial resolution, and accuracy. This would be done by replacing the probe laser, camera, and optical tubing. Based on these aspects, it will be possible to meet the requirements.

Table Of Contents

Preface	i
List of abbreviations	iii
Nomenclature	v
Summary	vii
1 Introduction	1
1.1 Background	1
1.2 Problem definition	2
1.3 Research objectives	2
1.4 Contents of this report	2
2 State-of-the-art	3
2.1 Triangulation based sensors	3
2.2 Other contact-less sensors	6
2.3 Control methods	9
2.4 Summary and conclusion	10
3 Concept development and evaluation	11
3.1 Situation sketch	11
3.2 Laser beam diameter	12
3.3 Formulation of Requirements	13
3.4 Proposed Concepts	14
3.5 Concept evaluation	17
4 Design and modelling of a CLT sensor	19
4.1 Design variables	19
4.2 Design and modelling of optics	20
4.3 Design and modelling of probe laser beam and filter	23
4.4 Advanced ray-tracing model	31
4.5 Summary	36
5 Implementation of a CLT sensor	37
5.1 Mechanical implementation	37
5.2 Implementation of image processing	39
5.3 Evaluation of set up	41
6 Experimental results and discussion	45
6.1 Experimental set-ups	45
6.2 List of experiments	47
6.3 Experimental results	51
6.4 Additional processing of sensor output	60
6.5 Practical applications	62
6.6 Discussion	63

7 Conclusion and recommendations	65
7.1 Conclusion	65
7.2 Recommendations	66
Bibliography	68
A Transmission spectra	73
A.1 Experimental set-up	73
A.2 Results	73
B Model results	77
C Technical drawings	79
D Characterising the laser modules	83
D.1 Wavelength spectrum	83
D.2 Beam profile	84
D.3 Analog control signal	86

Chapter 1

Introduction

1.1 Background

For at least the past 50 years, there has been a concerted effort into developing techniques for additive manufacturing (AM) [1]. This is most strikingly seen in the recent rise of commercial and hobby grade 3D printers, that can "print" plastic components using the Fused Filament Fabrication method. Most AM techniques rely on computer numerical control (CNC) technologies to "slice" the computer model of a desired component into thin "slices" and to print the desired geometry layer-by-layer [1].

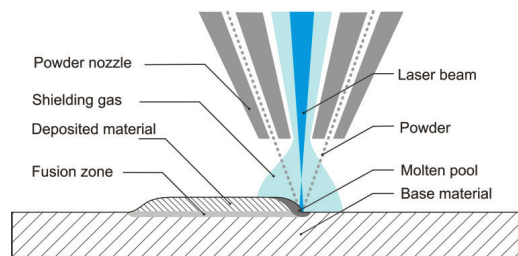


Figure 1.1: A representation of the different aspects of laser metal deposition [2].

Industrially however, the printing of metal components is highly desirable due to the large degree of geometrical freedom such a process can impart [1]. As a result, a large variety of AM processes have been developed for use in the industry, based on a wide variety of methods. According to Thompson et al. [1] one of the first experimental processes in this category was devised by I. Harter in 1942, where a welding electrode was used to deposit multiple layers of metal on top of each other [3]. This line of research was continued in the 1960's and 1970 with the advent of microprocessors and the subsequent rise of CNC machining methods.

However, the creation of the first LASER (Light Amplification by Stimulated Emission of Radiation) in 1960 would also open a different avenue of research [1]. Using directed energy from a laser beam it became possible to accurately melt metals at a certain location, leading to the advent of methods commonly grouped under the overall umbrella of Directed Energy Deposition (DED). The subgroup which relies on the usage of a laser is referred to as Laser Metal Deposition (LMD) which can also be referred to as Laser Engineered Net Shaping (LENS), Direct Laser Deposition (DLD) and Direct Light Fabrication (DLF), and various other three letter acronyms (TLA) [1].

Laser metal deposition itself can also be split into two different types depending on the material supply, the first type adds the material to be deposited in small (powder) particles suspended in the carrier gas (this carrier gas is also used as a shielding gas), called powder-fed LMD (PF-LMD). The second type adds the material to be deposited in wire form, called wire-based LMD (WB-LMD).

Using a PF-LMD process, it is possible to clad a metal powder onto a substrate of a different type, this will allow mixing-and-matching of different material types to realise an optimal cross-section, furthermore, using Laser cladding, it is also possible to repair existing components [1].

1.2 Problem definition

During PB-LMD the stream of metal powder being molten by the laser, which moves relative to the substrate, will result in a moving pool of molten metal, the melt-pool. Since the melt-pool is highly dynamic, as the material is deposited, small perturbations will occur in the geometry of the bead that has been deposited [1]. These perturbations will over the length of the process lead to large deviations from the required geometry of the final part.

When LMD is used for laser cladding, these deviations, if the process parameters have been correctly set, can remain within the desired boundaries. However, if the process parameters are not set correctly, and/or multiple layers are deposited on top of each other, large deviations can occur over time. These deviations are caused by several different effects such as: changes in the momentum of the melt pool due to the powder flow, surface instability of the melt pool due to the particles, internal flow inside the melt pool, or bulk heating effects which change how the melt pool behaves [1].

One of the many avenues of research into this problem is the use of a measuring system combined with a closed-loop controller which adjusts the process variables to correct for these deviations. Over the years many different types of sensors have been proposed. These proposals range from pyrometers measuring the temperature of the melt-pool to a camera to measure the size of the melt pool [4]. However other types of sensor have been proposed dedicated to measuring the geometry of the bead being deposited using: multiple cameras, laser triangulation and various other methods that will be discussed in chapter 2.

In this thesis the type of sensor being proposed is based on measuring the axial displacement between the laser processing head and the melt pool, to be able to use this to control the overall process.

1.3 Research objectives

The scope of the research in this thesis will be limited to the following:

1. Determine what kind of sensors can be used on the current laser set-up at the chair of laser processing of the University of Twente to measure the geometry of the clad below the laser optics, and to determine the best possible solution to implement.
2. Integrate the selected sensor into the experimental set-up.
3. Characterise the selected sensor for a variety of laser processing parameters.

1.4 Contents of this report

In this first chapter of this thesis, the subject will be introduced, and the scope of this thesis will be defined.

In the second chapter a literature survey is presented in the framework of the problem defined in the previous section. In this literature survey, multiple possible solutions from earlier research will be investigated. At the end of the literature survey, a short diversion will be taken into possible control strategies that the investigated type of sensor can be used for.

In the third chapter, the current situation of the experimental set-up will be examined and combined with results from the literature survey to establish a list of requirements that the solution will need to full fill. Furthermore, the literature survey will be used to create possible solutions for the stated problem and to determine the solution best meeting the stated requirements.

In the fourth chapter, a list of design variables will be created using the literature survey. Then using theoretical models, the prospective system is analysed, possible layouts are examined, and an overall design created.

In the fifth chapter, the overall design will be implemented into the existing system by designing the mechanical and software aspects. Then initial tests will be performed to examine the performance of the system.

In the sixth chapter, the implemented solution will be examined using data gathered from multiple experiments. This data will be discussed, and possible adjustments on the set-up will be applied. Furthermore, the overall results from the experiments of the implemented sensor will be discussed.

In the last chapter of this report, an overall conclusion will be drawn, and based on the conclusions recommendations for future research/improvements will be made.

Chapter 2

State-of-the-art

To determine what type of sensors to measure the axial displacement of the bead geometry relative to the laser focusing head, are available to be used in a laser metal deposition set-up, a literature survey is presented and discussed in this chapter. To showcase the results, this chapter has been divided into three sections: the first section will discuss the sensors based on triangulation, the second will discuss various non-triangulation sensors, while the third section is dedicated to showcase some of the control strategies that were implemented using these sensors.

2.1 Triangulation based sensors

Many of the sensors used to measure the geometry during or after the process of LMD, are based on the principle of optical triangulation [5][6][7][8][9]. In this section a general overview of how optical triangulation works will be provided as well as an overview of several methodologies increasing in the amount of data generated, since an overview of all sensors based on optical triangulation falls outside the scope of this document.

2.1.1 Principle

In general, optical triangulation works by projecting light from a laser source (or from a LED in cheaper implementations) and using a sensor sensitive to light (CCD or CMOS, again depending on implementation) to determine the location of the reflected light. The light sensor is placed at an angle relative to the light source, so that when the object is displaced, the projection of the reflection on the optical sensor is displaced as well. This basic geometry used in optical triangulation is shown in figure 2.1. This figure is based on the use of single point optical triangulation, one of the simplest methodologies, and one often used in mechanical positioning systems.

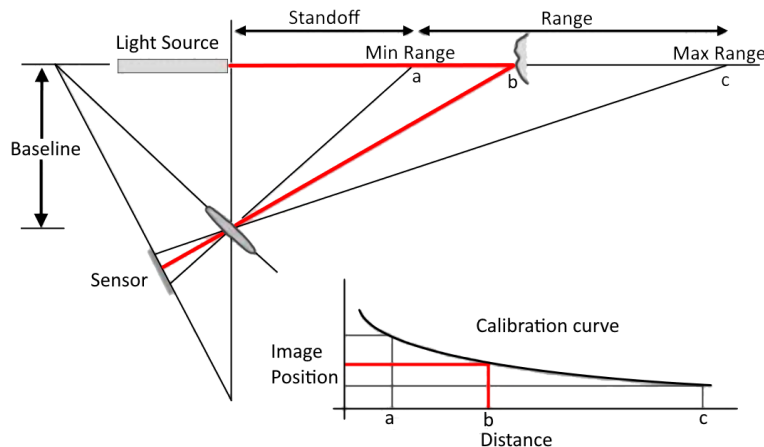


Figure 2.1: A schematic representation of how a 1D triangulation-based sensor measures the displacement [10].

2.1.2 2D implementations

Of course, due to how this method works, it is very easy to extend this use to the projection of a line on the substrate, to extract the height profile along this line. This type of sensor is very common for use in seam-tracking in laser welding [11], an example of this principle extended to omnidirectional can be found in the work of D. Iakovou [12]. In laser metal deposition, this kind of sensor has also found favour for its ability to extract the geometry of the clad track for use in a controller. A example of this can be found in the work of Xing et al. [5] who created a height-based closed-loop controller based on the use of a projected line using a laser source.

Another example of this technique was the work of Heralic et al. [6], who implemented this type of sensor to increase the stability during laser metal wire deposition, which is a variant on the powder-based laser metal deposition, that is used in this thesis. Figure 2.2 shows an example of a set-up using this type of laser displacement sensor. Another variation of this method was implemented by Takushima et al. [7] who instead of a front camera, used the coaxial camera of the laser processing head to measure the displacement of the laser line sensor. A different implementation was reported recently by Tyralla et al. [8] who used two triangulation sensors, manufactured by Falldorf Sensor GmbH, to measure the leading and trailing geometries during deposition.

It must be noted that this kind of sensor can come in different sorts of packages, e.g. separated line projector and camera (see Heralic et al. [6] or Takushima et al. [7]), or an integrated box containing both the LASER and the camera (see the Falldorf sensor used in Tyralla et al. [8] or Römer et al. [11]).

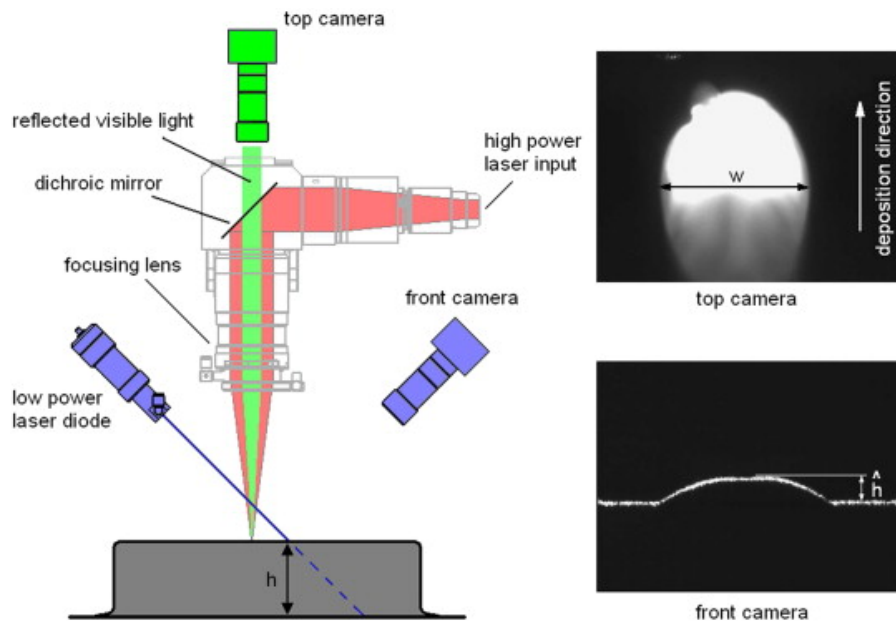


Figure 2.2: Sensor setup for bead height and width measurements using a projected laser line. The height is obtained by observing the shape of the projected laser line with the front camera [6].

2.1.3 3D implementations

As easy as optical triangulation is to implement into a 2D projected line, the same can be done to extend it further to measure the dimensions/geometry an entire 3D plane. This type of sensor has also been used to measure the surface of a part during LMD. In further work of Heralic et al. [9] a 3D scanner, based on sweeping a 2D line, was used between each successive layer of the WB-LMD process to determine the geometry of the resulting surface, and to use that to adapt the next layer to be deposited.

Garmendia et al. [13] [14] used a different approach, they implemented a 3D scanner that projected a structured light pattern instead of a laser, and used the resulting points cloud to determine the geometry after each layer (figure 2.3).

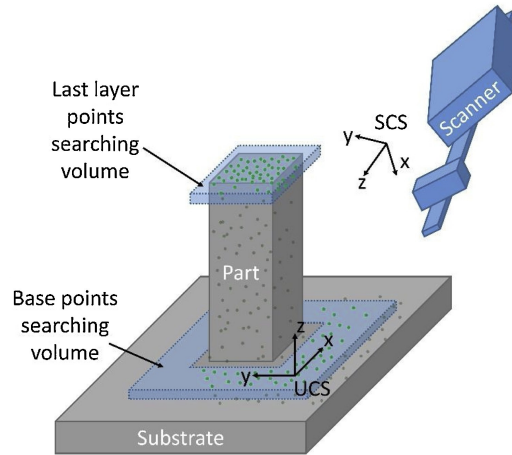


Figure 2.3: 3D scanning arrangement used between successive deposition layers [13].

2.1.4 Coaxial laser triangulation

A recently published innovative variation on normal optical triangulation was developed by Donadello et al. [15] [16], see figure 2.4. In their approach both the laser beam and the camera image used for triangulation project, resp. observe, through the processing head. This approach uses the focussing lens found in the focussing optics of the laser head, to ensure the projected laser beam intersects the focal point (see figure 2.4). This in turn when the substrate is axially displaced, projects a moving image on the coaxial camera. Using subsequent optical processing to remove the thermal signature of the molten metal in the image, this image is then used to calculate the displacement of the 1D point located in the melt pool.

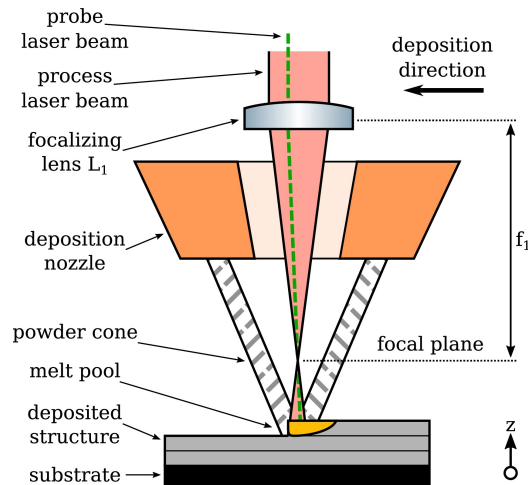


Figure 2.4: Representation of the powder nozzle with a measurement beam probing the melt pool [16].

2.2 Other contact-less sensors

Other than the triangulation-based sensors discussed in the previous section, a variety of other sensors exist which are used to measure the geometry of the workpiece based on a wide variety of methods. Some of these sensors have been implemented in LMD, others have been used for seam-tracking during laser welding and, some have been used to maintain a constant displacement.

2.2.1 Trinocular CCD camera set-up

The first method that will be discussed is the use of a trinocular set-up to monitor the geometry of the laser cladding bead. This method was at its earliest implemented by Mazumder et al. [17] [18], using a arrangement of three photo detectors 120 degrees apart, this method has been referred to as reflective topography. A variation on this method was later developed by Asselin and Toyserkani et al. [19] [20], this method uses the same type of array, but instead using CCD cameras (figure 2.5), to extract clad height, clad width and the rate of solidification.

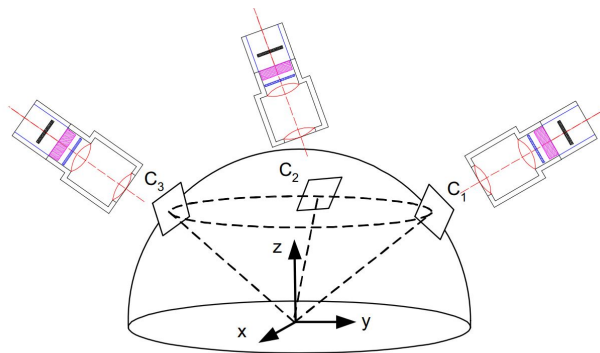


Figure 2.5: Overview of how a trinocular array is positioned [19].

2.2.2 Single CCD camera set-up

A alternative method, implemented by Toyserkani et al. [21], relied on the use of a single CCD camera mounted orthogonally to the laser processing head, to monitor the geometry of the melt pool (see figure 2.6). The geometry was calculated by using image processing to derive the geometry of the melt-pool, from a side-view. This geometry was then fed into a closed-loop controller to control the deposition.

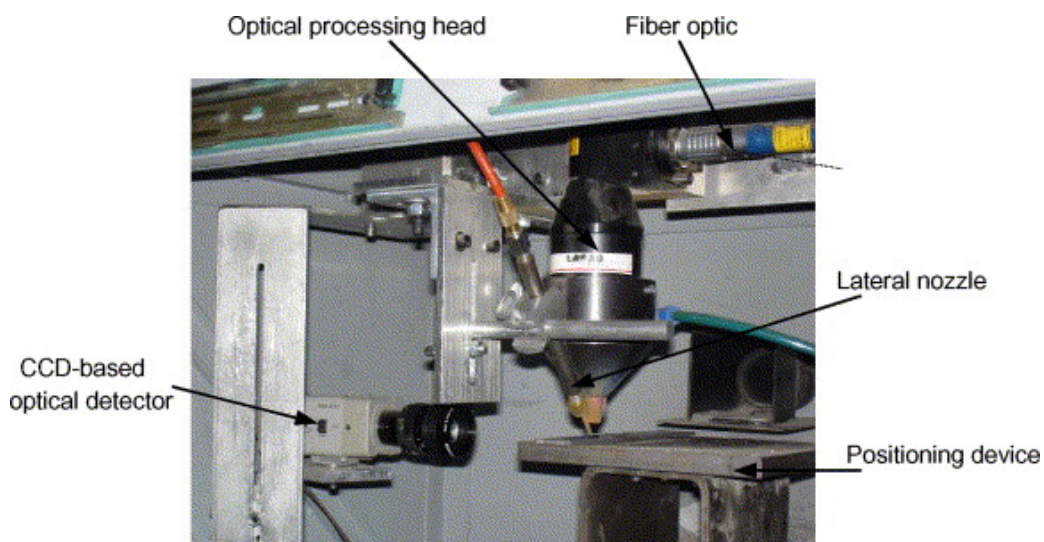


Figure 2.6: Overview of how a camera is mounted orthogonally to the laser processing head [21].

2.2.3 Optical coherence tomography (OCT)

A sensor that has been in use for medical application, has in recent years been applied to laser welding [22]. Furthermore this type of sensor has also been used to control wire-based laser metal deposition with good results [23]. This type of sensor is based on the use of splitting a beam of coherent light into a "probe"-beam and a "reference"-beam, the reference moves through a known length, before interfering with the returning probe-beam. This interference pattern, together with varying the displacement of the reference path, allows for very fast, very precise 3D imaging of the melt pool. An overview of how this sensor is set-up in the case of laser welding can be found in figure 2.7.

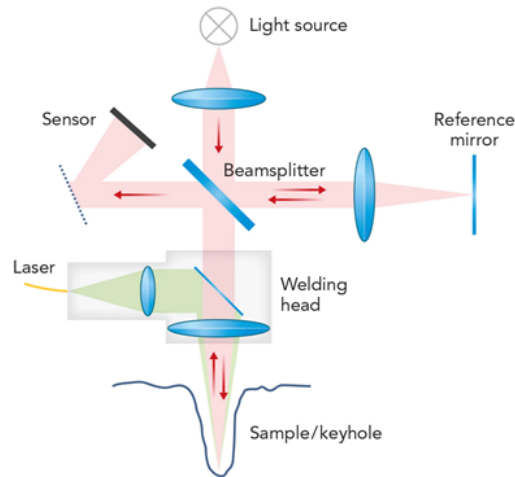


Figure 2.7: Overview of how a OCT sensor functions [24].

2.2.4 Inductive sensor (Eddy current displacement sensor)

A type of contact-less sensor that can be used, is a capacitive sensor. In this kind of sensor, a coil is used to generate an alternating magnetic field. If a workpiece is inserted into this fluctuating magnetic field, the field will induce the creation of Eddy currents in the workpiece. These Eddy currents in turn interact with the original magnetic field causing fluctuations in the amplitude of the current used to generate the magnetic field, as shown in figure 2.8. This change in amplitude can be measured and related to the distance between the probe and the workpiece. This type of sensor can reach sub-nanometre resolution in certain applications. And has been implemented in laser welding applications in for example the work of Bae et al. [25].

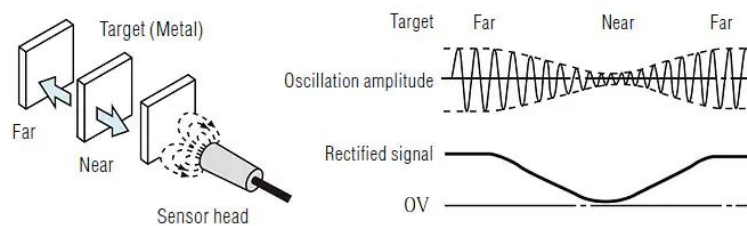


Figure 2.8: Overall overview of the workings of a inductive displacement sensor [26].

2.2.5 Chromatic confocal sensor

A sensor that has been developed and sold by Precitec GmbH [27] and is based on the use of chromatic white light. This method is used in the manufacture of precision components due to its extremely high resolution (sub-micron). As shown in figure 2.9, the sensor emits a chromatic spectrum of light which is focussed by a lens. Due to longitudinal chromatic aberration, the focal length of a single colour, will be dependent on the wavelength of that colour. Thus, when the light hits the target, the most intense wavelength seen by the camera, will vary based on the displacement.

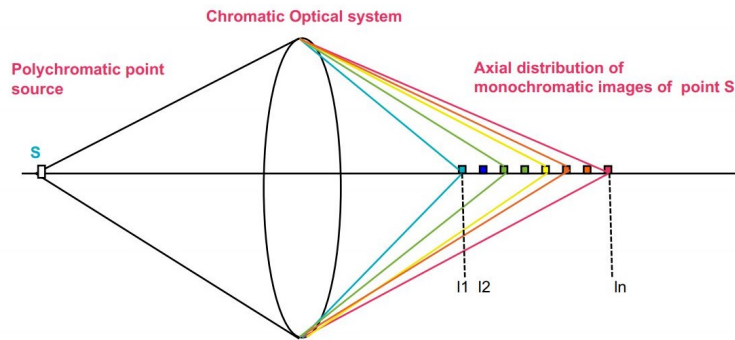


Figure 2.9: Overview of how a sensor using the chromatic confocal principle functions [28].

2.3 Control methods

In the previous section the multiple different methods that have been used to measure the bead height of the deposited material during the LMD process, or are available from different processes, have been shown. However, this discussion will not be complete without a short overview of how these displacement sensors are used, and the effect it has on the final geometry of the deposited clad layers.

One of the observations that can be made based on the literature, is that most of the time, the sensor signal from the displacement sensor is combined with the signal from another type of sensor. For example, in the earlier referenced work of Heralic et al. [6], the geometry calculated using the projected laser line is combined with a value calculated for the size of the melt pool. This in turn is fed into a separate controller for both the height and width of the clad.

Another example of this is the work of Mazumder et al. [29] where the reflective topography geometry measurements are combined with a dual colour pyrometer, this combination resulted in a improved final geometry of a solid part. Another example (and often reported in literature) of Mazumder's work is a height controller using only the cameras, this controller yields the results as shown in figure 2.10.

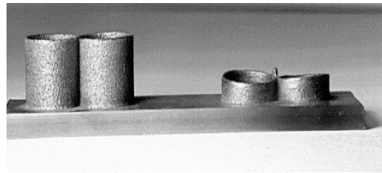


Figure 2.10: Example of LMD fabrication with height controller: (left) with height controller, (right) no height controller [17].

Another alternative that has been shown in section 2.1.3 is, instead of using a real-time controller during the process, the measurements are taken after each layer has been completed, and the processing parameters for the next layer are adjusted based on that data. A example of results using a 3D scanner-based height controller from the work of Garmendia et al., is shown in figure 2.11.

The controllers that have been discussed earlier, use either a measurement before the melt pool, or a 3D scan. However the method referred to in section 2.2.3, OCT, makes it possible to take in-line measurements which yields the results shown in figure 2.12 when used in conjunction with a controller.

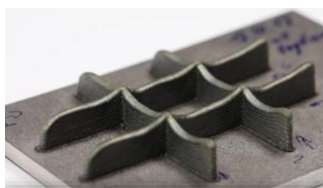


(a) Without height control.

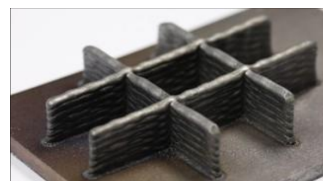


(b) With height control.

Figure 2.11: Results of a 3D scanner-based layer-to-layer height controller [14].



(a) Without height control.



(b) With height control.

Figure 2.12: Results of a OCT sensor based height controller [23].

2.4 Summary and conclusion

In this chapter an overview has been given of the state of the literature on the subject of sensors capable of measuring the geometry of the clad bead below the high power processing laser optic. Also, an overview has been given of the various methods for how a controller was implemented for illustrative purposes, since controllers are out of the scope of this thesis.

An aspect that is clearly shown, is that methods based on triangulation, have been widely applied in this field with the sensors ranging from a projected line sensor, to a 3D scanner using structured light. Lastly a new type of triangulation was discussed based on coaxial laser triangulation.

The second aspect that has been shown, is that for a long time, the main alternative to triangulation based sensors was based on the use of a trinocular camera set-up using various types of optical sensors, or the use of a perpendicularly mounted CCD camera. With only very recently a OCT based scanner being applied for this purpose.

Chapter 3

Concept development and evaluation

In this chapter, the current PF-LMD set-up of the Chair of Laser Processing at the University of Twente, will be presented and discussed. This, together with data from the literature survey will be used to establish requirements that the height sensor, to be developed, should meet. Afterwards, the results from the literature survey will be processed to gather several methods that will be able to meet these requirements. Finally, these methods will be compared with each other, and the overall situation to derive the solution that will best be able to solve the stated problem.

3.1 Situation sketch

As mentioned in the introduction, a PF-LMD set-up consists of multiple components: the laser source, the laser focussing optic (also known as the optical head, or focussing head), and the means for material/gas supply. In the current set-up found in the University of Twente's Macrolab, the laser source is a TRUMPF TRUDISK 10001 Yb:YAG disk laser source. This laser source emits a 1030 nm wavelength laser with a maximum power of 10 kW. This source is connected to the processing optic using a optical transport fibre.

Currently, this set-up is used to perform experiments regarding Laser Metal Deposition, focussing on single direction cladding tracks. In the future, it will be desirable for the set-up to be able to move in multiple directions to create more complex geometries.

3.1.1 Optical beam path

The optic itself is a TRUMPF BEO D70 focussing optic which allows a lens diameter of 70 mm and has lenses available with a focal length of 300 mm, 400 mm, and 600 mm. A overview of the optical layout is shown in figure 3.1. It must be noted that the processing optic that will be used is the 90° version, which has when compared to other designs, the light coming from the target passing through the dichroic mirror.

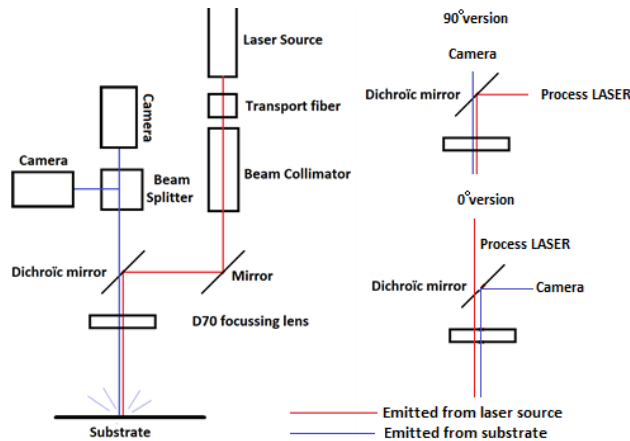


Figure 3.1: Overview of the LMD set-up and a comparison between 90° (top-right) and 0° layouts (bottom-right).

3.2 Laser beam diameter

The processing laser itself is connected to the processing head using an optical fibre. After the laser beam passes through the optical head, two characteristics are known, the BPP (Beam Parameter Product), which denotes beam quality, and w_0 , the beam radius in the focal point. Based on these parameters, the M^2 , which denotes the match between the beam profile and a "perfect" Gaussian beam (like BPP), can be calculated using:

$$\theta = \frac{BPP}{w_0}, \tag{3.1}$$

$$M^2 = \frac{\pi\theta w_0}{\lambda}. \tag{3.2}$$

Then,

$$w = w_0 \sqrt{1 + M^2 \left(\frac{\lambda h}{\pi w_0^2}\right)^2}, \tag{3.3}$$

can be used to calculate the radius for the different lenses available, which is shown in figure 3.2. Table 3.1 gives an overview of these different values, and also lists the Rayleigh range Z_R . Furthermore it lists the distance at which the diameter of the beam is 10 mm (h_{10mm}).

Table 3.1: Optical properties of the laser beam with multiple focal lengths for the D70 focussing lens.

	f = 300 mm	f = 400 mm	f = 600 mm	Units
BPP	25	25	25	mm/mrad
M^2	8.58	8.58	8.58	NA
w_0	0.45	0.6	0.9	mm
Z_R	8.1	14.4	32.4	mm
h_{10mm}	90	120	178	mm

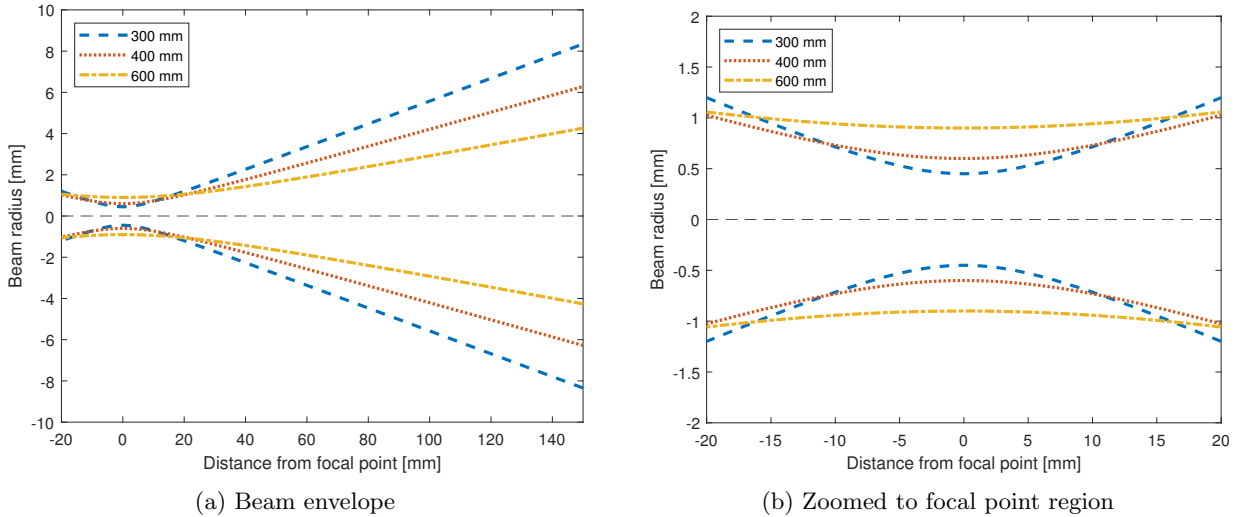


Figure 3.2: Beam radius of the laser beam emitted from the focussing optic. Data has been mirrored over the x-axis to show the complete caustic.

3.3 Formulation of Requirements

To gather sufficient data to make a proper choice for a sensor system, a set of requirements must be specified. As has been mentioned in section 1.2, the goal of the system is to provide online measurements on the height of the clad geometry that is being deposited, for later use in a closed-loop controller. This means that there are three primary quantifiable requirements for the entire system:

1. Accuracy: how accurate the given reading from the sensor should be.
2. Range: the vertical (axial) range of where the sensor can perform measurements.
3. Polling rate: how many times a second the sensor can provide reading.

These three requirements will form the core of the design. The next requirement that will be discussed, is where the measurement is taken. In the literature survey the precise location of measurement varies between methods. That is, before or after the melt pool (e.g. laser line triangulation), to measuring the location inside of the melt pool itself (Optical Coherence Tomography or Coaxial Laser Triangulation). In light of these observations, and from common movements in additive manufacturing, an extra requirement is added that the displacement sensor must be able to cope with the melt pool moving in multiple directions, instead of moving in only a single direction (see figure 3.3).

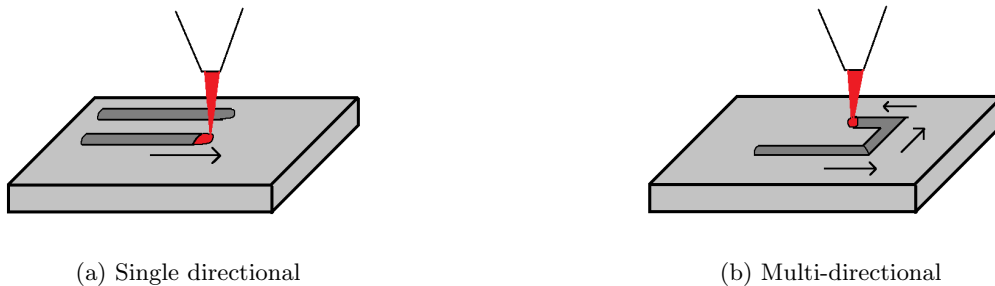


Figure 3.3: Movement capabilities of the optical head.

Furthermore there are two other requirements:

1. The chosen system must be compatible with the current set-up without replacing any major components (e.g. the optical head, processing laser beam etc.).
2. The system must be robust and be able to handle the movement of the robotic arm the system is mounted on without loss of accuracy.

The next step in creating a list of requirements, is to quantify the requirements that have been set.

The first requirement that will be quantified is the required accuracy of the system. Based on the literature survey and discussion, it became clear that the bead heights used varied with the experiments, ranging from 0.3 mm to 1 mm of height. As such, to gain an appropriate amount of insight in the variations during LMD, the desired accuracy of the sensor to be implemented was set at ± 0.1 mm.

The next requirement that will be discussed is the desired range. In section 3.2 the diameter of the laser beam along the optical axis has been discussed, for LMD, the size of the melt pool can be directly related with the beam diameter, and the power of the processing laser beam. Since the current set-up has been used to create clad beads with a width of up to 10 mm, the maximum size of the melt-pool has been set at 10 mm with a focal length of $f = 300$ mm of the processing lens. Thus, due to table 3.1 and some additional range, the desired range has been set at -10 to 100 mm distance from the focal point of the D70 focussing lens.

The last of these requirements that will be discussed, is the desired polling rate of the sensor under consideration. Based on the literature survey, which shows polling rates varying from 100 Hz to 20 Hz, the desired polling rate has been set to 30 Hz to correspond to a simple camera. All of the requirements are summarized in table 3.2.

Table 3.2: List of requirements.

Functional requirements		
Requirement	Value	Units
Axial resolution	± 0.1	mm
Axial range	-10-100	mm
Polling rate	30	Hz
Non-functional requirements		
Compatible with current PF-LMD set-up		
Capable of withstanding robotic arm movements		
Allow for multi-directional movements		

3.4 Proposed Concepts

3.4.1 OCT sensor

The first sensor that has been chosen to be further investigated is a sensor based on Optical Coherence Tomography (OCT). Application of this system to laser processing has been pioneered by the company Precitec GmbH for use in laser metal deposition of components (see section 2.2.3). Most of the systems commercially available are implemented in "scanner type" optical heads (optical heads that via mirrors allow the laser beam to be moved), such as the Trumpf PFO-3D [30] and the Precitec YC30/52 [31], however Lessmüller Lasertechnik GmbH offers the system added onto the Trumpf PFO-3D as a package compatible with the current BEO D70 focussing optic with the 90° layout [32].

The scanner functions by scanning a set of prescribed points and using that data to construct the geometry. This scanner can take these measurements within a radius of 15 mm of the centre and up to 12 mm axially with a scanning frequency of 70 kHz. In the case of the proposed implementation, the choice could be made to scan axially in the centre (i.e. 12 mm displacement with 50 μm resolution, requires a scanning frequency of 30x240 Hz). Another scan that could be proposed, is to scan axially along a line inside the melt pool. Using the proposed settings, it would be possible to axially scan 10 other points within the 15 mm radius. If more points are desired, the axial resolution would need to be decreased.

The scanner used in this sensor, would be mounted onto the system by replacing the top-cover of the optical head with the scanner shown in figure 3.4. The specifications for this system are listed in table 3.3.



Figure 3.4: The Lessmüller OCT scanner under consideration [32].

Table 3.3: Specifications of the Lessmüller OCT tracking system [33].

Specification	Value	Unit
Axial resolution	12	μm
Axial working range	390	mm
Axial measurement range	12	mm
Lateral measurement radius	15	mm
Scanning frequency	70	kHz

3.4.2 Off axis line triangulation sensor

The second method that has been considered, is to mount a laser line triangulation sensor to the current set-up. This kind of sensor has been used in the Macrolab before, for research in laser welding by de Graaf [34], as such a Falldorf S5A laser line sensor is available in the lab. The proposed layout would use one of these line sensors mounted on the side of the current set-up (see Takushima et al. [7]). The data from this sensor would be processed in a computer to derive the height profile along the projected laser line.

Using this height profile, the height of the geometry could be calculated and fed to a controller. The current specifications for such a set-up are listed in table 3.4. One of the main disadvantages of such a system is the fact that the projected line is not coaxial with the high power laser beam, hence it will not be able perform measurements if the movement of the optical head does not intersect the laser line. However in the work of Iakovou [12] a possible solution was found for this problem by using multiple laser lines surrounding the melt pool.

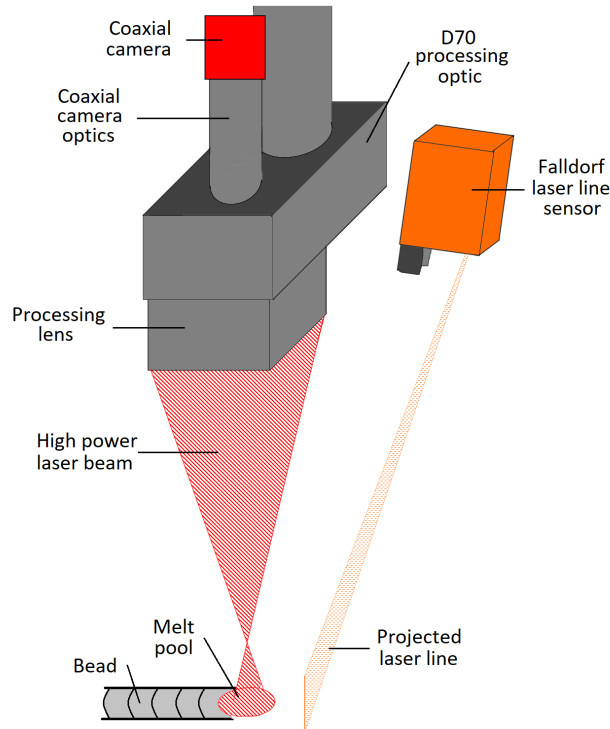


Figure 3.5: The proposed layout of the system using a laser line sensor.

Table 3.4: Specifications of the available falldorf S5A laser line sensor, sourced from [34].

Specification	Value	Units
Axial resolution	22	μm
Standoff distance	56	mm
Axial measurement range	5	mm
Scanning frequency	200	Hz

3.4.3 Coaxial triangulation sensor

Due to the requirements previously established, the third sensing approach is based on Coaxial laser triangulation which was presented in section 2.1.4. In this approach, the existing camera port on the optical head will be re-purposed with the addition of coaxially inserted probe laser beam. This probe laser beam will be inserted into the beam path of the main high power processing laser beam and will be, due to the addition of a small offset from the optical axis, be focussed through the focal point of the D70 focussing lens. Thus, as described earlier, a laser beam will be projected onto the target substrate, and its reflection will move if the target is axially displaced.

This resulting image (of the reflected probe laser beam) is then acquired by the camera mounted on the optical head. This camera is mounted coaxially to the optical axis and was formerly used to monitor the melt pool. To ensure that a clear image of the reflected probe-laser is projected onto the camera, it will be necessary to optically filter it. This can be achieved by using a diaphragm inside the shared focal point, and (primarily) using an optical bandpass-filter that will isolate the wavelength of the probe-laser from the other wavelengths present in the system.

The acquired image is then processed to pinpoint the location of the projected probe-beam on the image itself. This location will then be used to calculate the axial location of the target, using a linear equation. Table 3.5 shows the specifications of the experimental set-up described in the literature survey (see section 2.1.4). Figure 3.6 shows the layout of the proposed system using the system described in the literature as a basis. It must be noted that in contrast with the layout proposed in the literature, due to the 90° layout, an IR-blocking short-pass filter will not be required since the dichroic mirror already blocks these wavelengths from passing through the mirror and entering the coaxial camera-system. This is in contrast with a 0° layout where the dichroic mirror reflects all light except the processing laser wavelength into the optical system.

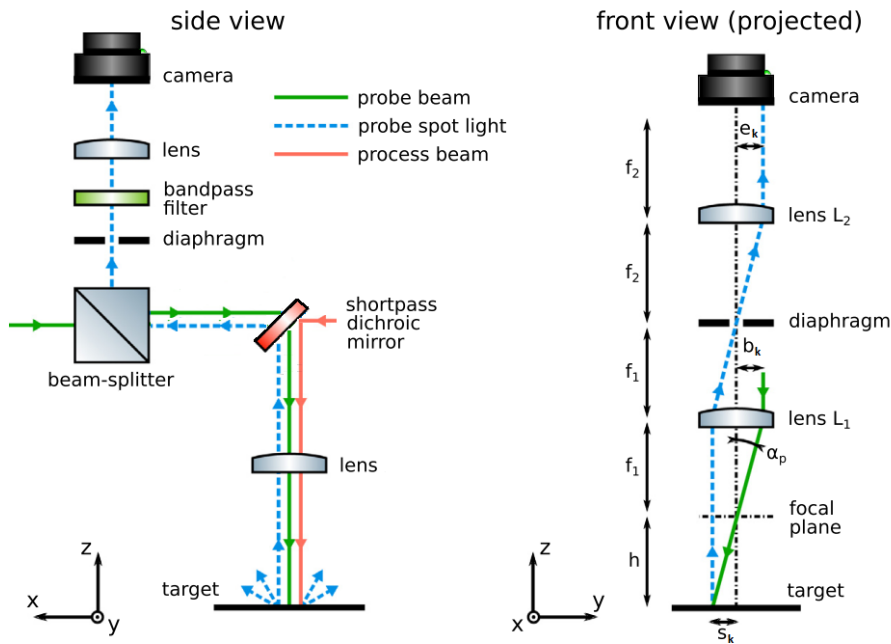


Figure 3.6: The layout of the proposed CLT based system. Adapted from [16].

Table 3.5: Specifications of the proposed CLT based method from the original literature [16].

Specification	Value	Units
Probe wavelength	532	nm
Axial resolution	70	μm
Axial measurement range	-10-15	mm
Scanning frequency	100	Hz

3.5 Concept evaluation

To determine which literature concept will be implemented into the existing setup, it will be required to determine the advantages and disadvantages of each approach. In the requirements (section 3.3), it was stated that it was preferable for a commercially available solution to be used. This of course immediately de-prioritises the CLT based approach, since it is still experimental. The two methods commercially available are the OCT-scanner sold by Lessmüller GmbH. and the Falldorf S5A laser line sensor.

The main problem that currently exists with the use of a laser line sensor, is the fact that the projected line is in front of the melt pool. This means that the direction of movement on the substrate will be limited, so that the melt pool will move over the projected laser line (see figure 3.7). This can be mitigated by rotating the processing optic into the direction of movement; however, this still means that acute corners will not be detected.

To partially solve this issue, it is possible to project multiple laser lines in a triangular configuration to allow for multi-directional tracking of the clad bead. However, at this point, this has only been implemented for seam tracking [12]. Another problem with the Falldorf S5A sensor specifically is that the included image processing software does not have an API for on-line accessing the height profile, only for the resulting processed seam-tracking parameters.

The third problem with a laser line configuration lies in the fact that the controller must precisely "know" when and where the measurement is performed. For moving in a straight line, this is no problem. However, when the direction of movement changes, this data must also be fed into the controller, to compensate for the change in time between measurement and cladding.

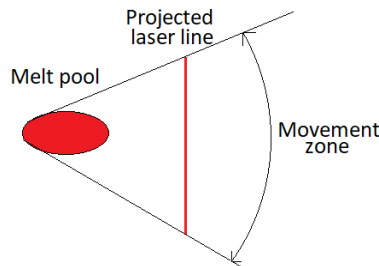


Figure 3.7: Movement limitation of single laser line.

The other method commercially available for implementation on the existing optical head, is the OCT scanner (see section 3.4.1). When analysing the specifications and the capabilities of this type of scanner, it becomes clear that it is the best option for integrating on-line displacement measurements of the target, together with the additional capabilities (line scanner, melt pool geometry scanning) that the scanner is capable of. The main problem that the proposed implementation currently has is that the axial measurement range is limited to 12 mm. Which means that during LMD, the scanner must be set to read the required offset from the focal point. However, it is expected that this does not present a problem, since if the deviation from the set distance from the focal point, exceeds the working range, the work piece will have deviated severely from the planned geometry anyway.

The main disadvantage of this sensor is the cost, initial contacts made with Lessmüller, estimate the approximate cost of the system and supporting software to be about €50.000.

Due to two commercially available options either not meeting the specifications to be implemented (laser line sensor), or being too expensive, the final choice fell to implement the experimental CLT method. According to the original implementation, it will be possible to implement it in such a way, that all requirements stated in table 3.2 all except the commercial availability can be reached. However, it will require developmental work, to ensure that the specified measurement range can be reached. The main area of further development will be to ensure that the increased axial range (which is linked to melt pool size), and thus thermal emissions from the melt pool, does lead to an acceptable signal on the image sensor.

Chapter 4

Design and modelling of a CLT sensor

In this chapter a start will be made with designing the implementation of a CLT-based sensor as was chosen to implement. To do this, several models and calculations were created to help fully define and quantify the different parameters, required for the final implementation.

4.1 Design variables

Based on theoretical modelling and the original concept, the design variables that are needed for a full design are:

- Probe beam offset b_k : This is the distance (perpendicular to the optical axis) between the probe beam and the optical axis of the high power laser beam in the processing head. This variable can be altered by displacing the laser beam at the ingress port of the processing head, this primarily impacts the resolution of the measurement.
- Optical magnification M : This is the amount of magnification between the image on the target (substrate) and the image on the sensor, this parameter also primarily impacts the axial resolution of the sensor.
- Properties of the probe laser (P_{probe} and λ_{probe}): these are the primary properties of the probe laser, P_{probe} is the power emitted by the probe laser source and λ_{probe} is the probe laser wavelength, these properties will impact the signal-to-noise ratio of the sensor.
- Bandpass-filter properties: The optical signal passes through an optical filter eliminating all wavelengths except λ_{probe} in the sensor, depending on the wavelength, different widths of filter are available, this will impact the signal-to-noise ratio of the signal.

The size of the diaphragm used will also have an effect on the signal-to-noise ratio in the system by suppressing unwanted reflections caused by the optics, but while an attempt will be made to investigate some of the effects using a ray tracing analysis, the primary analysis will be investigated experimentally using an adjustable diaphragm.

4.1.1 Available components

To implement the sensor system into the Trumpf D70 laser processing head, several different components are needed. Luckily, the coaxial process monitoring camera already mounted on the processing head, is available for use. This yields the following components:

- Baumer TXG03 0.3 mega-pixel monochrome GigE machine vision camera (see table 4.1, mounted with a 100 mm focal length lens).
- Trumpf GmbH 2-way camera port used to allow addition of extra optical sensors for process monitoring. This camera port is a beam splitter.
- Multiple lenses of the processing head are available for use (focal length: 300 mm, 400 mm, and 600 mm).

An important note is that the diameter of the coaxial camera optics is 20 mm, thus the maximum offset b_k will be limited to 8 mm due to the diameter of the laser beam itself.

Table 4.1: Some properties of Baumer TXG03 monochrome camera [35].

Property	Value	Unit
Max resolution	656x494	pixels
Pixel size	7.4x7.4	μm
Max fps	90	fps
Exposure time	0.004-60000	ms
Data interface	GiGE ethernet	

4.2 Design and modelling of optics

In this section, a simple model will be used to calculate the resolution of the optical system. Furthermore, the design will be adapted to ensure the requirements will be met.

4.2.1 Original layout

To design the sensor optics so that it can meet the stated requirements (see section 3.3), the first step will be to create an optical model of the optic. A simple geometric model can be used that uses the path of a single ray emitted by the probe laser on the target. A simplified sketch, based on the original proposed system [16] is shown in figure 4.1.

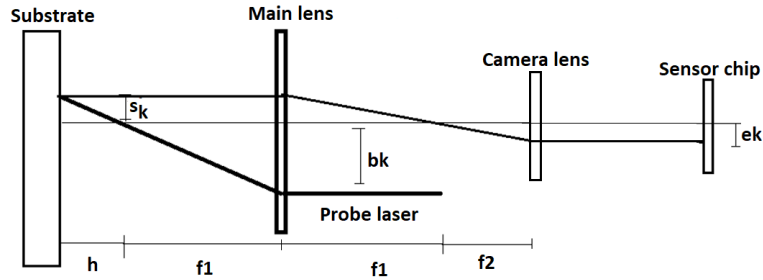


Figure 4.1: A schematic of the path of a single ray in the proposed CLT system.

In this sketch it can be observed that the projected single beam forms a set of equivalent triangles, that links the system together. Using these triangles, the equation linking the probe laser offset (b_k), to the distance on the target (s_k), reads,

$$\frac{s_k}{b_k} = \frac{h}{f_1} \Rightarrow s_k = \frac{b_k}{f_1} h. \quad (4.1)$$

Redoing this equation using the other set of equivalent triangles,

$$\frac{e_k}{s_k} = \frac{f_2}{f_1} \Rightarrow e_k = \frac{f_2}{f_1} s_k, \quad (4.2)$$

allows us to calculate the location of the probe laser on the target as a function of the height by substituting,

$$e_k = \frac{f_2 b_k}{f_1^2} h. \quad (4.3)$$

However, because this section is about calculating the overall resolution of the sensor, equation (4.3) will need to be rearranged to investigate the sensitivity caused by moving one pixel on the sensor (dS), on the calculated axial displacement (dh). This results in:

$$dh = \frac{dS f_1^2}{b_k f_2}. \quad (4.4)$$

In this equation, it can be seen that either increasing the probe laser offset b_k or camera lens focal length f_2 , or decreasing processing lens focal length f_1 will result in an decreased sensitivity to a movement on the sensor.

Plotting equation (4.4) as function of variable b_k with, f_2 : the available camera lens, dS : the pixel size, and, the available processing lenses f_1 yields figure 4.2. When analysing this figure, it becomes clear, that to reach the desired system accuracy at maximum achievable offset (8 mm), the position of the probe laser on the camera must be very precisely interpolated (e.g. for $f_1 = 300$ mm, the location must be known to within 0.25 pixels, see table 4.2 for each processing lens).

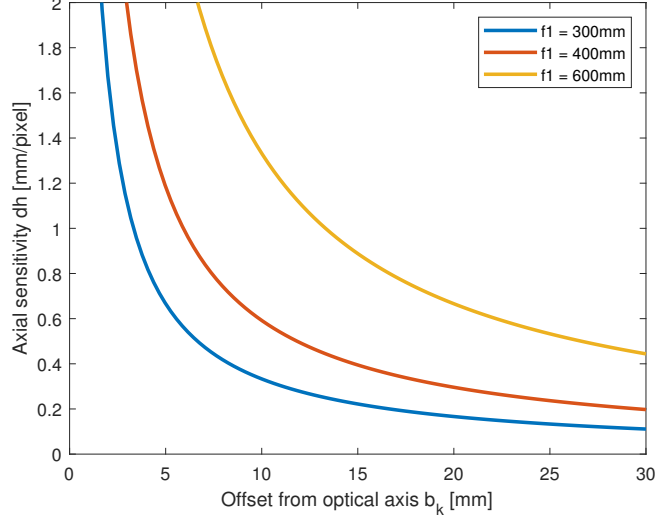


Figure 4.2: Axial sensitivity dh as function of b_k for different focal lengths.

Table 4.2: Some general numbers regarding requirements extracted from equations (4.1) to (4.6).

Lens [mm]	Sensitivity @ $b_k = 8mm$ [mm/pixel]	Interpolation accuracy to reach \pm 0.1 mm [pixels]	Maximum range [mm]
300	0.4	± 0.25	272
400	0.75	± 0.13	485
600	1.62	± 0.06	1091

Because of the interpolation accuracy required to reach the target accuracy being so high due to the limited offset, it is necessary to investigate changing the current parameters. If the maximum displacement that the camera sees can be increased, the resolution of the system will increase as well. Rewriting equation (4.3) to show the magnification factor between the target and the image of the camera yields:

$$e_k = M_{Cam} \frac{b_k}{f_1} h. \quad (4.5)$$

In the current configuration using the TXG03 camera, the magnification factor M_{Cam} between the projected spot on the melt pool, and the image on the camera, is f_2/f_1 and ranges, depending on the chosen processing lens, from a factor 1/3 (with $f_1 = 300$ mm) to a factor 1/6 (with $f_1 = 600$ mm), which is much lower than the magnification reached in the paper by Donadello et al. [15] (factor 2/3) which together with the $5 \times 5 \mu m$ pixel size explains the superior resolution obtained in the paper.

4.2.2 Adapted layout

As such, as it is desirable to keep the camera, it will be necessary to increase this magnification factor significantly so that the required interpolation accuracy to meet the requirement is decreased. As such if the requirement is set that the interpolation accuracy is 0.5 pixels, the magnification factor must be multiplied with a factor 2 to 4 (see table 4.2 and divide the set interpolation accuracy by the interpolation accuracy to reach ± 0.1 mm). The simplest way to do this, is to for example increase the focal length of the camera lens by a factor 3. This would mean that the current 100 mm lens must be replaced with a 300 mm focal length lens, which will result in geometry shown in figure 4.3.

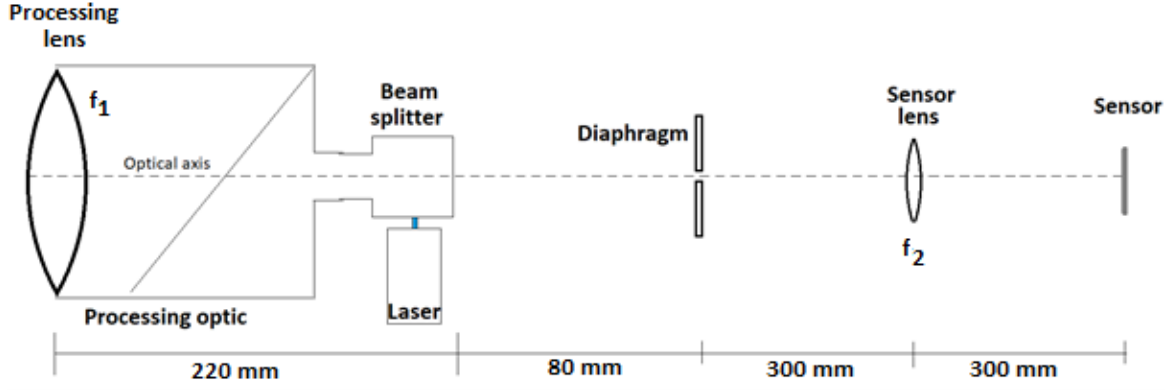


Figure 4.3: Geometry of the originally proposed CLT system.

It can be derived from this figure, that this layout will result in a (too) long (680 mm) optical system and since the diaphragm is preferably located in the common focal point longer processing lenses, will increase the length further (see table 4.3).

Table 4.3: Length in mm of added optical system for multiple magnification factor.

f_1	Additional magnification			
	1	2	3	4
300	280	480	680	880
400	380	580	780	980
600	580	780	980	1180

It can easily be seen that such a lengthy optical system is not practical for use in a LMD set-up due to the weight and length of this system (an example of problems could be vibrations of the camera system). For this reason, it is desirable to change the optical layout of the system to increase the magnification in a different way.

4.2.3 Addition of telescope

One of the possible ways, and one that was used in an earlier master-assignment within the group [36], was to add an optical telescope between the lenses in the system, to magnify the resulting image. According to W.J. Smith's Modern Optical Engineering [37], there are three basic types available:

- Keplerian (astronomical) telescope using two converging lenses.
- Galilean (Dutch) telescope using a diverging and a converging lens.
- Lens erecting telescope using an additional lens to "erect" the image.

Another advantage of adding additional lenses to the system, is that by manipulating the location of one of these lenses, the focal length of the entire optical system can be adjusted. This is important, because when working at the end of the stated range, the image will be out-of-focus and thus very large. By slightly adjusting the focal length of the imaging system, the size of the out-of-focus image on the camera sensor is limited. The diaphragm can then be located behind the additional lenses such that the combined focal point of the optical system is positioned properly.

Of course, adding an additional telescope to the optical system will require the previously determined relations to be adapted. However this can easily be done by assuming that the distance s_k seen by the optical system is additionally magnified with a factor M_{add} , and redefining M_{Cam} to $(M_{Cam} = M_{add} \cdot f_2/f_1)$ in equation (4.5). Based on this plots for increasing magnification M_{add} are shown in figure 4.4a.

However increasing the magnification, logically leads to a reduction in the maximum possible measurement range (h_{max}) because the maximum displacement on the camera chip (S) is limited (figure 4.4b,

$$h_{max} = \frac{Sf_1^2}{b_k f_2 M_{Cam}}. \quad (4.6)$$

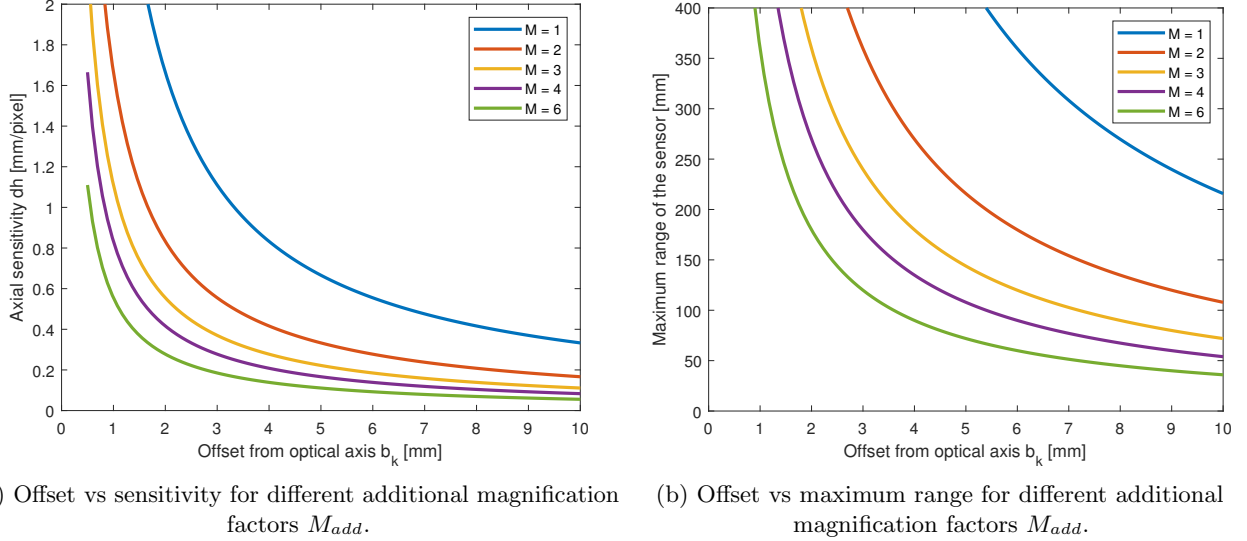


Figure 4.4: Plots showcasing the relation between the coaxial offset, the axial sensitivity, and maximum range.

As a result of these calculations, a compromise is necessary to choose the additional magnification that the telescope will need to be designed for. Another point to consider is that the projection on the camera sensor will also have a diameter dependent on the size of the diaphragm.

4.3 Design and modelling of probe laser beam and filter

In this section, a model will be derived to determine what the required properties of the probe-laser and bandpass-filter are to gain a sufficiently high Signal-to-Noise-Ratio (SNR), this will then be used to select an appropriate laser and bandpass-filter.

4.3.1 Signal-to-Noise modelling

The first part in creating the model, is to determine what needs to be investigated. The first aspect that is investigated, is to determine what kind of noise is expected to be present in the system. Several sources have been identified, namely:

1. Thermal emissions from the (white hot) molten metal.
2. Internal reflections from the optical system (e.g. reflections from the probe laser beam on optical components, dust, fingerprints etc.).
3. Unwanted reflections caused by the probe laser hitting the stream of particles used in LMD.

In this theoretical model, primary consideration will be given to the source of noise represented by the thermal emissions from the melt pool. This because thermal emissions are theoretically well understood while the internal reflections, are by their nature highly dependent on the implementation and thus hard to model (the effect in the implementation will herefore be discussed in section 5.3.4).

The primary focus of this model is to calculate the amount of thermal emissions emitted from the melt pool and to derive a function representing the spectral transmittance (T_λ) of the optical system. The spectral transmittance of an optical system, is defined as the fraction of light at a certain wavelength, that is transmitted through the system.

A global overview of the optical path, is shown in figure 4.5. Some of the main assumptions made, are that the lenses in the system have a constant transmission ratio above 90% and can be directly multiplied for the overall calculations.

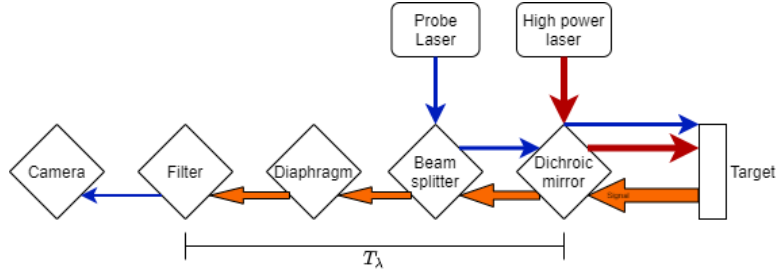


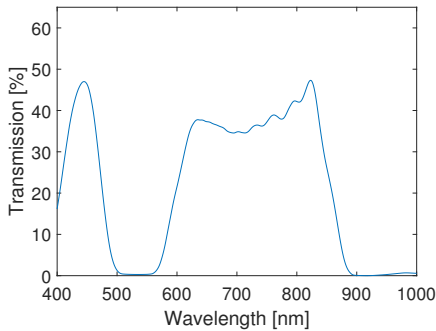
Figure 4.5: A flowchart showing the path of the probe laser and thermal emissions through the system.

Transmittance of optical components

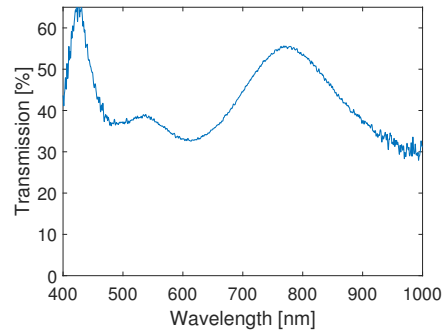
Figure 4.5 shows that there are four main optical components that have an effect on light incident on the camera, of these, three have a effect on the spectral transmittance of the system, while the fourth component (the diaphragm) will be discussed separately in section 4.4.4. So the three components that are relevant for the spectral transmittance are:

- The dichroic mirror, reflecting the high power processing laser through the lens, while allowing the probe laser beam to pass through.
- The beam splitter, responsible for splitting incident light into two equal components with different directions.
- The optical filter, responsible for eliminating all non-probe laser wavelengths from the system to increase the strength of the signal-to-noise ratio.

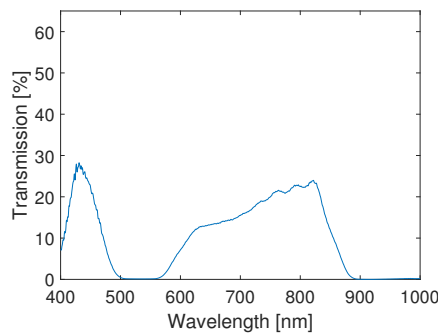
The first two components are original components of the processing head, where the specifications where not readily available. Thus it was necessary to measure the transmittance of these components. This was done with the use of a source of white light, combined with a spectrometer (for more information on methodology, see appendix A). The results from these measurements can be seen in figures 4.6a, 4.6b and combined in figure 4.6c. It can be concluded from the figures that the system transmits light between 400-500 nm and between 650-800 nm.



(a) Transmission spectrum of the TRUMPF D70 optical head.



(b) Transmission spectrum of the measured path of the TRUMPF camera port.



(c) Transmission spectrum of the combined OEM system.

Figure 4.6: Transmission spectra of the laser processing head.

The final component that affects the overall spectral transmittance of the camera system, is the bandpass-filter responsible for isolating the signal from the probe laser from all other wavelengths in the system. An example of the transmission spectrum of such a filter is shown in figure 4.7 and is defined by the following specifications:

1. Centre wavelength (CWL), location of the transmittance peak.
2. Transmittance ($T(\min)$), the minimum amount of transmittance at the designed centre wavelength.
3. Full Width at Half Maximum (FWHM), the wavelength range specified by half the maximum transmittance.

There are a wide variety of bandpass-filters available with varying CWL and related $T(\min)$ and FWHM. For most wavelengths, a FWHM of 10 nm is available, with 1 nm FWHM only available for special wavelengths (488, 532 or 632.8 nm). As such for this model it has been assumed that the bandpass-filter is the same shape ($T(\min)$ and FWHM) as in figure 4.7, with only the CWL varying.

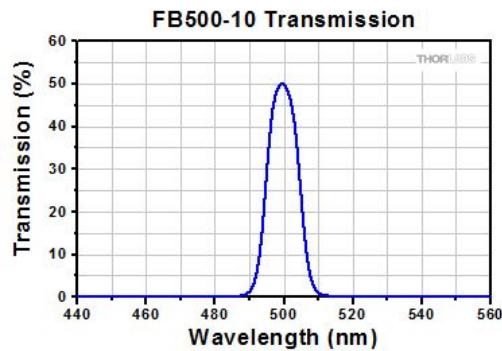


Figure 4.7: Transmission plot of a THORLABS FB-500-10, 500nm CWL, 10nm FWHM $T(\min) = 50$ bandpass-filter [38].

Melt pool emissions modelling

As mentioned in previous sections, the melt pool during the LMD process emits a broad spectrum of wavelengths consisting of thermal emission from the molten metal, combined with the incident light of the probe laser beam. The amount of thermal energy emitted can be calculated using the Stefan-Boltzmann law for a grey body (blackbody with $\epsilon < 1$), which reads,

$$P = A\epsilon\sigma T^4, \quad (4.7)$$

where P = power emitted, A = black-body area, σ = Stefan-Boltzmann constant and, T = surface temperature of the black body. However this total amount transmitted, is over the entire spectrum of wavelengths, and as was seen in section 4.3.1, the coaxial camera is only sensitive in the visible part of the spectrum (400-720 nm). Furthermore, because the transmittance of the optical head depends on the wavelength, the amount of energy per wavelength will need to be calculated. To calculate this, Planck's law needs to be used,

$$B(\lambda, T) = \frac{2hc^2}{\lambda^5} \frac{1}{e^{\frac{hc}{\lambda k_B T}} - 1} \epsilon \quad [W \cdot sr^{-1} \cdot m^{-3}], \quad (4.8)$$

in which h = Planck's constant, c = speed of light in a vacuum, λ = the wavelength, k_b = Boltzmann constant and T = surface temperature, which yields the spectral radiance. To use this equation to calculate the amount of power per wavelength (thus thermal noise) entering the camera, the first thing that must be done is to multiply with the surface area of the melt pool, resulting in the unit known as spectral intensity ($[W \cdot sr^{-1} \cdot m^{-1}]$).

The next step is to determine how much light is incident on the optical system, for this, the solid angle must be determined. The solid angle can easily be calculated by assuming that light travels from the target to the optic in the shape of a cone aligned with the optical axis (figure 4.8). The solid angle, sr , of this cone can then be calculated using,

$$sr = 2\pi(1 - \cos(\theta)) \quad \text{with} \quad \theta = \text{atan}\left(\frac{D_{\text{optic}}}{2(h + f_1)}\right). \quad (4.9)$$

As can be seen this equation is directly dependent on the distance of the target. Thus when the target is axially displaced, the power received by the optical system decreases, due to the smaller size of the cone, but the power emitted by the melt pool increases (due to the increase in area by the larger laser beam).

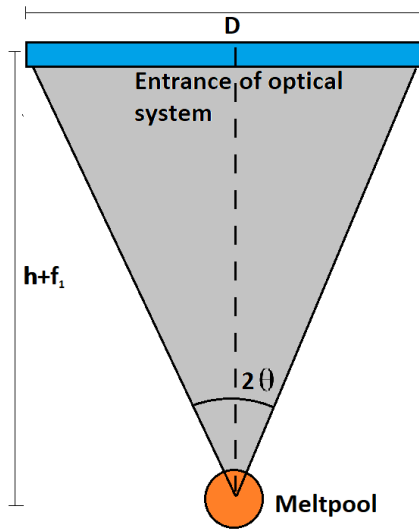


Figure 4.8: section sketch of the emitted cone of light entering the optical system.

If Planck's equation (4.8) is multiplied with the resulting solid angle, and the area of the melt pool (thus results are in $[W \cdot m^{-1}]$), it yields the power per wavelength (called the spectral flux) entering the optical system. Figure 4.9 shows the amount of power entering the optical system.

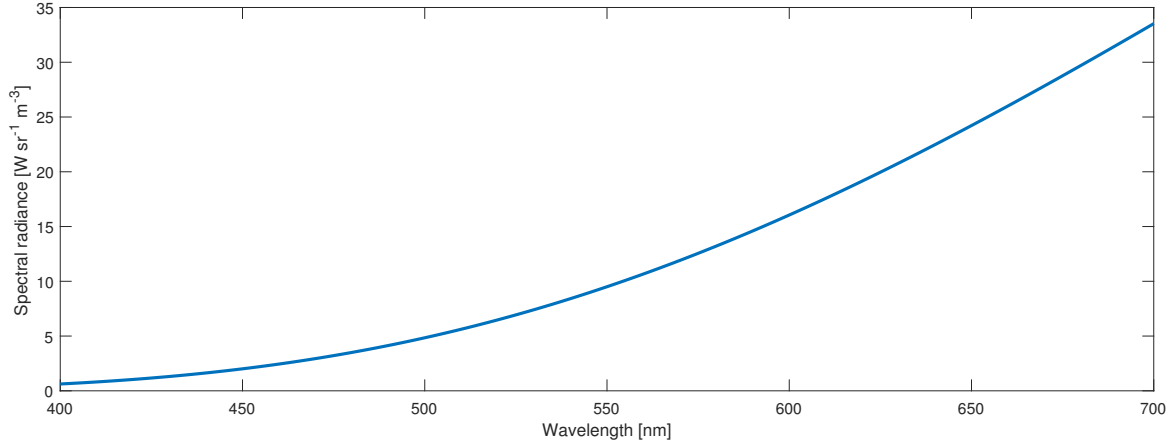


Figure 4.9: Spectral radiance of a 2273K surface in the visible spectrum (400-700nm).

Up until now, Planck's equation (4.8) was used using a solid surface with a constant temperature T_{max} . However in research it has been shown that the temperature profile during LMD is almost linear along the radius of the melt pool [39]. To model this linear behaviour using equation (4.8), it will be needed to divide the melt pool into discrete parts, each with a temperature calculated using a linear temperature profile,

$$T(x, y) = T_{max} - \frac{\sqrt{x^2 + y^2}}{D} T_{min}. \quad (4.10)$$

Figure 4.10 shows the resulting melt pool, this result can be scaled up to calculate for a larger diameter melt pool.

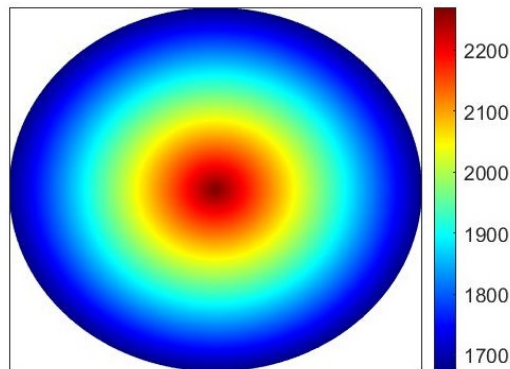


Figure 4.10: Calculated temperature profile of melt pool divided into discrete square pixels, with linear temperature profile from 1773 to 2273 K.

Signal-to-noise ratio model

Using the transmittance from the optical components and combining it with the spectral data from the melt pool, a simple model can be created that will allow the signal-to-noise ratio (SNR) of the signal incident on the camera,

$$SNR = \frac{P_{probe@cam}}{P_{thermal@cam}}, \quad (4.11)$$

where $P_{probe@cam}$ = amount of remaining power of the probe laser beam and $P_{thermal@cam}$ = amount of remaining thermal power to be calculated.

The first step is to derive the equation linking the power spectrum emitted by the probe laser to the spectrum it has when it is projected onto the melt pool (see table 4.4),

$$P_{probe@melt}(\lambda) = P_{probe@start}(\lambda) \cdot T_{splitter}(\lambda) \cdot T_{mirror}(\lambda) \cdot T_{lens}. \quad (4.12)$$

Using this spectrum, the SNR at the melt pool can be calculated, however because the wavelength of the probe laser beam has not been isolated using a filter, the SNR will be very low unless an unreasonably powerful (> 10 to 15 watts) probe laser source is used. Thus a second set of equations is created that will link the emissions from the melt pool (reflected probe light and thermal emissions) to their strength when they hit the camera,

$$P_{probe@cam}(\lambda) = \frac{P_{probe@melt}(\lambda)}{2\pi} sr(h) \cdot T_{mirror}(\lambda) \cdot T_{splitter}(\lambda) \cdot T_{filter}(\lambda) \cdot T_{lens}^2, \quad (4.13)$$

and

$$P_{thermal@cam}(\lambda) = P_{thermal@melt}(\lambda) \cdot T_{mirror}(\lambda) \cdot T_{splitter}(\lambda) \cdot T_{filter}(\lambda) \cdot T_{lens}^2, \quad (4.14)$$

(see table 4.4). It must be noted that it has been assumed that the probe light is scattered equally in a hemisphere ($2\pi sr$) thus to calculate the amount of light reflected into the optics, the power has been normalized. Furthermore, two lenses have been assumed to be present in the optics (process lens and camera lens).

Table 4.4: Overview of all variables relevant in section 4.3.1.

Symbol	Description	Value
$P_{probe@start}(\lambda)$	Probe power emitted by laser	
$P_{probe@melt}(\lambda)$	Probe power hitting melt pool	
$P_{probe@cam}(\lambda)$	Probe power hitting camera	
$P_{thermal@melt}(\lambda)$	Thermal power emitted by melt pool into optic	See figure 4.9
$P_{thermal@cam}(\lambda)$	Thermal power emitted by melt pool hitting camera	
$T_{mirror}(\lambda)$	TR-spectrum of dichroic mirror	See figure 4.6a
$T_{splitter}(\lambda)$	TR-spectrum of beam-splitter	See figure 4.6b
$T_{filter}(\lambda)$	TR-spectrum of bandpass-filter	See figure 4.7
T_{lens}	TR-ratio of 1 lens	0.9
$sr(h)$	Solid angle between melt pool and optics	Section 4.3.1

4.3.2 Selection of the probe laser source and the filter

With the SNR model available, it will be possible to determine the influence of the thermal emissions of the melt pool in order to choose the remaining design parameters P_{probe} and λ_{probe} and the corresponding optical bandpass-filter.

Probe laser wavelength

Analysing the system, it becomes clear that, if the power of the probe laser is set to a constant value, the signal-to-noise ratio of the system will largely be dependent on wavelength of the bandpass-filter. This is because if the shape of the transmission ratio curve of the filter w.r.t the probe laser wavelength is constant, independent of the chosen CWL (a reasonable assumption within the visible spectrum), the amount of thermal radiation that enters the camera will be dependent on the CWL of the filter since the other optical components (mirror and splitter) are fixed. This is illustrated in figure 4.11 where the amount of power remaining after passing through the optical system with varying CWL for the bandpass-filter is shown.

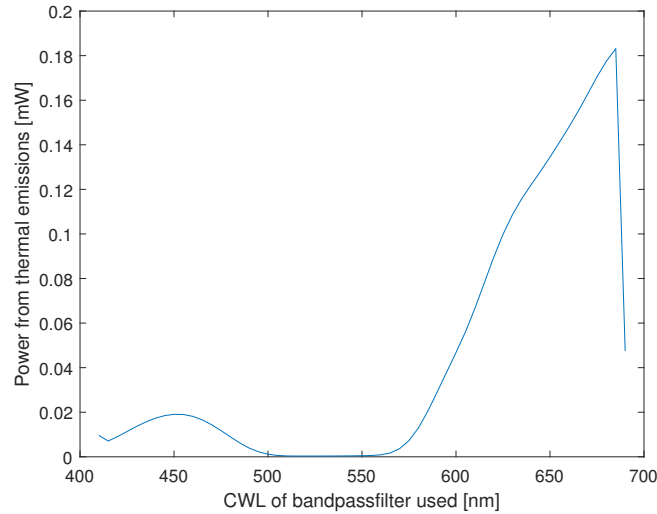


Figure 4.11: The amount of thermal emissions after passing through the optical system if the CWL of the bandpass-filter is varied along the visible part of the spectrum. Model is in the focal point of the $f = 300$ mm lens.

Firstly, it can be observed from figure 4.11 that between circa 500 to 550 nm, all thermal emissions are suppressed. This is because this part of the spectrum has been completely suppressed by the dichroic mirror (figure 4.6a) since it can contain the parasitic wavelengths caused by the source of the processing laser beam. But overall the conclusion that can be drawn from figure 4.11 is: that a lower chosen wavelength (excepting the region from 500 to 550 nm) for the filter (and thus the probe laser source) will result in less thermal emissions incident on the camera thus overall the signal-to-noise ratio at a given amount of laser power, would increase.

Power of the probe laser source

The other part of the equation, is as earlier mentioned, the amount of power that the probe laser needs to emit into the system, which was modelled in section 4.3.1. The main design goal for this laser power, is that the signal-to-noise ratio at maximum range (thus maximum thermal emissions) must be sufficiently large. To calculate this SNR, the easiest way will be to multiply the thermal emissions on the sensor from figure 4.11 with the desired SNR. The resulting number is then equal to the amount of power of the probe laser source that hits the sensor. Using this value, it is then possible to calculate the starting amount of power by using figure 4.12, which shows the relation between starting power and the remaining power using the model that was created.

Figures 4.11 and 4.12, show that at lower wavelengths, there are lower thermal emissions hitting the camera, and the probe laser beam is transmitted more efficiently through the system. To ensure that the probe laser beam was being transmitted at the most efficient wavelength, a laser source with a wavelength of 450 nm was highly preferred. At this wavelength, the required power for a sufficient SNR at $h = 100$ mm is about 500 mW. Furthermore, due to the way the system works, decreasing the axial displacement (and thus the size of the melt pool), will results in much better SNR performance as can be seen in figure 4.13.

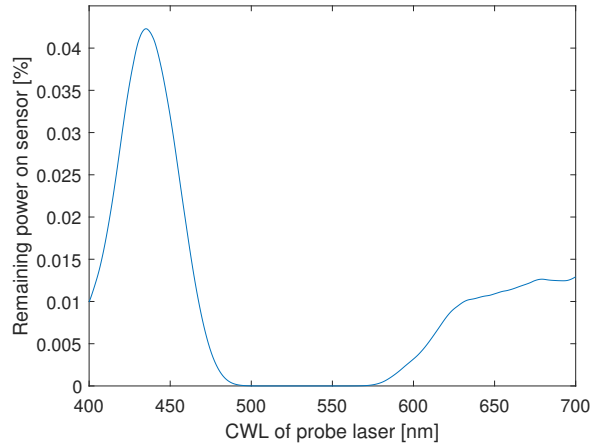


Figure 4.12: The fraction of power from the probe laser, that hits the camera sensor at $h = 100mm$.

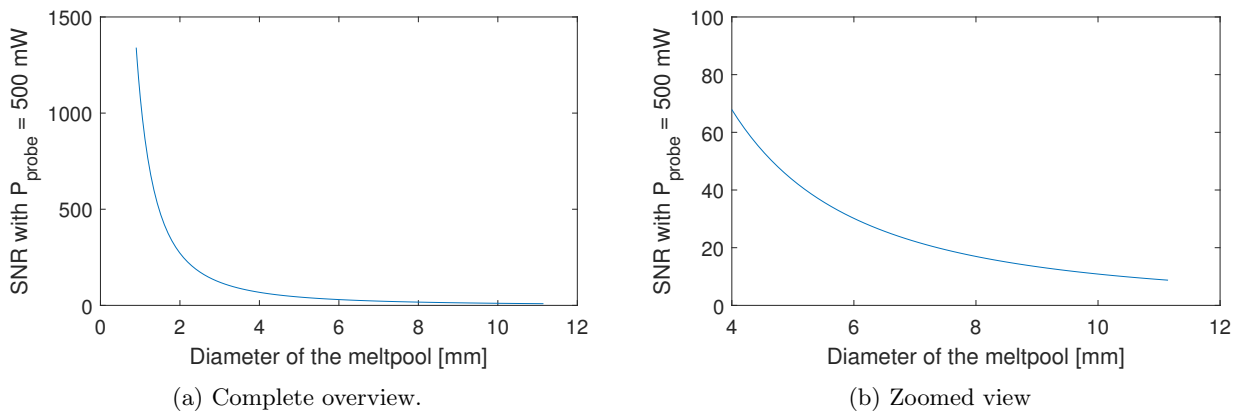


Figure 4.13: The signal to noise ratio of the 450 nm 500 mW laser with increasing diameter of the melt pool.

Selecting the probe laser source

When investigating the commercially available laser sources that meet the requirements (450 nm, 500 mW), it became clear after contacting several manufacturers, that complete laser modules are not available from a reputable supplier. The main alternative is to buy all the required components to build a diode laser source, which has been found to be the main available type of laser source in this power category. However this would mean that the following components had to be bought and assembled: diode laser power supply, diode laser, diode can mount, diode can cooling system and a collimator array.

In the end the decision was made to investigate the use of a much cheaper diode laser module supplied by ODICFORCE [40]. This 450 nm 2W laser module (figure 4.14) comes in a single package and was meant for use in CNC laser engraving applications. However this laser source has been modified with the addition of a collimator lens to be used as the probe laser. The experimentally determined properties of the laser will be discussed in the next chapter.



Figure 4.14: The diode laser module that will be used as a probe laser source [40].

4.4 Advanced ray-tracing model

Previously, the optical behaviour of the system was approximated using a geometric model, however this model does not consider the behaviour of the image out-of-focus $h > 0$ nor the presence of a diaphragm. Especially the influence of a diaphragm requires further investigation.

4.4.1 Ray transfer matrix analysis model

To model the optical system, a method known as ray transfer matrix analysis (or ABCD matrix analysis),

$$\begin{bmatrix} y_2 \\ \theta_2 \end{bmatrix} = \begin{bmatrix} A & B \\ C & D \end{bmatrix} \begin{bmatrix} y_1 \\ \theta_1 \end{bmatrix}, \quad (4.15)$$

has been used, in which $[y_1 \ \theta_1]$ are parameters of the input ray, $[y_2 \ \theta_2]$ are parameters of the output ray, and $[A \ B; C \ D]$ are parameters of the ray transfer matrix (see figure 4.15). This method is a form of ray tracing using the paraxial (small angles) approximation. The method models each optical element (such as a lens, mirror, or propagation through a medium) as a 2x2 matrix-vector equation,

$$M_{thinlens} = \begin{bmatrix} 1 & 0 \\ -\frac{1}{f} & 1 \end{bmatrix}, \quad M_{propagation} = \begin{bmatrix} 1 & d \\ 0 & 1 \end{bmatrix}, \quad (4.16)$$

where f is the focal length of the lens, d is the propagation distance along the optical axis (i.e. distance between two optical components), $M_{thinlens}$ is the ray transfer matrix of lens using the thin lens approximation, and $M_{propagation}$ is the ray transfer matrix of propagation through air.

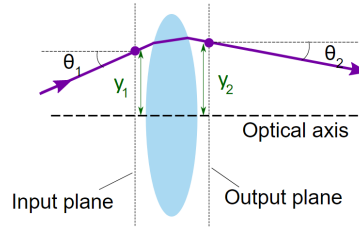


Figure 4.15: Representation of transformation between input plane and output plane of a single lens [41].

In the case of the system that is under consideration, the construction of the ABCD matrix is done by multiplying the ray transfer matrices of the different components and equals,

$$\begin{bmatrix} A & B \\ C & D \end{bmatrix} = M_{propagation \ target \ to \ f_1} \cdot M_{f_1} \cdot M_{propagation \ f_1 \ to \ f_2} \cdot M_{f_2} \cdot M_{propagation \ f_2 \ to \ camera}, \quad (4.17)$$

The goal of this analysis is to create a numerical analysis that will investigate the effects of moving out-of-focus from the coaxial camera, and the influence of the diaphragm on the relation between axial displacement of the target and the resulting location of the reflected image on the camera. To do this, the input into the ABCD matrix consists out of a discrete number of rays being projected from the previously created discrete model of the melt pool. The starting locations of these rays are located along a vertical line that is the 2D melt pool, with each point emitting multiple rays that "sweep" the optic from top to bottom (figure 4.16). These rays then enter the ABCD matrices until the location of the diaphragm, at that point, each ray is examined for the condition $r_{dia} > y_{ray} > -r_{dia}$ and then passed through the rest of the system.

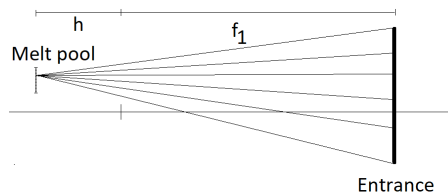


Figure 4.16: Schematic view of discrete rays sweeping the optics.

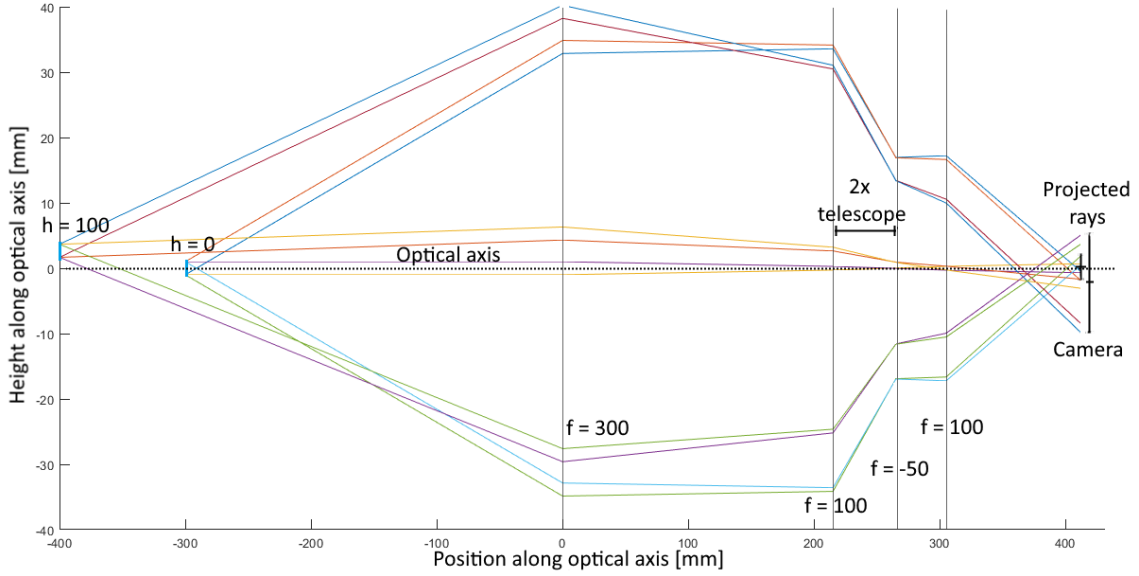


Figure 4.17: Simple ray traced model of the proposed CLT sensor including a 2x telescope.

Using this ray tracing model, a simplified overview has been created in figure 4.17 which shows how the rays travel from the target to the sensor through the optical system.

This overview shows the projected spot of the probe laser beam, based on some preliminary assumptions of the probe laser beam ($w_0 = 2mm$). From the corner of each probe spot, 3 rays are projected into the system. At the end of travel, these rays are incident on the camera sensor to project an image. Using the location where each of these rays hit, the centre and width of the projected spot can be calculated.

Increasing the amount of rays that are projected from the melt pool, and the amount of axial steps that are taken, will increase the accuracy of the modelled system at the cost of sharply increasing computational time. However the advantage of this discrete model is that difficult aspects can be easily modelled using this discrete approach. Furthermore, this ray tracing model has also been expanded by using the discrete melt pool modelled in section 4.3.1 which will allow a more detailed out-of-focus SNR analysis later on.

Model parameters

All of the following figures that have been created with the model (except figure 4.17, for legibility), are based on dividing the melt pool in 10 discrete points, from which 100 rays are emitted into the optical system. Furthermore, the positioning of the target goes from 0 to 100 mm in 5 mm increments. Lastly, the probe laser beam is given an offset of 8 mm from the optical axis, with an initial diameter of 2 mm.

4.4.2 Discrete melt pool model

To further extend the ray tracing model, it is possible to have each ray emitted carry a "charge" which will be projected onto the image. This charge can be set to be a fraction of the intensity profile present on the target as calculated using,

$$P_{ray,r,n} = \frac{I(r)}{N_{angle}}, \quad (4.18)$$

Where $I(r)$ is the Intensity of the melt pool at radius r , N_{angle} is the amount of rays projected from that point, and $P_{ray,r,n}$ is the power contained in the ray emitted. To apply this equation, the shape of the intensity curves of both the probe laser beam and the melt pool emissions must be known. A discrete model of the melt pool has already been developed in section 4.3.1 to calculate the power using a linear temperature profile.

Probe laser modelling

To model the intensity of the probe laser beam on the target, the probe laser beam has been assumed to have a Gaussian shaped 2D intensity profile, determined by,

$$f(x) = ae^{-\frac{(x-b)^2}{2c^2}} \quad (4.19)$$

Based on this equation, 3 parameters must be determined: the location of the centre b is equal to s_κ from equation 4.1. The width c has been set equal to the diameter of the beam at h , using the $1/e^2$ definition:

$$c = \frac{w_h}{\sqrt{2\log(e^2)}}. \quad (4.20)$$

Finally, the area (A) enclosed by the Gaussian is equal to the amount of power that is emitted by the probe laser on the target, and is related to the parameters using:

$$A = \sqrt{2}ac\sqrt{\pi}. \quad (4.21)$$

4.4.3 Position modelling

The first part that will be analysed, is the relations between the axial displacement of the target and the centroid projected onto the camera chip. Figure 4.18 shows the relation between the axial displacement and the location of the centroid on the projected image. This figure also shows that the relation that was expected to be linear, based on the geometry of the system, is instead non-linear. Furthermore it can also be concluded that when the magnification is increased, the maximum axial measurement range decreases. For example, the Baumer TXG-03 monochrome camera, on which the assumptions are based, has a horizontal resolution of 646 pixels. This means that from the centre onwards, the maximum displacement the camera can see is 320 pixels, without considering the diameter of the spot on the image. This also means that the range estimate previously made using a assumed linear system, does not match the results from the ray tracing analysis.

There are multiple possibilities present that could explain the non-linearities present in the model. One explanation is that moving the target out-of-focus, results in the focal planes inherent in the optics being slightly moved while the overall geometry remains the same. This over the complete axial displacement would yield small non-linearities. The other explanation deals with how the centre point is calculated in the model. This is done by taking the rays with the maximum and minimum y-value at the sensor and calculating the halfway point. If the target moves out-of-focus, it also moves away from the optical axis, which as can be seen in figure 4.17 shifts all completed rays upwards. which changes where the centre point is located.

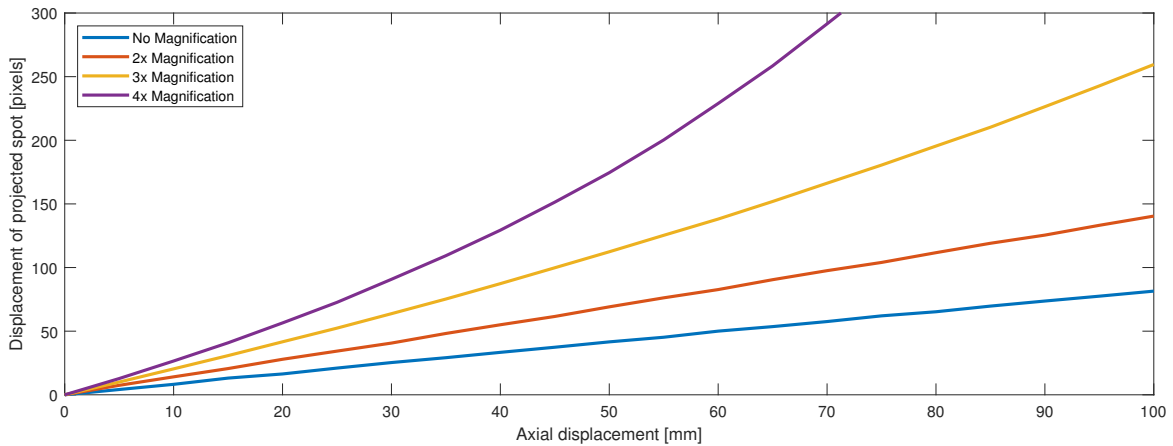


Figure 4.18: Location of the centroid of the projected beam, expressed in the amount of pixels from the optical axis $1 \text{ pixel} = 7.5\mu\text{m}$.

Another aspect that must be considered, is that the addition of a telescope allows for manipulation of the focal plane of the camera set-up. In the case of the Galilean telescope that is proposed, adjusting the location of the diverging lens, will move the focal plane in the axial direction which can be seen in figure 4.19. In this figure it is shown that moving the diverging optic closer to the converging lens, the camera plane will shift axially away from the focal plane of the processing laser beam.

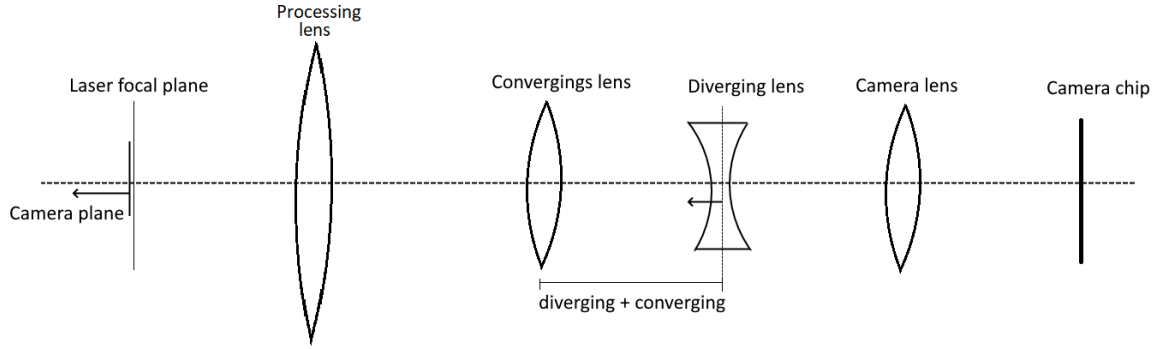
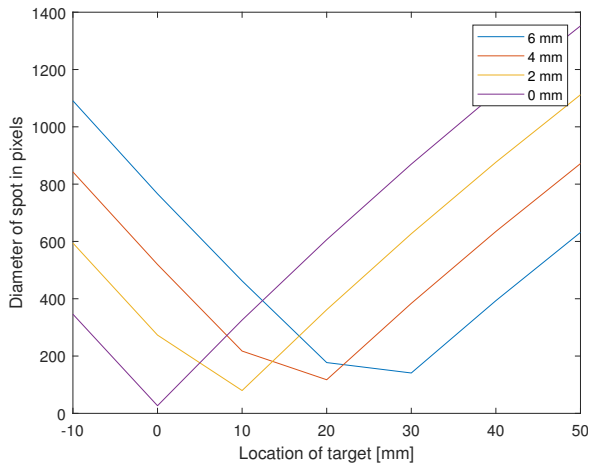
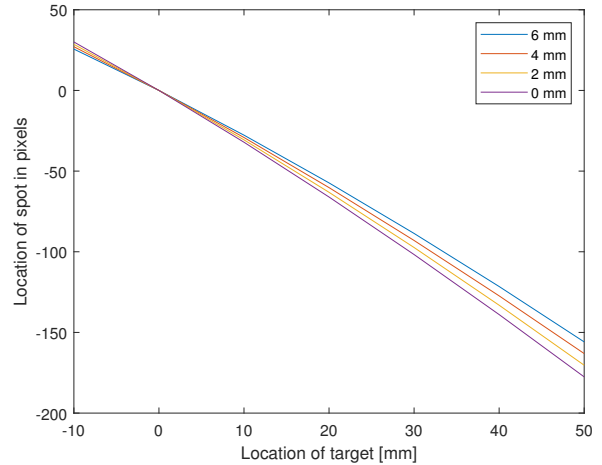


Figure 4.19: Schematic overview of moving the camera focus plane via the telescope.

Modelling this in the discrete model by moving the converging lens between runs, yields the two sub-figures of figure 4.20. These figures clearly show that a slight axial movement in the diverging lens of the telescope, will yield a (relatively) large displacement of the coaxial camera focal plane; Coupled with a small change in the centroid response of the system. Furthermore in figure 4.20a it can be observed that the focal plane of the optical system, where the diameter is minimized shifts as expected. It must be noted that the diameter as modelled, is very large, this is caused by the fact that the diameter was calculated using all rays hitting the sensor. Which leads to the rays that have little impact on the final image (e.g. low amount of light) still being counted for the diameter of the spot.



(a) Diameter of the projected beam as function of the axial displacement of the target.



(b) Location of the centroid of the projected beam, expressed in the amount of pixels from the optical axis $1 \text{ pixel} = 7.5 \mu\text{m}$, as function of the axial displacement of the target.

Figure 4.20: Plots showcasing the effects on the image of moving the converging lens out of position by 0 to 6 mm, limited to -10 to 50 mm of target displacement for clarity.

4.4.4 Combined melt pool and ray tracing model

The last step of the ray tracing model is to combine both the discrete melt pool model (section 4.4.2) and the ray tracing model (section 4.4.1) to model the intensity of the light when it is incident on the camera. This must be investigated because the projected probe beam moves both out-of-focus (along the optical axis) and out-of-axis (away from the optical axis) this means that these effects are compounded, and the resulting image becomes blurry, if the distance from the focal point of the processing lens is increased.

To get an accurate read of these effects, instead of the previously used 10 discrete points emitting 100 rays each, there will be 50 points emitting 500 rays each. This increase is required to ensure that the resulting intensity curve on the camera has sufficient data points to be (relatively) smooth.

The first effect that is known to influence the amount of spread in the image, is the diameter of the opening of the diaphragm. Decreasing the size of the diaphragm will not just decrease the power that reaches the camera, but it will also increase the depth of field of projected image, thus decreasing the amount of blur from operating out-of-focus. This effect is shown in figure 4.21. This figure shows that when the diameter of the diaphragm is decreased, the intensity of the image decreases as well.

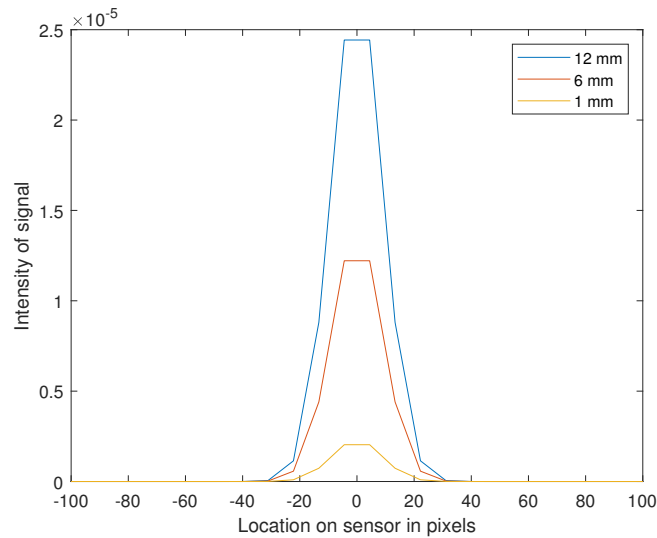


Figure 4.21: Intensity of reflected probe laser light on camera plotted as function of decreasing diaphragm diameter at $h = 0$ mm and $M_{add} = 3$.

Another check on the expected behaviour is to examine what happens with the amount of power remaining (area underneath curves in figure 4.21) after the diaphragm with increasing axial displacement and comparing it with the situation with the diaphragm completely open ($d_{dia} = 12$ mm). This relation is shown in figure 4.22. From this figure it can be concluded that as the diaphragm decreases in size, the power remaining at a certain diaphragm size is relatively linear and consistent across different axial displacements.

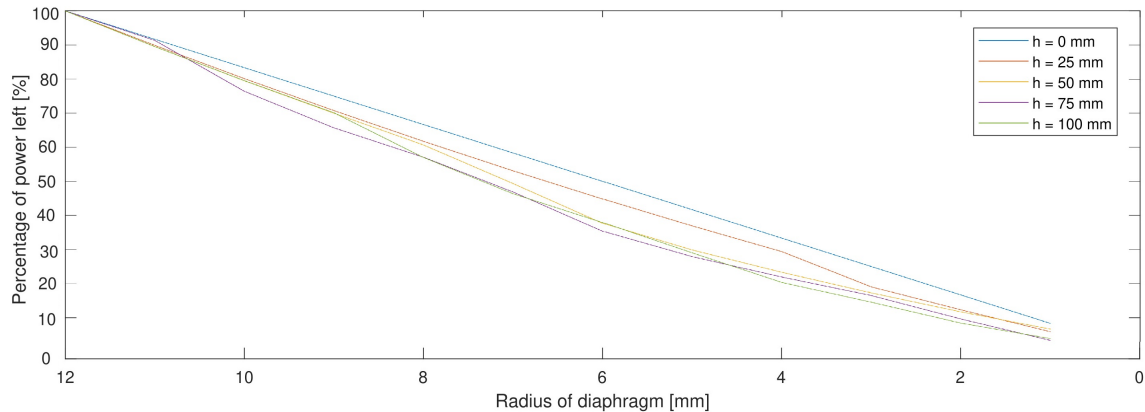


Figure 4.22: Power on projected image for decreasing size of diaphragm.

Examining the differences between a diaphragm diameter of 12 mm and of 1 mm, yields figures 4.23a and 4.23b (figures for situation without a telescope, and with 3x magnification can be found in appendix B). These figures shown that as expected, when the diaphragm size is decreased, the resulting image more tightly focussed due to the increased field-of-view. Which despite the significantly reduced power in the image, would yield a more sharply defined image.

However, it must be noted that in the discrete model used, the power of the probe laser was set at 500 mW. This means that the values that are seen for the resulting diameter of the beam, are based on the complete output of the laser over 1 second. Which, can be observed in the figure will be relatively large compared to the amount of space present on the camera (656 pixels width, versus diameters larger than 300 pixels). However the camera does not take 1 image per second but can be set at much higher frame rates, this higher frame rate means less laser energy hits the camera per image, which will result in the camera "seeing" a projected spot with a much smaller diameter.

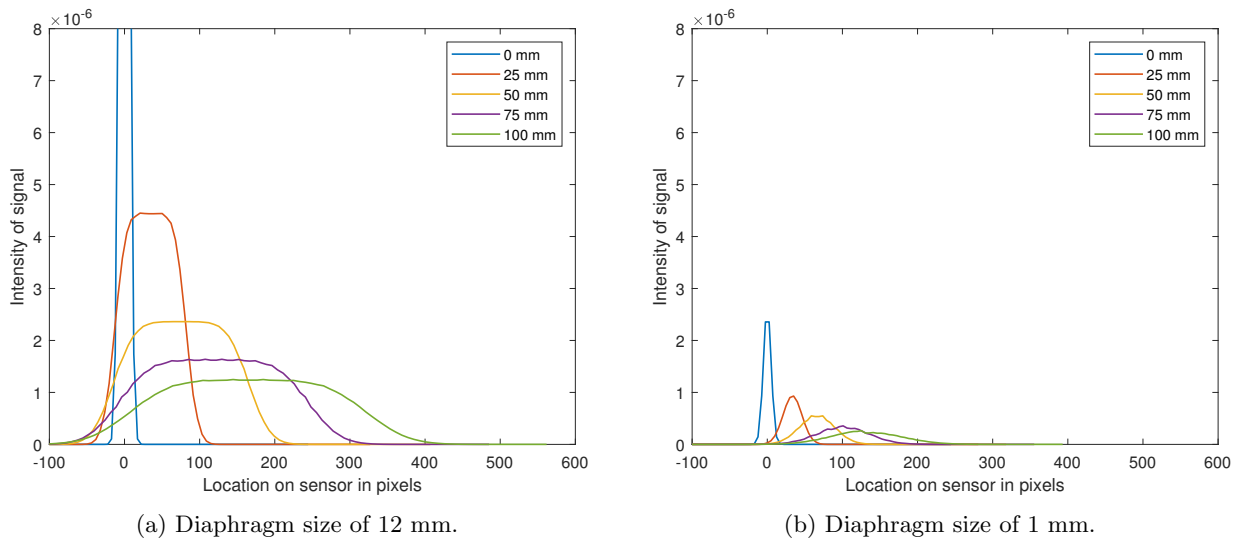


Figure 4.23: Intensity profile of the projected image using a 2x additional magnification as function of differing axial displacements.

4.5 Summary

In this chapter, the different aspects of creating a overall design based on several models where discussed. In the beginning of this chapter, a list was created of the main design variables and their influence on the implementation, together with the components that are already possible to be re-used.

The first model that was created, was directly based on the geometry of the proposed optical system and sought to derive a relation that could be used to determine the axial resolution of the sensor system. It became clear after some analysis, that the system would need to be adjusted and after some analysis, it was chosen to add a Galilean telescope to the system to ensure additional optical magnification.

The second model was based on a simplified optical model and sought to calculate the relation between the properties of the probe laser source, and the amount of light incident on the camera. To do this, the amount of light emitted from the melt pool was calculated using Planck's law and the properties of the existing set-up. From this model it could be concluded that a lower wavelength probe laser source was preferred and that a optical band-pass filter would be required to gain sufficient SNR.

The third model, was created as a consequence of the addition of a telescope and a diaphragm. This model was based on the application of ray transfer matrices, which are a form of ray-tracing. Using this model, the relation between axial displacement of the target substrate, and location of the projected spot on the camera was modelled. Furthermore, using a further expanded model, the influence of the diaphragm on the camera image was also modelled.

Chapter 5

Implementation of a CLT sensor

With the optical components and design selected, the next step is to integrate the designed sensor with the optical laser processing head. This implementation is done in two steps. The first step is to create the mechanical design that mounts onto the head. The second step is to design the software implementation to determine the axial displacement from camera data. Afterwards, the implementation will be tested to derive the final optical properties, to determine the laser properties, and to examine the actual noise present in the system.

5.1 Mechanical implementation

5.1.1 Optics mounting

Since this system is meant as an easily adaptable prototype, it has been chosen to use modular optical tubing supplied from Thorlabs GmbH to construct the telescope. Since this optical tubing uses a special SM1 thread, adapters will need to be designed to connect the optical tubing, to the optical head components from Trumpf GmbH. For this purpose, two adapters were designed (technical drawings in appendix C):

- Cameraport-SM1 thread, used to connect the camera port (beam-splitter) to the SM1 optical tubing, used by the telescope.
- SM1-Camera, used to connect the SM1 tubing with the original camera optics, furthermore, this adapter is also used to house the bandpass-filter.

The overall layout of the optical components are shown in figure 5.1. As mentioned, the telescope has been constructed out of multiple SM1 tubular components (figure 5.2). Thus due to the modular construction of the telescope, it will be possible to easily replace the converging lens with one with a larger focal length, then it is only necessary to insert an additional SM1 section to achieve the required distance between the optical components. Due to this, the choice has been made to mount the converging lenses in a 25 mm SM1 tube, and the diverging lens has been mounted in a slotted 50 mm tube (see table 5.1 for lens information). The slotted tube allows easy access to the diverging lens to ensure the camera focal plane can be easily adjusted in the axial direction.

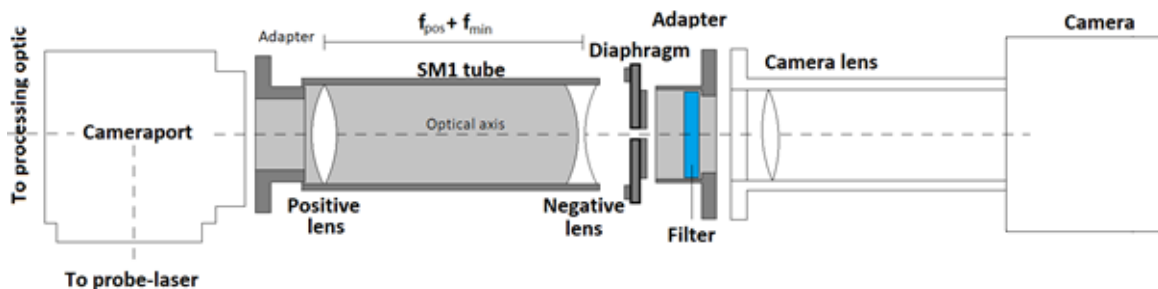


Figure 5.1: Overview of parts needed for the optical components, coloured components are newly implemented, uncoloured components are re-used.

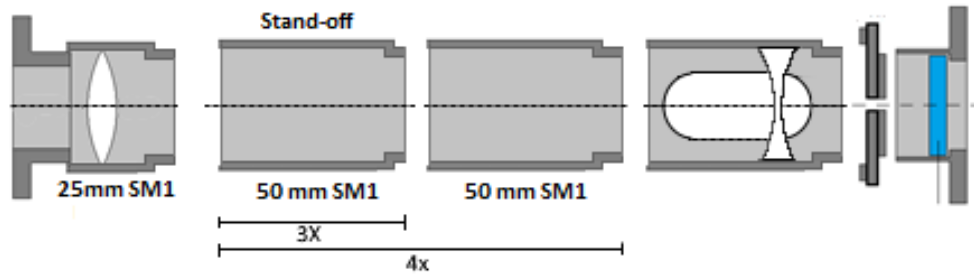


Figure 5.2: Overview of the multiple configurations possible to change the magnification of the telescope.

Table 5.1: Lenses used for telescope.

Uncoated N-BK7 Plano-convex lens	
Lens	Focal length
LA1509	100 mm
LA1433	150 mm
LA1708	200 mm
Uncoated N-BK7 Plano-concave lens	
Lens	Focal length
LC1715	-50 mm

5.1.2 Mounting of the probe laser source

To mount the selected probe laser source to the beam splitter, a mounting system needed to be devised. Due to the geometrical inaccuracies of the mounting of the laser module, this mounting method needs to be flexible enough to allow for slight adjustments in angle to ensure the probe laser beam is inserted perpendicular to the optical axis of the system. Furthermore this system would also need to allow for the required 8 mm of radial offset.

For simplicity, the laser module itself was mounted onto a sheet metal mounting bracket, this bracket was subsequently mounted, using four bolts in the corners, on slots in another sheet metal plate. The positioning of the probe laser module was achieved by using adjustment nuts to allow for precise positioning of the laser module in these slots. A overview is shown in figure 5.3.

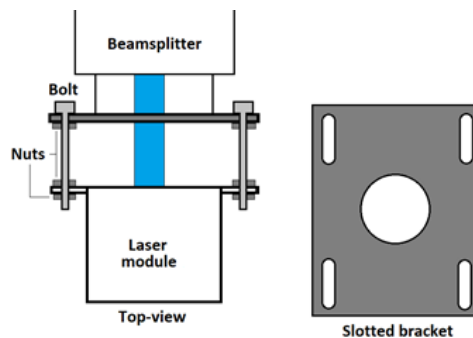


Figure 5.3: Overview of how the laser module is mounted onto the camera port of the coaxial camera system.

5.2 Implementation of image processing

The last aspect that will need to be implemented is the image processing software required to determine the displacement of the reflected beam on the camera. Based on the literature, this can be divided into two different parts:

- Determining the position of the reflected beam on the camera chip.
- "Translating" the location of the projected beam, to the corresponding axial displacement of the target.

In the literature on coaxial laser triangulation [15] [16], the second part is done by assuming a linear displacement profile and fitting calibration data to this linear relation. However the results from the ray tracing analysis are showing that instead of the linear profile reported in the literature (figure 5.4) the displacement curve is non-linear (figure 4.18). This can be solved by using a full calibration to create a look-up table or to interpolate over many points.

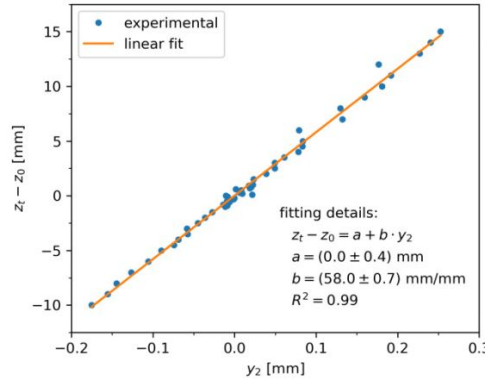


Figure 5.4: Literature based calibration curve of the CLT method, with the target displacement plotted as a function of the location of the centroid on the sensor [15].

However the main issue will be to determine the displacement of the reflected probe beam on the camera. To do this, there are multiple options that come to mind:

- Use image recognition software (like the MATLAB REGIONPROPS function, or other functions of this type), to recognise the circular spot in the image.
- Reduce the problem to a 2-dimensional curve by summing the image perpendicular to the movement of the projected beam then determining the centroid of the resulting curve [15].

To examine which method will be preferred, a set of camera images was created using an early version of the experimental set-up where the probe laser beam was projected onto a piece of paper. The resulting image set was then used to compare three implementations to determine the location of the centroid. The results from this comparison are listed in table 5.2. This table clearly shows that directly using a Gaussian fit present in the MATLAB toolbox to locate the centroid will not meet the stated frequency requirements (30 Hz).

Table 5.2: Processing times for acquiring location of centroid per image. Data taken on mid-range desktop pc (AMD r5 3600x @ 3600MHz).

Method	Processing time [s]	Achievable frame rate
Cftool	0.042	24
Guo	0.0002	5000
Regionprops	0.0025	400

An alternative solution was found by using Guo's method [42]. This method starts by examining,

$$y = Ae^{\frac{(x-\mu)^2}{\sigma^2}}, \quad (5.1)$$

which is of course the Gaussian equation which is non-linear and thus inefficient to fit a curve to. However, taking the logarithm from both sides, will reduce the Gaussian equation into the 2nd order polynomial equation,

$$\ln(y) = \ln(A) - \frac{\mu^2}{2\sigma^2} + \frac{2\mu x}{2\sigma^2} - \frac{x^2}{2\sigma^2}. \quad (5.2)$$

This polynomial equation can then be solved using the weighted average least squares fit which is used in Guo's algorithm:

$$\begin{bmatrix} \sum y^2 & \sum xy^2 & \sum x^2y^2 \\ \sum xy^2 & \sum x^2y^2 & \sum x^3y^2 \\ \sum x^2y^2 & \sum x^3y^2 & \sum x^4y^2 \end{bmatrix} \begin{bmatrix} a \\ b \\ c \end{bmatrix} = \begin{bmatrix} \sum y^2 \ln(y) \\ \sum xy^2 \ln(y) \\ \sum x^2y^2 \ln(y) \end{bmatrix}, \quad (5.3)$$

The parameters a, b, and, c are directly related to the Gaussian parameters via equations:

$$\mu = \frac{-b}{2c}, \text{ and } \sigma = \sqrt{\frac{-1}{2c}}, \text{ and } A = e^{a-b^2/4c}. \quad (5.4)$$

The other alternative approach mentioned, is of course to use a image processing algorithm. In this analysis, the MATLAB function REGIONPROPS has been used to gather data. However the main problem that was found, was that the function was extremely sensitive to noise, which would influence the function to find more circular areas in the image instead of only the projected probe spot. This would imply that additional filtering would be required.

In the end, it was chosen to use the same method used in the originally proposed system [15], and that is to reduce it to a 2-dimensional function, and to fit the resulting function to a Gaussian curve. This is because a 2D image of a Gaussian shape (assumed to fit the shape of the probe-laser), if summed along one axis, results in another Gaussian curve. Furthermore, fitting a 2D curve can be done computationally efficient to ensure that it can be done 30 times per second. Finally due to the compatibility with the TXG03 GiGE camera, the choice was made to implement the image processing in MATLAB.

The process flow that has been implemented in MATLAB is schematically shown in figures 5.5 and 5.6. The first step of this scheme is to acquire the image from the camera, and to isolate the relevant portion of the image to reduce the amount of background noise, and to serve as an additional filter against unwanted internal reflections.

The next step is to sum the pixels in the image in the direction perpendicular to the direction of displacement on the camera, which will yield a 2D curve which hereafter will be referred to as the intensity curve, see figure 5.6. Then to simplify the determination of the centroid, and to further eliminate any further background noise, a threshold is used to isolate the data above this threshold. Then the last step is to fit a Gaussian curve to this dataset to determine the parameters (A , μ and σ) that describes the fitted Gaussian.

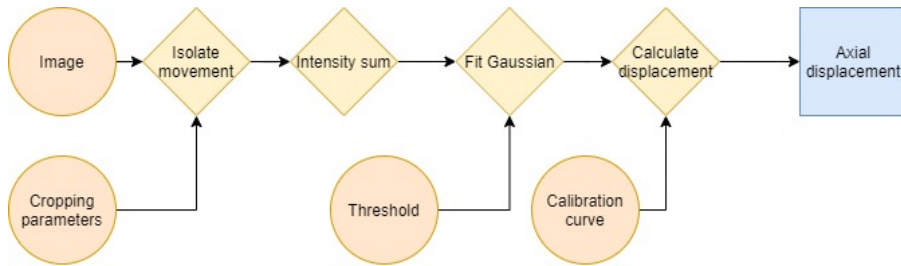


Figure 5.5: Process flow of the implemented image processing software.

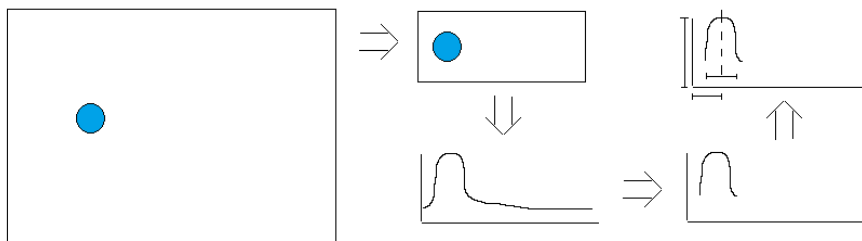


Figure 5.6: Schematic overview of the image processing flow to determine the location of the centroid.

5.3 Evaluation of set up

With the implementation designed, the final design of the CLT sensor is shown in figure 5.7. This figure shows how the system has been implemented. The images show the multiple configurations that are possible for the telescope components, allowing for an additional 1x (i.e. no additional magnification) to 3x magnification. Furthermore after initial experimentation a revised configuration without magnification was devised as shown in figure 5.7d.

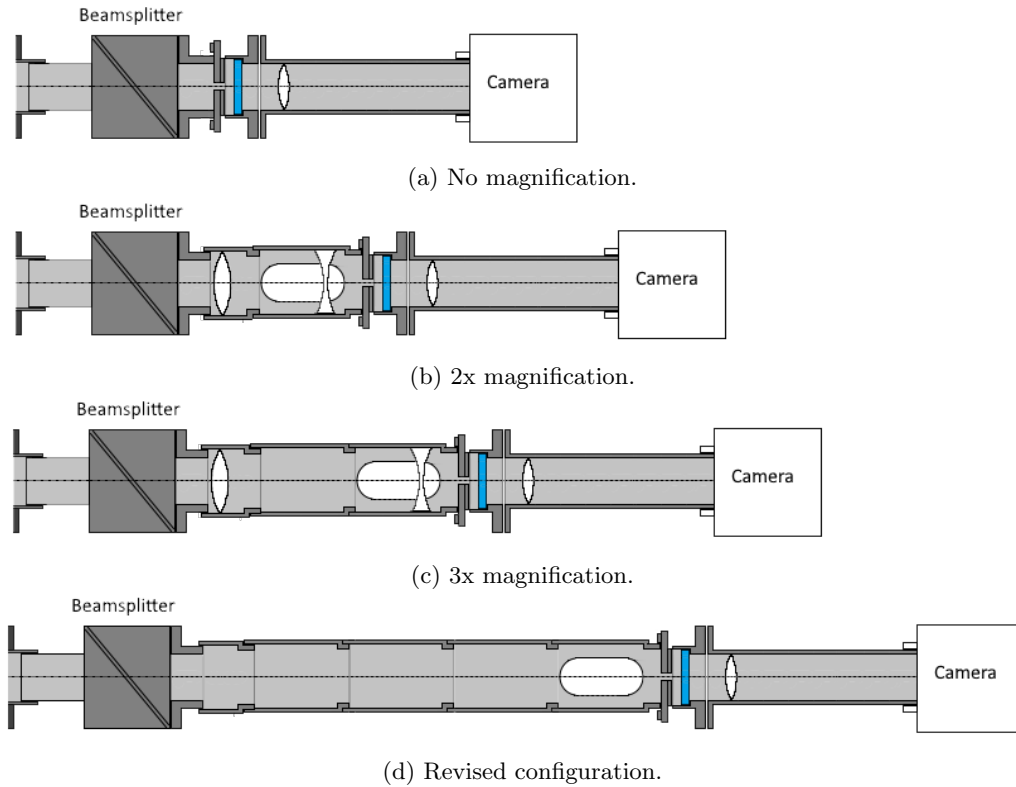


Figure 5.7: Schematic overview of the different configurations of the optical system that have been used during the experiments.

5.3.1 Characterisation of the probe laser

To ensure successful experiments, it will be necessary to know the properties of the probe laser source used. Complete data on the characterisation can be found in appendix D. However a relevant result is the fact that the emitted laser beam is not circular but is instead rectangular (figure 5.8a), which is characteristic for diode laser sources. To properly circularise the laser source, the usual way to do this, is either via a cylindrical lens pair, an anamorphic prism pair, or a spatial filter (see Thorlabs lab facts [43]). In the current set-up, it was decided to simply use a 2 mm circular cut-out on the collimating lens to create a circular laser beam (figure 5.8b).

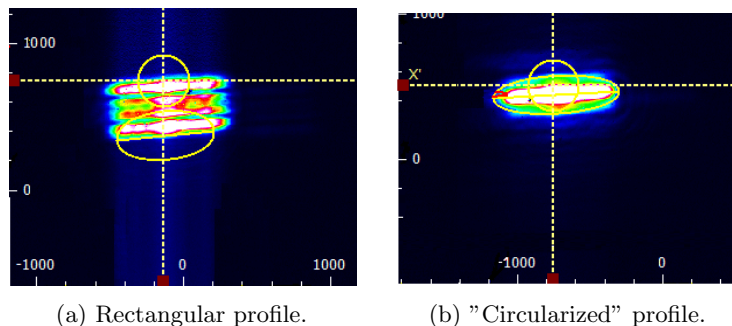


Figure 5.8: Images taken using a beam profiler in the focal point of the 300 mm processing lens.

Another aspect that must be considered, is the alignment of the probe laser beam itself. In section 5.1 it was mentioned that the probe laser source mounting was adjustable along several axis. Using this mounting system, the probe laser source was brought in-line with the targeting laser of the high power processing beam. The result of this calibration is shown in figure 5.9. The probe laser spot is almost exactly centred in the targeting laser in the focal point, and with increasing axial displacement the impact location of the probe laser spot will move along a single axis. This is as expected.

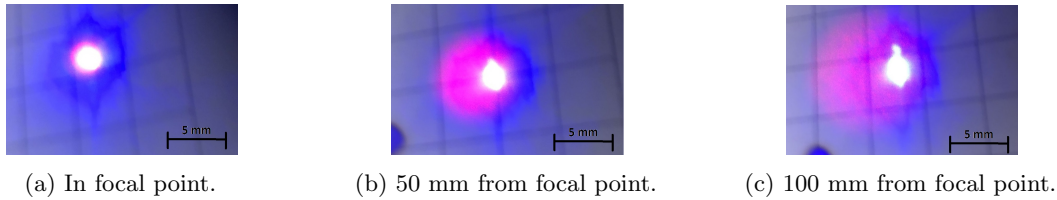


Figure 5.9: Alignment of probe laser (blue/white) with the processing laser's targeting laser (red).

5.3.2 Probe laser power

Another aspect to consider, is to determine if the melt pool emissions are sufficiently suppressed compared to the intensity of the probe laser source. To determine if this is the case, the LMD set-up was used by moving in a single direction while the high power processing laser was turned on with its power increasing in a step-wise pattern. Figure 5.10 shows the power present on the camera image with and without the optical bandpass-filter in place. This was done by summing all the pixel intensities present on the image. A representative image from the set is shown in figure 5.11.

The images clearly shows that without the bandpass-filter in place, the emissions from the melt-pool are noticeable in the image, but are "overshadowed" by the light from the probe laser source. However with the bandpass-filter, the emissions from the melt pool are not present, and ramping the process laser power up to 2 kW doesn't show any increase on the camera. The only noise present in the image is caused directly by the camera.

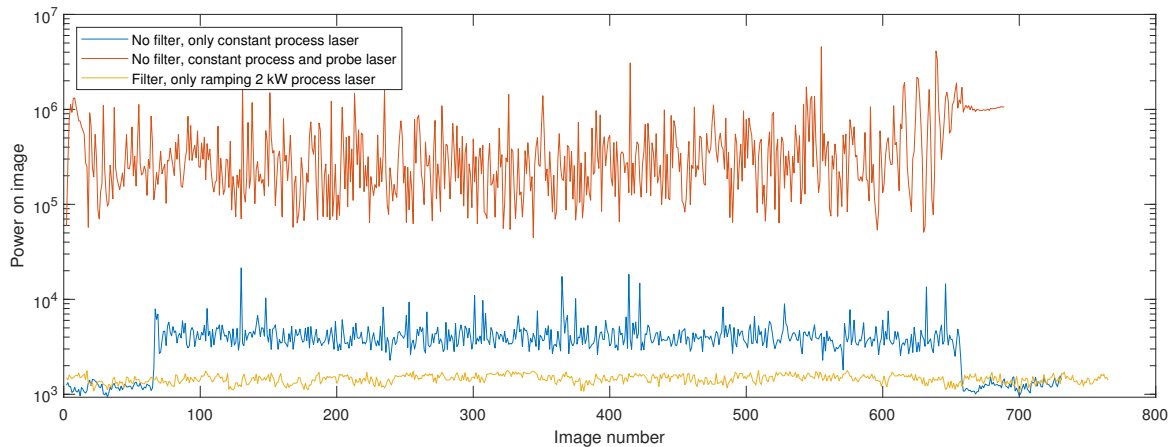


Figure 5.10: Summed pixel intensities over entire image, for multiple runs with logarithmic vertical axis.



(a) No bandpass-filter, process laser (Intensified 100x). (b) No bandpass-filter, process and probe laser. (c) Bandpass-filter, process laser (Intensified 100x).

Figure 5.11: Images captured during verification tests. In which several variables were altered.

5.3.3 Camera field-of-view

With the probe laser module and alignment characterised, the next step is to examine the effect of the telescope on the field-of-view of the camera. This was done using a backlit graduated millimetre scale, see figure 5.12. The field-of-view was calculated by measuring the number of pixels between millimetre ticks and scaling it up to the image size (656x494). The results closely match the expected numbers within the limits imposed by manually measuring the distance between multiple millimetre ticks.

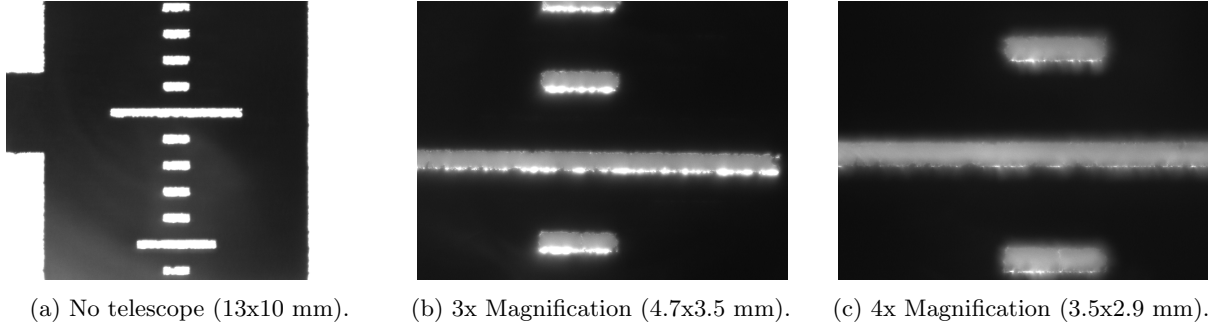


Figure 5.12: Field-of-view images (bxh) on different magnifications.

5.3.4 Internal reflections

The last area of interest in the implemented system, is to examine the internal reflections that are seen by the camera. Figure 5.13 shows some raw images taken during one of the experiments where a target was axially displaced and only the probe laser was turned on. The dot marked by the arrow, representing the probe laser spot, can clearly be seen to be moving along the x-axis in response to an increase in the axial displacement. However the rest of the image shows that there is a lot of extra light (irregular blob) incident on the camera that does not change over time. After some experimentation it was found that this extra light (irregular blob) was dependent on the probe laser offset b_k . This clearly shows that along the path of the probe laser beam, there is/are (a) component(s) that reflect a part of the light of the probe laser directly into the camera optic.

As has been mentioned in section 5.2 a large part of these reflection will be eliminated by cropping the image to contain only the part where the spot of the probe laser beam is. Any internal reflections remaining will be removed via a background subtraction in the software.

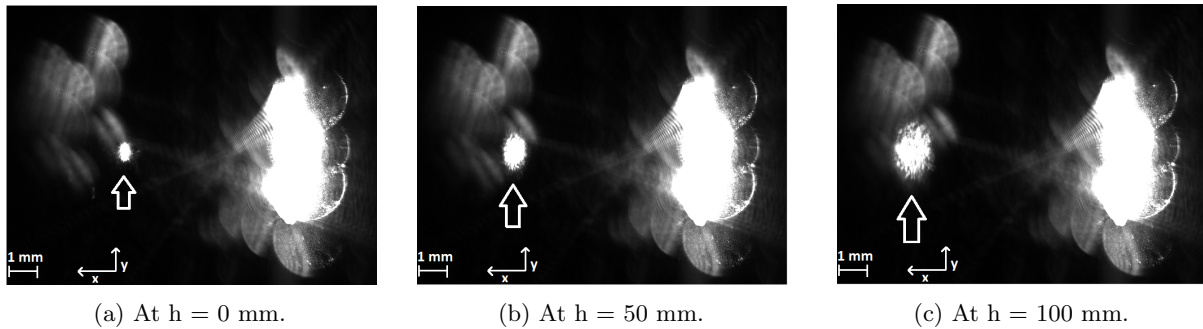


Figure 5.13: Raw camera images taken at varying axial displacement. The marked moving spot represents the probe laser.

Chapter 6

Experimental results and discussion

In this chapter, the results obtained during the experimental phase will be presented and discussed. Some results obtained during the implementation of the design (laser/image properties) have already been discussed in the previous chapter. This chapter has been divided in multiple sections. The first section will discuss the experimental set-ups that have been used to obtain the results, the second section will discuss the different experiments that were performed on these set-ups. The third section will discuss several aspects of the obtained results. The fourth section will discuss a multi-layer experiment that was performed, while the last section will contain a discussion on all the experiments.

6.1 Experimental set-ups

One of the main goals of the experimental phase, is to determine the behaviour of the coaxial laser triangulation system that has been implemented, and subsequently to determine if the sensor meets the requirements that have been set (see section 3.3). To do this, the experimental phase was performed using two different set-ups. The first set-up, hereafter referred to as the "static" set-up, was used to test the implementation (alignment, processing etc.) and to determine the behaviour of the system under "ideal" conditions (no high power processing laser source, precisely known axial displacements). While the second set-up (the "dynamic" set-up) was used to determine the behaviour of the system under operating conditions (i.e. during the LMD process).

6.1.1 Sensor configurations

As has been mentioned in the previous chapter, multiple configurations of the system are possible with the main difference being the amount of magnification supplied by the telescope. A general overview of these configurations can be seen in table 6.1 and figure 5.7. The need for the last configuration will be discussed later.

Table 6.1: Overview of different configurations tested.

Configuration	Lens f_1	Lens f_2	Distance between f_1 and f_2	Overall length	Notes
No magnification	N.A.	N.A.	N.A.	150 mm	
2x magnification	100	-50	30-50 mm	275 mm	
3x magnification	150	-50	80-100 mm	325 mm	
Configuration re- vised	N.A.	N.A.	N.A.	400 mm	Optimized for 400 mm process lens

6.1.2 Static set-up

As mentioned at the start of this chapter, the goal of the static set-up is to test the system under "ideal" conditions to verify if the implementation works, and to initially verify if the image processing yields correct results. In this set-up no high power processing laser source was used. Furthermore, this set-up was used to calculate the accuracy of the system under ideal conditions.

Several of the results from the static set-up have already been shown in the previous chapter and have been used to determine the behaviour of the optics and verify its performance. To investigate the behaviour of the implementation, it was necessary to have the axial displacement of the target relative to the lens (and thus the focal point), to be precisely known. To achieve this, a precision displacement table manufactured by Physik Instrumente GmbH (table 6.2) was placed in front of the laser processing head (figure 6.1). Using this table, it was possible to precisely set the axial displacement h of a target relative to the focal point, to characterise the behaviour of the sensor.

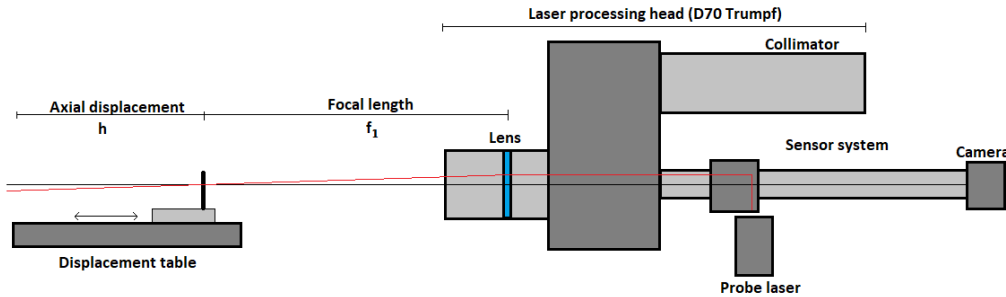


Figure 6.1: Schematic overview of the static configuration with precision displacement table.

Table 6.2: Specifications of the precision table. Sourced from [44].

Manufacturer	Physik Instrumente GmbH.
Model	M-404.4DG
Controller	C863 Servo Controller
Travel range	100 mm
Repeatability	0.5 μ m

It must be noted that the main disadvantage of the static set-up is that the target the probe laser was projected on, was a piece of paper or metal. Of course in practise, during the LMD process, the target is a molten pool of metal, this was assumed to change the behaviour of the sensor, due to the shape of the bead and the presence of a stream of reflective metal powder, common in LMD.

6.1.3 Dynamic set-up

To test the behaviour of the sensor during the LMD process, the sensor system was implemented on the optical head of to the high power processing laser source, with the main difference being the use of a 400 mm focal length process lens, instead of the 300 mm process lens used in the static set-up. This difference in focal lengths will slightly lower the axial resolution of the system, however since the focus of this set-up will be to analyse the behaviour of the sensor system when additional process variables are introduced, this reduced axial resolution will be largely irrelevant.

6.2 List of experiments

For each of the experimental set-ups previously mentioned, different experiments were performed to gather the data required to assess the performance of the sensor.

6.2.1 Static experiments

As mentioned earlier, the static set-up (section 6.1.2) was used to verify the implementation as presented in section 5.3. This was done with a variety of methods ranging from manually moving a piece of paper to precise movement of the displacement table.

To compare the behaviour between different implementations and variables, measurements were taken while the displacement table was set to a certain movement pattern. This movement pattern was a 1D scan with a 1 mm interval, each lasting 0.3 seconds, over the defined range of 0 to 100 mm. This scan was repeated 6 times to allow statistical analysis. The resulting pattern, and the sensor output are shown in figure 6.2. This figure clearly shows that for each axial displacement, there are 6 different measurements at that displacement spread out in time (sample rate $\sim 2\text{-}3$ Hz). Using these measurements, it will be possible to investigate how precise the location of the projected spot on the camera can be located, giving a measure of the accuracy which will be discussed later.

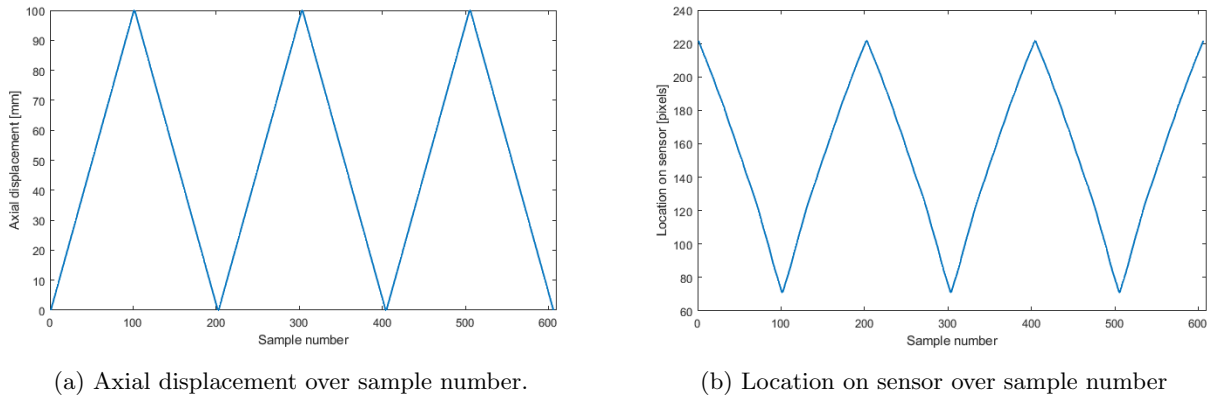


Figure 6.2: Displacement pattern used in the experiments on the static set-up with resulting output from the sensor.

6.2.2 Dynamic Experiments

To characterise the system when dynamic aspects are in play, four different experiments were performed.

The first set of experiments was done by displacing the robotic arm, to which the optical processing head including the sensor is connected, in the axial direction, which should eliminate any "wobbling" of the optics. The displacement in the axial direction was done in 5 mm intervals, each interval lasting for 2 seconds. A representative result from the sensor output is shown in figure 6.3 below. This figure clearly shows that each 5 mm axial step has a corresponding step in the output of the sensor.

The second set of experiments used a set of metal plates (25 mm thickness) stacked to form a "staircase" with 50 mm intervals (figure 6.4a), while the processing head was moved in a horizontal line with a speed of 10 mm/s. Afterwards, these images were processed to calculate the location of the probe spot in the camera image. Thus as can clearly be seen in figure 6.4b, the axial displacement measured by the sensor was increased in fixed intervals.

The third set of experiments were targeted at investigating the impact of the LMD process on the behaviour of the sensor. This was accomplished by having the optical processing laser head follow a pre-programmed track, that would be used to deposit a clad bead. This track would then be repeated multiple times, each time activating another aspect of the LMD process, see table 6.3.

The last experiment that was performed, is like the previous one, except that when depositing the next bead, the processing head is moved upwards by 0.1 mm. After this has been done 50 times, a multi-layer "wall" will have been created. The goal of this experiment is to use the sensor to monitor the entire depositing process needed to form the wall.

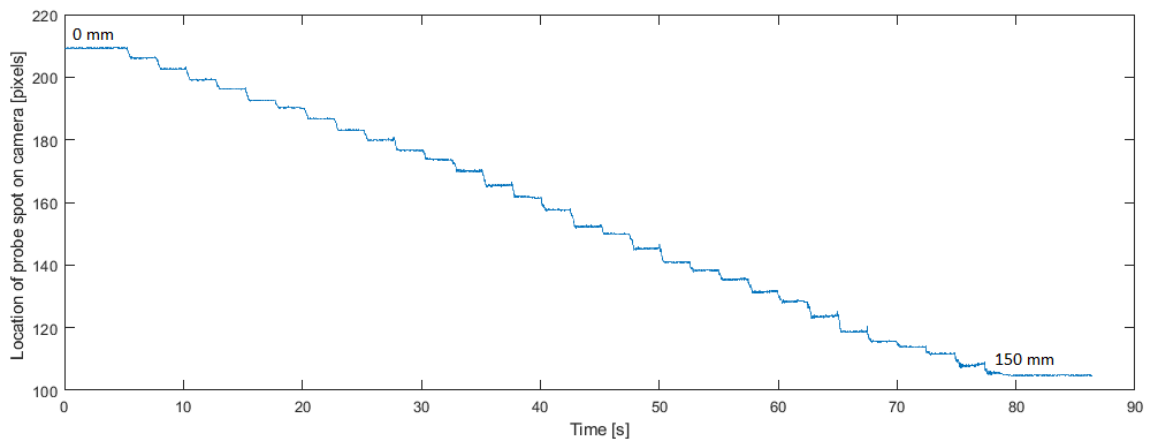
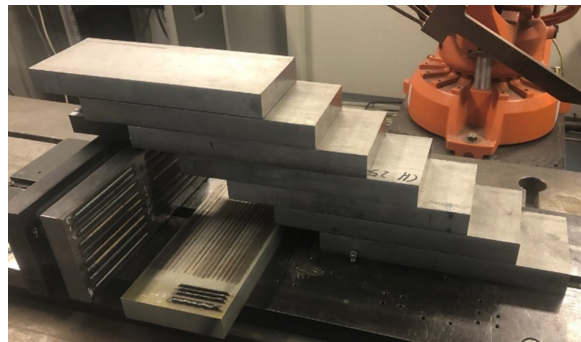
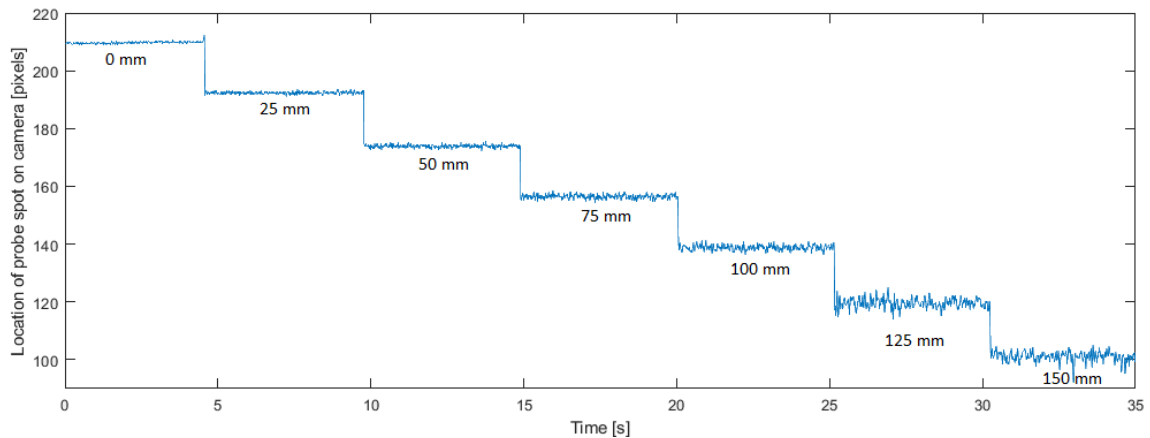


Figure 6.3: Sensor output (location of probe spot on the camera sensor) from 1D axial scan as function of time.



(a) Test target set-up, consisting of a "staircase" built from metal plates.



(b) Sensor output.

Figure 6.4: Location of the probe spot when used to measure the "staircase" used in horizontal scanning.

Table 6.3: Parameters for each subsequent run.

Name	Probe laser	Powder feed	Process laser
Probe only	ON	OFF	OFF
Powder test	ON	ON	OFF
Bead laying	ON	ON	ON
Examining bead	ON	OFF	OFF

Issues with original set-up

Unfortunately, over the course of the experiments performed on the dynamic set-up, with one of the implemented configurations (2x telescope), severe issues were found with the measurements taken. These issues included: the system not meeting the requirements, and an extremely large variance in the obtained results. An example of the results obtained during these experiments, is shown in figure 6.5. This figure shows that the results from the early configuration have the following problems:

- Large deviations (± 10 pixels, which equals circa ± 3 mm of axial displacement of the target) from the mean in the "stable" parts of the result.
- Significant spikes are present in the results (e.g. at image number ~ 350), these spikes are caused by a "flash" in the image which the image processing cannot properly correct (example shown in figure 6.6).

The result of this, is that the data obtained during experiments with LMD depositing, is of much lower quality than expected based on "static" experiments which will be discussed in section 6.3.1.

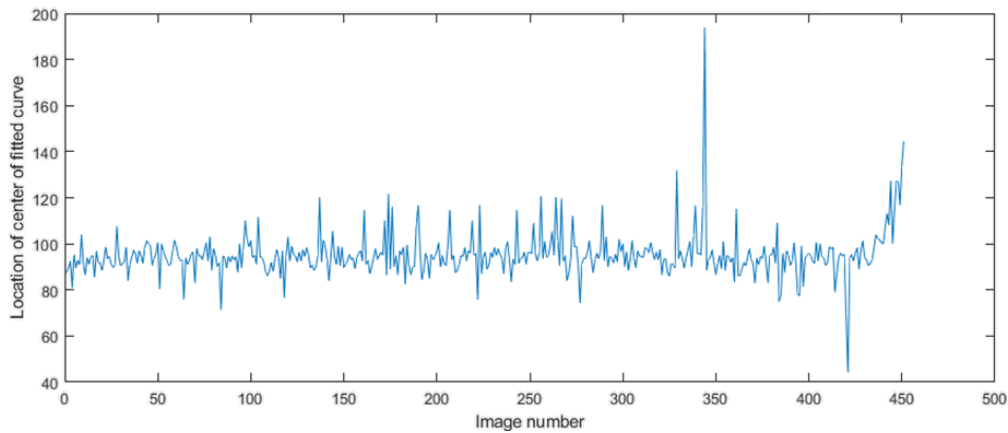


Figure 6.5: Sensor output from 1D scan during LMD, using the old configuration.

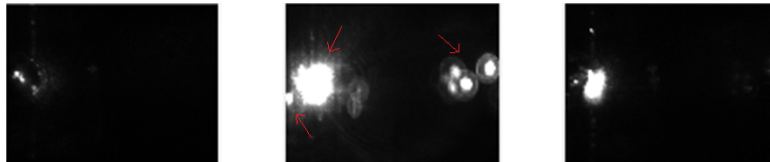


Figure 6.6: Three consecutive images showing the "flashes" as recorded by the sensor (spike around image number 350).

Two other issues were also observed after the configuration had been analysed:

- The optical tubing used, and the mounting on the top-cover where not rigid enough. Due to this, when the robotic arm moved the laser processing head to perform the experiment, the calibration of the set-up was lost (an example is shown in figure 6.7).
- The optical axis of the sensor system was not fully in line with the geometric axis of the optical tubing (deviation of approximately 12 mrad), this implied that during alignment, when the resulting image should have been in the centre of the camera, it was instead at the edge (seen in figure 6.6). This also sharply reduced the maximum measurable displacement, since the projected probe spot (moving from right to left) would quickly reach the rightmost edge of the sensor image.

Overall, these issues, combined with the accuracy results obtained using the telescope (see section 6.3.2), led to the creation of a revised implementation, based on the original design from literature [15]. Furthermore, the optical tubing was mechanically reinforced due to the addition of a clamp halfway on the tubing, which is shown in figure 6.8. This new implementation does not support additional magnification since the diaphragm has been mounted in the common focal point of the process lens and the camera lens, thus the data generated using the old implementation in the static set-up, will be used where relevant.

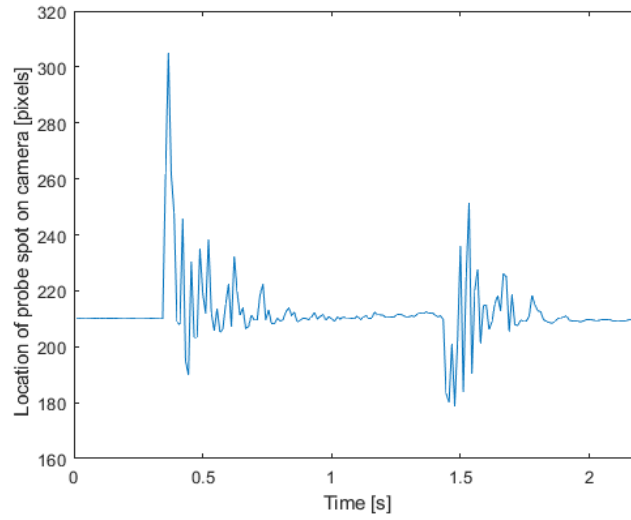


Figure 6.7: Vibration present in the testing data when robotic arm holding the processing head and sensor starts moving.

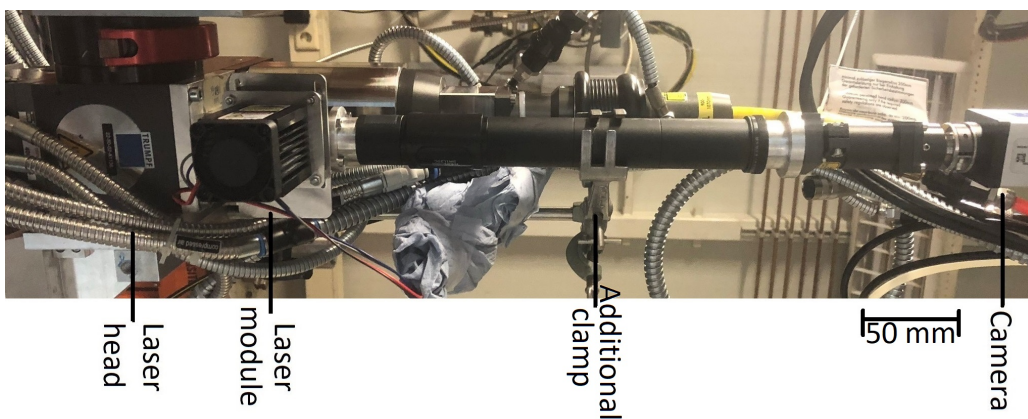


Figure 6.8: Photograph of the revised set-up with an additional clamp, mounted on the laser processing head for laser cladding.

6.3 Experimental results

In the following, the overall results have been split into multiple subsections dealing with the different aspects of the sensor system. The first section that will be discussed, is the overall calibration of the sensor. By this, the curve representing the position of the projected spot on the sensor and its corresponding axial displacement is meant. This will be discussed using both the static and the dynamic experimental set-ups (section 6.1.2 and 6.1.3). The second aspect that will be discussed, is the overall precision of the implemented sensor system, based on the data obtained from the different calibration experiments. The third discussion is partially a continuation of the second, focussing on the influence of the different LMD additions on the accuracy and calibration of the system.

6.3.1 Calibration of system

One of the first aspects that must be investigated, is the relationship between the location of the projected spot in the camera image and the actual axial displacement of the target. Knowing this relationship, will give knowledge about the axial resolution of the sensor. Furthermore in the theoretical model (see section 4.4.3), non-linearities were present, when the diaphragm is decreased in size. It is necessary to investigate this behaviour to determine if the ray tracing model previously used, gave accurate results.

Influence of magnification on calibration

The first behaviour investigated, is the influence of the magnification on the calibration curves of the system. The results of these experiments together with the theoretical results from the model are shown in figure 6.9, where the different calibration curves have been adjusted to use the relative displacement from the starting point. The values on the displacement curve are derived from the average value during the experiment at each axial displacement, relative to the starting position. The figure clearly shows that, as expected, the displacement of the projected spot almost linearly increases with the magnification. Calculating the slope of these curves, will yield the axial resolution of the sensor (see table 6.4). It must be noted that the experiment with the 3x magnification has been limited to a maximum displacement of 50 mm, due to the maximum sensor size. Furthermore, the behaviour of the revised implementation is also shown.

As experiments with a telescope configuration on the dynamic set-up with the 400 mm lens failed these results are based on the experiments on the static set-up.

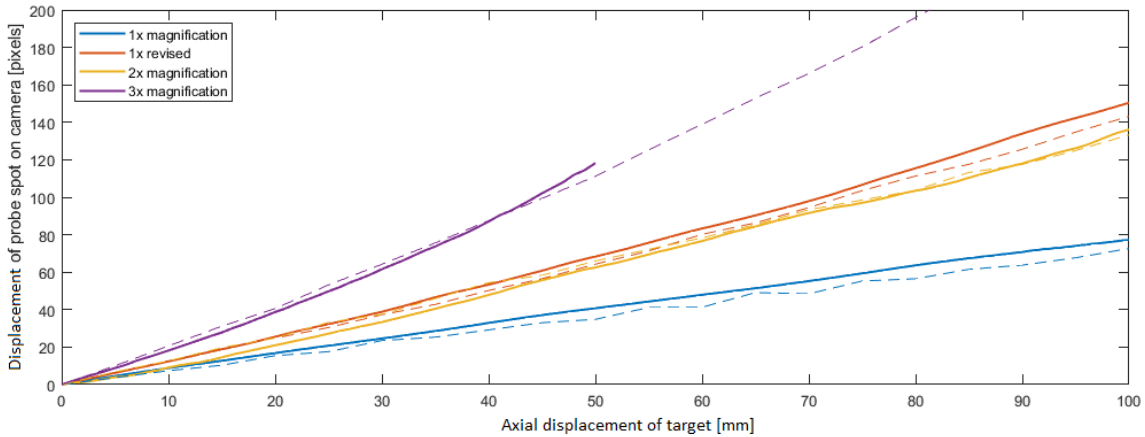


Figure 6.9: Relative displacement of projected spot for multiple magnifications and the revised implementation. Dotted lines are the theoretical results from the model (section 4.4.3).

Table 6.4: Results from each plotted curve.

Configuration	Displacement [pixels]	Slope [pixels/mm]	Resolution [mm/pixel]
1x	77	0.77	± 0.65
Revised	150	1.5	± 0.33
2x	140	1.4	± 0.35
3x	118	2.3	± 0.2

Influence of diaphragm on calibration

The next results to examine, are what happens to the calibration curve, when the diaphragm is decreased in size. In the model this resulted in a increasingly non-linear displacement curve of the set-up. To examine this, the results from the static experiments with the telescope configurations will once again be used and contrasted with the revised implementation.

Figure 6.10 shows the different results from the experiments, relative to the starting position, together with the expected behaviour derived from the model. Figure 6.11 shows the same displacement curve for the revised system, but with a variety of diaphragm sizes applied. It can be seen in this figure, that increasing the diaphragm size influences the displacement of the projected spot on the camera. Figure 6.12 shows the raw image footage used to calculate this, together with the result from the image processing. One of the conclusions that can be drawn from this image, is that as seen in section 4.4.4 the diameter of the projected probe spot, is dependent on the size of the diaphragm, but also on the integration time used for the camera. Due to these factors, a direct comparison with the results obtained in section 4.4 cannot be made.

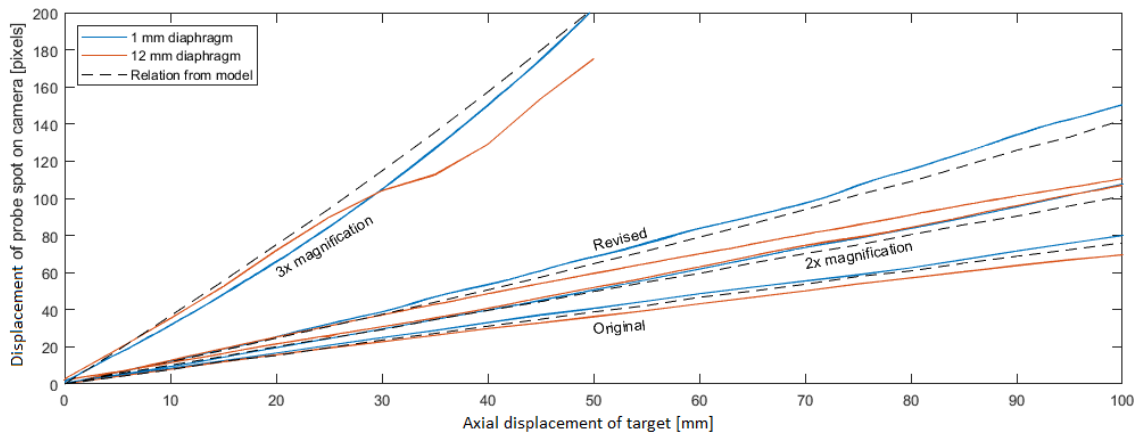


Figure 6.10: Relative displacement curves from static experiments with varied diaphragm. Dotted lines are the theoretical results from the model (section 4.4.3).

The overall conclusion that can be drawn from these effects, is that decreasing the diaphragm size will decrease the overall resolution of the sensor (slope of curves in 6.11). So overall a large (or no) diaphragm will be preferable but since this will increase the amount of noise, the effect on the accuracy will be examined in section 6.3.2.

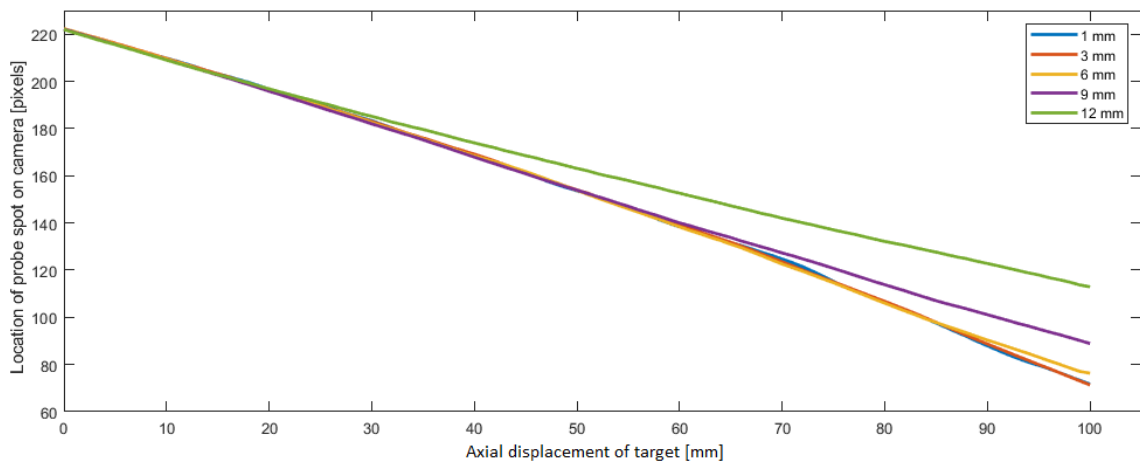


Figure 6.11: Calibration curve of revised set-up with variable diaphragm size.

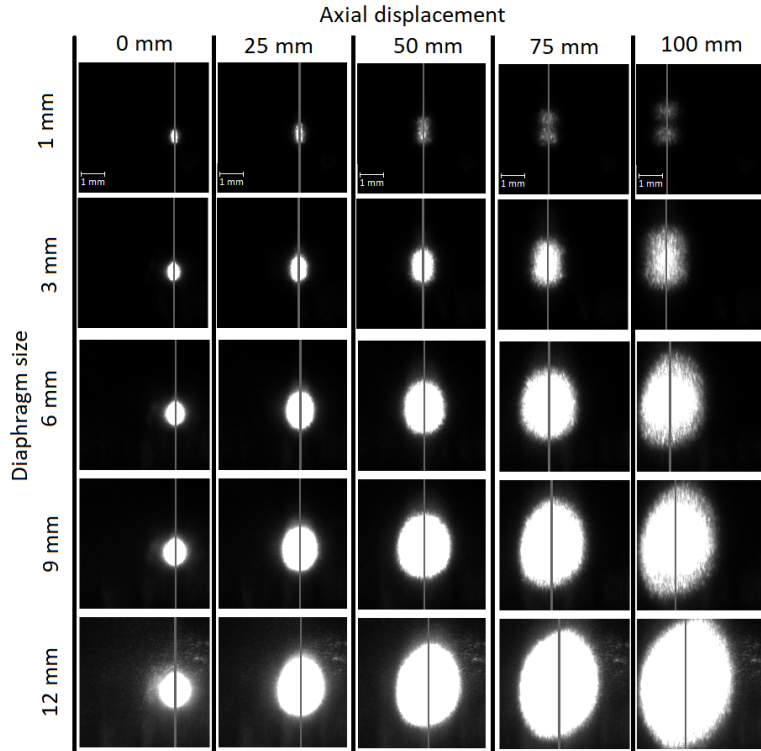


Figure 6.12: Raw images taken using the revised set-up with variable diaphragm size for increasing axial displacement. Grey line indicates the calculated centre of the laser spot. The images have a field of view of 5x5 mm.

Comparison to dynamic set-up

The last aspect to be considered is that the dynamic set-up uses a different focal length of the processing lens than the static set-up. Thus it is important to quantify the different calibration curve that this results in. As mentioned before, due to issues with the telescope configurations during LMD, the revised implementation of figure 6.8, will be used to gather the results.

The overall calibration curves with the processing lens with focal length 300- and 400-mm are shown in figure 6.13. An important consideration is that due to the $f = 400$ mm processing lens, the overall displacement of the centroid of the probe spot on the camera image, over the specified axial displacement of the target has been decreased significantly, which matches the results from the theoretical model.

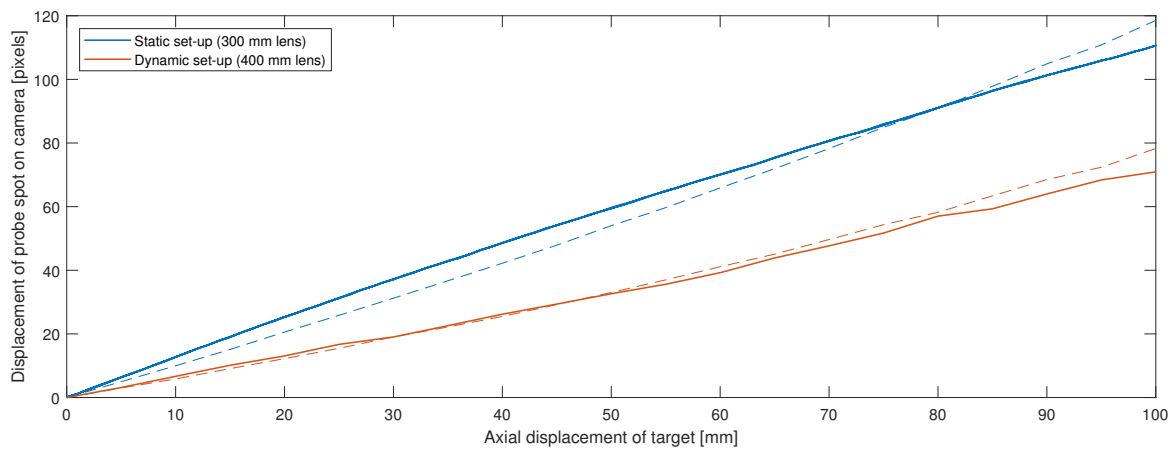


Figure 6.13: Displacement curves of the static and dynamic set-ups. Dotted lines are the theoretical results from the model (section 4.4.3).

6.3.2 Accuracy of the sensor system

For the sensor system to meet the accuracy requirements of ± 0.1 mm, the accuracy of the actual sensor needs to be determined. The accuracy in this system can be said to consist out of two different components:

- Accuracy of the calibration: how accurately the relationship between the location on the camera and the axial displacement has been mapped.
- Accuracy of the fitting: how accurately the location of the image (centroid) on the camera has been determined using the image processing described in section 5.2.

In the previous section, it has been shown that calibration curves for multiple different configurations exist and have been mapped. Thus it can be assumed that any error in this part will be static. Thus it can be concluded that the primary source of inaccuracy/noise present in the results, will be caused by small deviations in the image of the probe spot projected onto the sensor. Thus in this section, the precision of the sensor will be discussed in terms of the accuracy of the calculated location of the centroid of the probe spot on the image. This has been defined for this purpose as the range that contains 95% (2σ) of the measurements taken at a fixed axial displacement,

$$\sigma = \sqrt{\frac{1}{N-1} \sum_{i=1}^N |x_i - \bar{x}|^2}, \quad (6.1)$$

where N is the number of samples and x_i and \bar{x} are individual values and the mean of x respectively. Thus in both experimental set-ups, the images taken at a fixed (known) displacement, can be used to calculate the standard deviation (and thus the error) of the fitting at that axial displacement. Multiplying this fitting error (in pixels) with the resolution (in mm/pixel) will yield the accuracy of the sensor at that displacement.

Sources of inaccuracy

The first thing that can be done with the data obtained during the experiments; is to examine what the causes are of the inaccuracies in the fitting process. To ensure vibrations and other sources are not considered, data gathered from the static set-up will be used. In the dataset that has been chosen to be used for this analysis, the mean of all the fitting errors (2σ) over the displacement is ± 0.18 pixels, while at the axial displacement chosen for this analysis ($h = 50$ mm), the fitting error is ± 0.29 pixels, which is the reason this displacement was chosen.

Figure 6.15 shows the six different images that were processed, together with the intensity profiles along the horizontal axis. Examining these images yields very little information. To amplify the problem and visualize it better, figure 6.14 shows the the (amplified) differences between the individual images, and the mean of all intensity profiles.

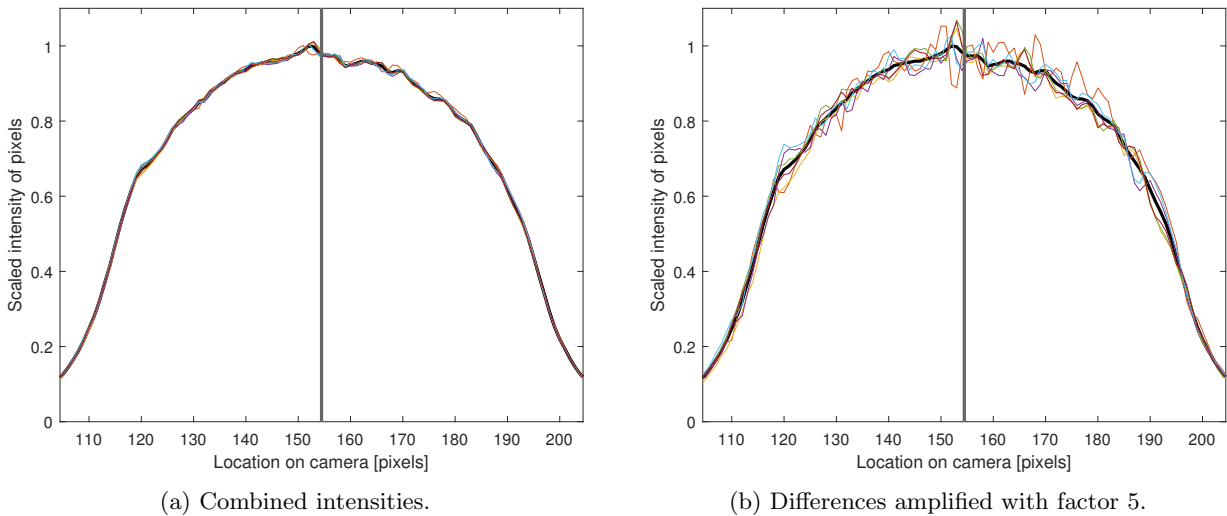


Figure 6.14: Composition of all intensity profiles, plotted versus the mean profile (black) and the spread of the calculated centre (vertical line ± 0.29 pixels).

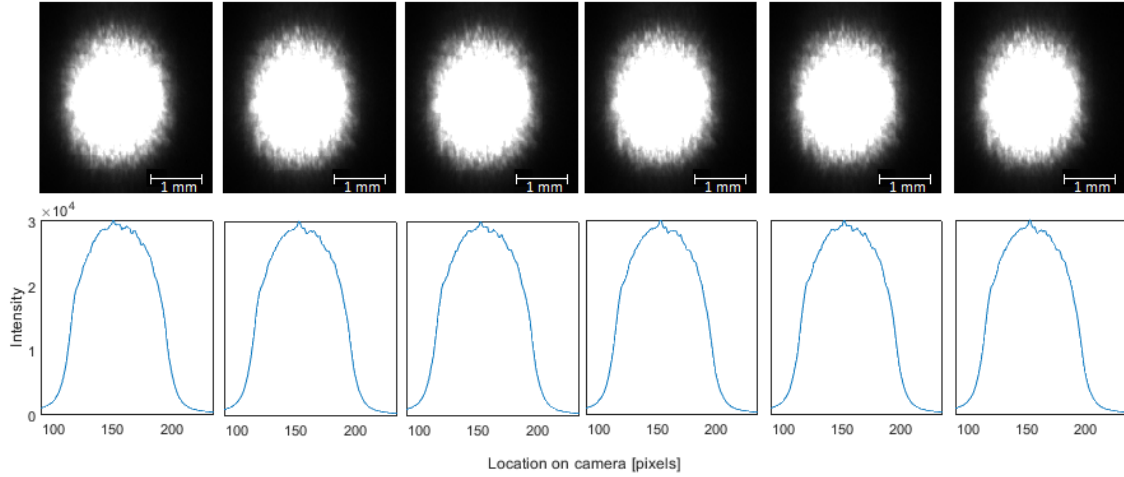


Figure 6.15: Images taken at $h = 50$ mm with $D_{dia} = 6$ mm, with the corresponding intensity profiles ($N=6$).

From figure 6.14 it can be concluded that there are only very small differences between the different images, but these are sufficient to create small deviations. According to the results, the average deviation of the intensity profiles from the mean profile is around 1%. This small deviation could be caused by several different sources such as:

- Temporal power instability of the probe laser source.
- Speckling of the probe laser on the target (as seen in the "halo" around the projected spot).
- Small movements of the target.
- Noise inherent to the camera (referenced in the manual [35], however considered negligible due to gain set to 0 dB).

Influence of magnification

The first thing that will be discussed in terms of the configuration, is whether the implementation of a Galilean telescope will improve the accuracy of the sensor sufficiently to meet the stated requirements. To do this, the data that gathered using the static experiment (section 6.2.1) was processed to calculate the standard deviation using the 6 data-points for each location along the scan spread out over time. The results for all configurations (telescope and revised) are shown in figure 6.16. The first figure has been calculated in terms of the fitting accuracy (i.e. how much deviation is present in the image), and the second figure has been calculated in terms of the overall accuracy (i.e. the corresponding deviation in axial displacement).

These figures show that overall the configuration without telescope, and with the 2x magnification are in the same ballpark when it comes to the fitting error (around ± 0.2 pixels), this indicates good performance during image processing. However the 3x telescope has a much-reduced quality of fitting which despite the increased resolution result in a lowered accuracy.

Influence of diaphragm diameter

The next step is to investigate whether the size of the diaphragm impacts the accuracy of the system. To determine this, the results from the different implementations have been gathered and are shown in figures 6.17 and 6.18. These figures show that narrowing (reducing the diameter) the diaphragm has a negative influence on the accuracy of the sensor system that is approximately the same over the different configurations. However it must be noted that the error in the revised system is relatively "cyclical" over the displacement while the error of the older configuration is much less stable over the range.

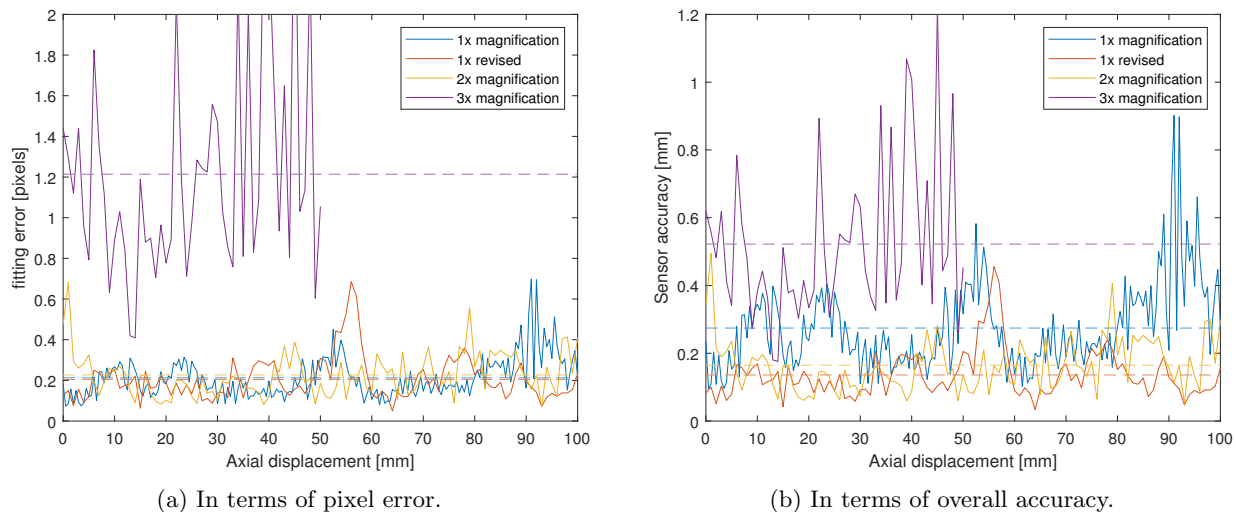


Figure 6.16: Fitting error and system accuracy given in terms of implemented magnification, the dotted lines show the mean of the dataset. Diameter of diaphragm is 1 mm.

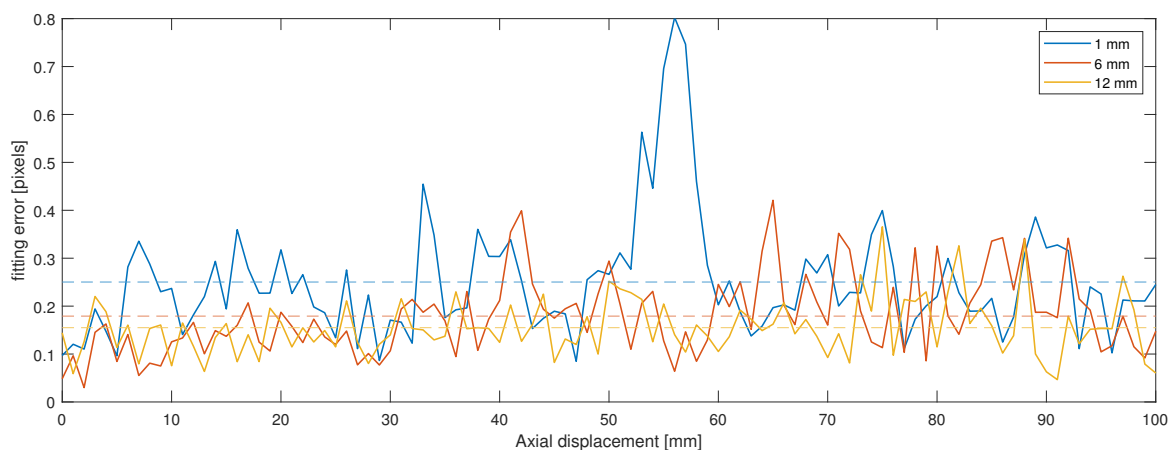


Figure 6.17: Fitting errors of the revised system given for varying diaphragm size, the dotted line shows the mean fitting error.

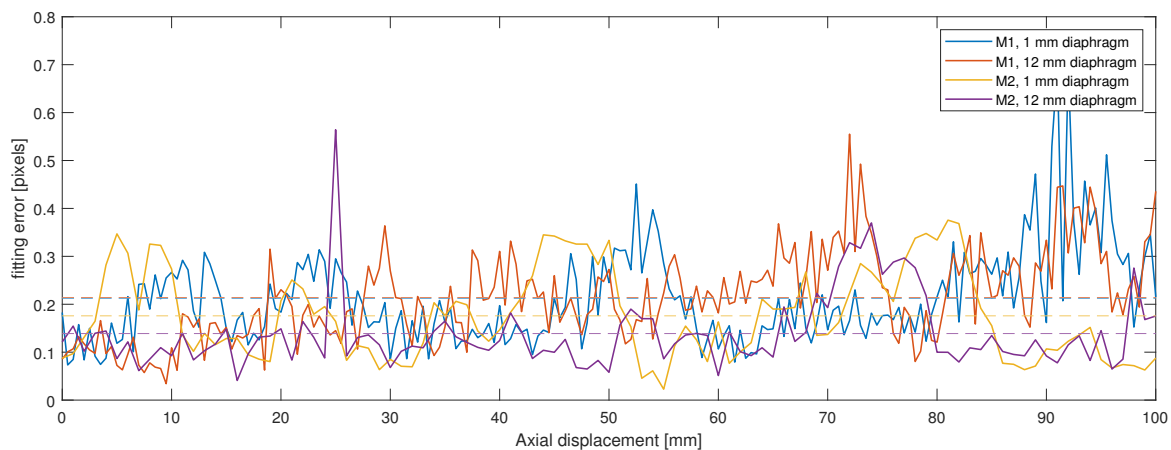


Figure 6.18: Fitting errors of the old configurations given for varying diaphragm size, the dotted line shows the mean fitting error.

Influence of static versus dynamic set-ups

The last step in the initial calculations, is to investigate the difference between the experimental results of the different set-ups. This is done using the revised configuration (see figure 6.8) since it is operational on all set-ups. The results of this are shown in figure 6.19. This figure shows that there are large differences in the calculated accuracy of the different set-ups. The large difference between the static and dynamic experiments, can largely be explained by the differing focal length of the process lens (focal length of 300 vs 400 mm).

The increasing difference between accuracy of the axial movement and the lateral step pattern over the axial displacement, clearly indicates that a variable in the image changes with it. Figure 6.20 shows the images taken at certain displacement during the experiments. In these images, it can be seen that the quality of the projected spot of the lateral movements has degraded compared to the images from the axial movement, investigation yielded that this degradation is caused by the interference pattern generated by the probe laser on the different metal plates. When the probe laser is moved laterally this pattern changes quickly which introduces more noise.

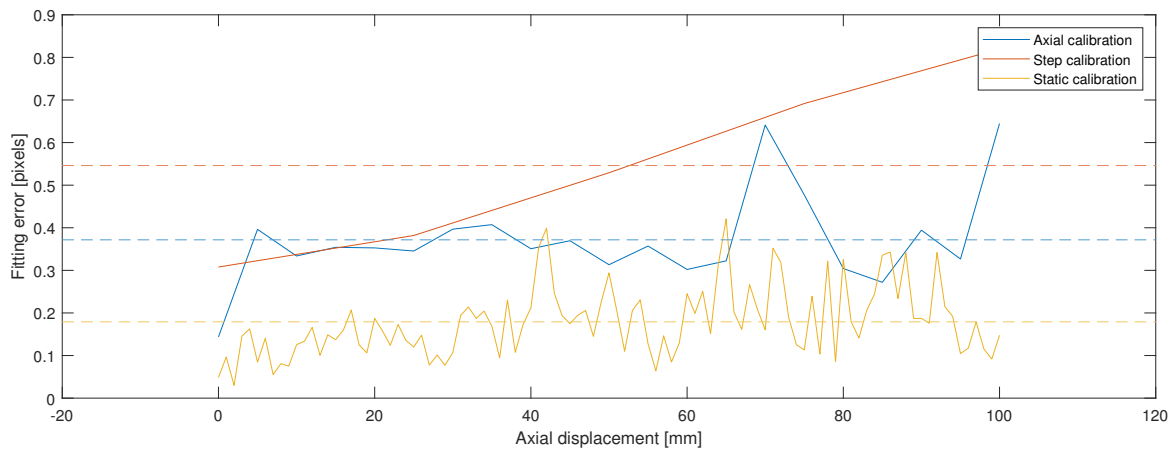


Figure 6.19: Fitting errors calculated for the different calibration set-ups used.

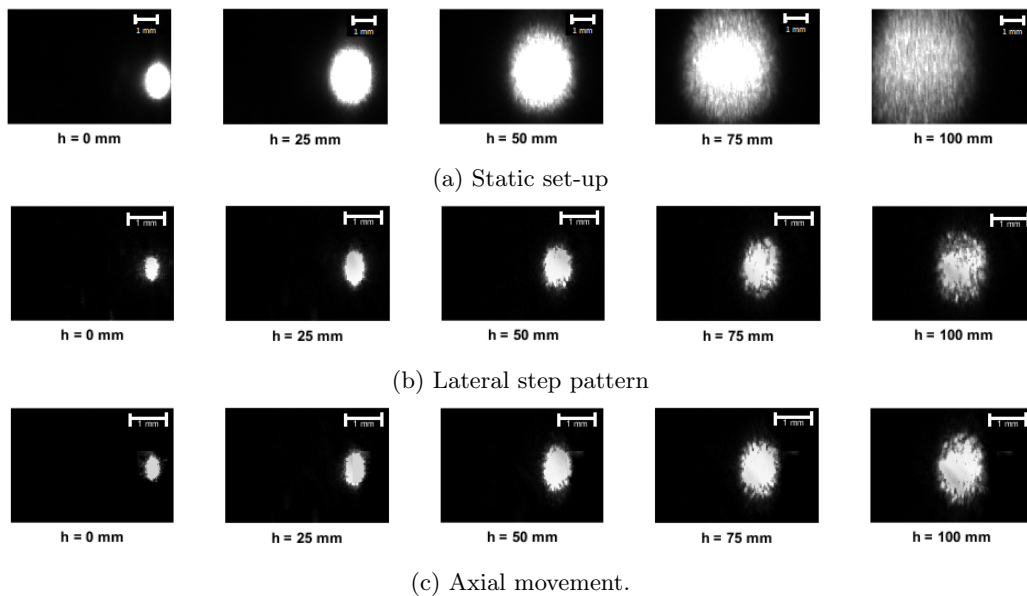


Figure 6.20: Images taken at certain displacements during the different calibration experiments. Note: background noise in these images has been suppressed during processing.

Accuracy of system during LMD

The previous discussion has been focussed on the accuracy in "ideal" conditions i.e. without the high power processing laser beam, but a question that must be answered is: what is the additional influence of the actual LMD process, thus including the interference caused by the high power process laser beam, metal powder and melt pool. As mentioned before, a set of experiments was performed, that step-by-step added these additional factors. The results are shown in figure 6.21 and in table 6.5.

This figure clearly shows that turning on the metal powder feed, has little influence on the accuracy of the measurements. But when the measurement is performed on a bead of molten metal the fluctuation in the measurements increase sharply. It can be observed in figure 6.22b that there are more reflections present, and while a large portion of these reflections will be suppressed by the applied threshold, it will be enough to reduce the accuracy of the sensor.

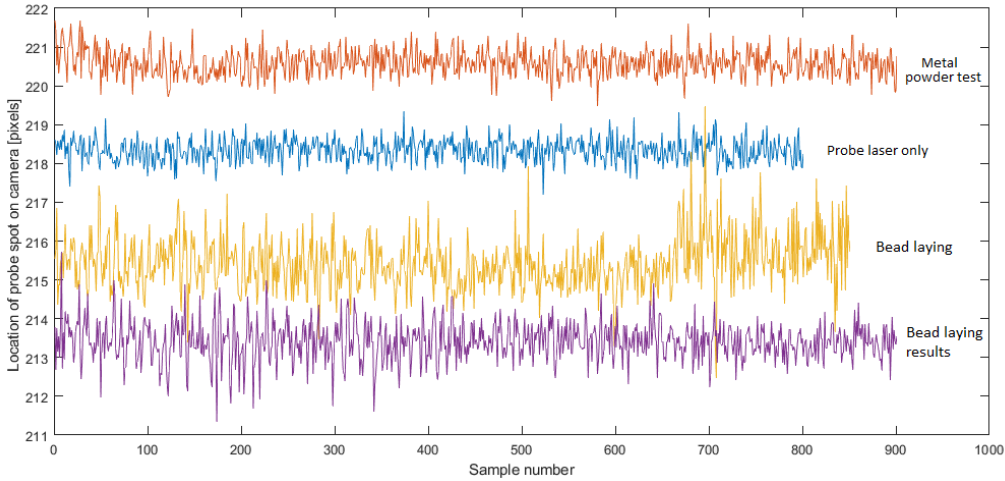


Figure 6.21: Sensor results from 4 different runs according to table 6.3.

The last set of measurements was gathered by moving the probe laser beam over the already deposited bead (so after LMD), to examine the result. It can be seen in the resulting data, that the fluctuations are still relatively high when compared to the earlier laser probe-only measurement. However when examining figure 6.22c, which is a representative image taken during the measurements, it can be seen that there are two horizontal "tracks" present in the image, which will introduce inaccuracies in the image processing. These tracks and other bright spots are caused by the rough clad surface at the sides due to partly un-molten powder particles. Furthermore these tracks indicate that the diameter of the spot of the probe laser, is too large for this melt pool size. Thus overall, these aspects have increased the interference in the processing, and thus the accuracy will decrease.

An attempt was made to reduce the effects of the tracks after and during bead depositing by further cropping the image to only the centreline of the projected spot (17 by 30 (hxb) pixels). This indeed has the effect of improving the fitting accuracy by 10% (examination) to 30% (during depositing) by removing the additional sources of noise.

Table 6.5: Experimental results during LMD process, with $D_{dia} = 6$ mm.

Experiment	Mean value	Fitting accuracy (2σ) [pixels]	Accuracy (2σ) [mm]
Probe laser only	218.3	± 0.59	± 0.40
Metal powder test	220.6	± 0.67	± 0.46
Bead laying	215.4	± 1.40	± 0.84
Bead laying results	213.4	± 1.00	± 0.70

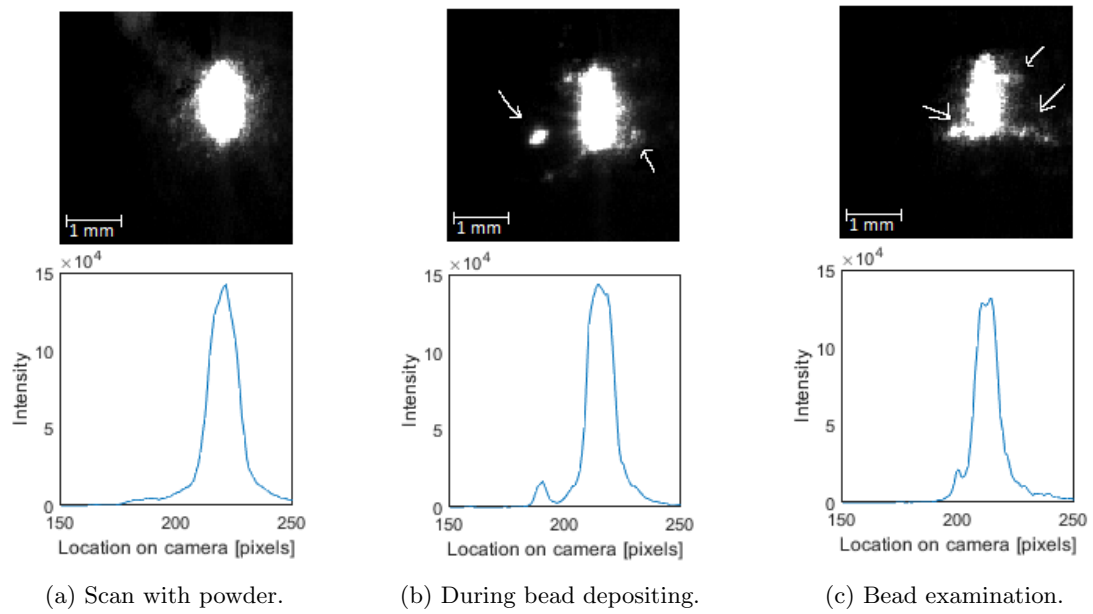


Figure 6.22: Images taken halfway through bead depositing, shown together with intensity profile and annotations, with $D_{dia} = 6$ mm. Cropped to a size of 100 by 100 pixels.

6.4 Additional processing of sensor output

In the previous sections, the image processing has carried out according to the diagram shown in figure 5.5 in chapter 6, with the early image processing consisting out of isolating the area of interest, and a background subtraction. However as shown in figure 6.17, the overall accuracy of the system does not meet the stated requirements. In the article by Donadello et al [15], they made use of a moving average filter on the output of the sensor (location of the centroid). Thus in this section several methods of further image processing will be examined, and their influence on the accuracy of the sensor determined.

The first method to be examined, is the addition of a moving average filter to the sensor output. Using the measurements taken during the axial movement experiments on the dynamic set-up, the direct impact on the resulting signal is shown in figure 6.23. The overall effect of this filter on the accuracy can be found in figure 6.24. It is shown in these figures, that using a moving average filter will improve the accuracy of the sensor output by a significant amount.

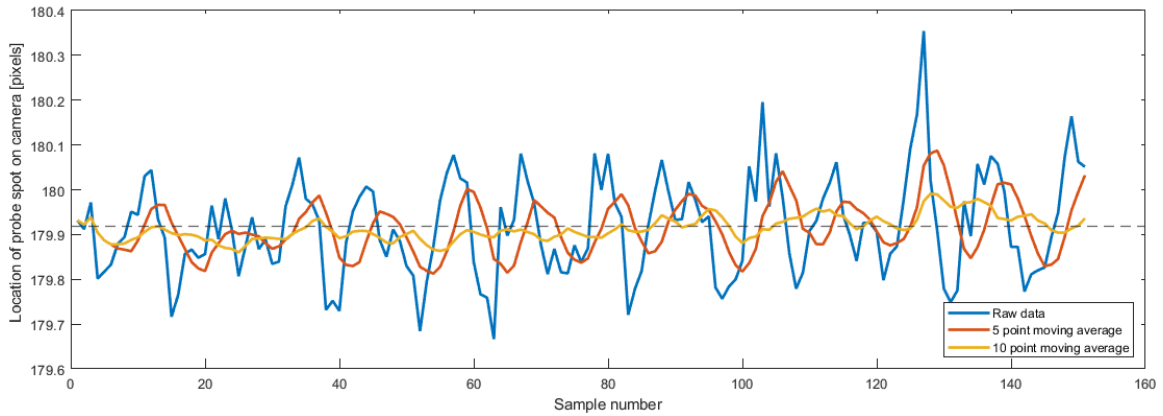
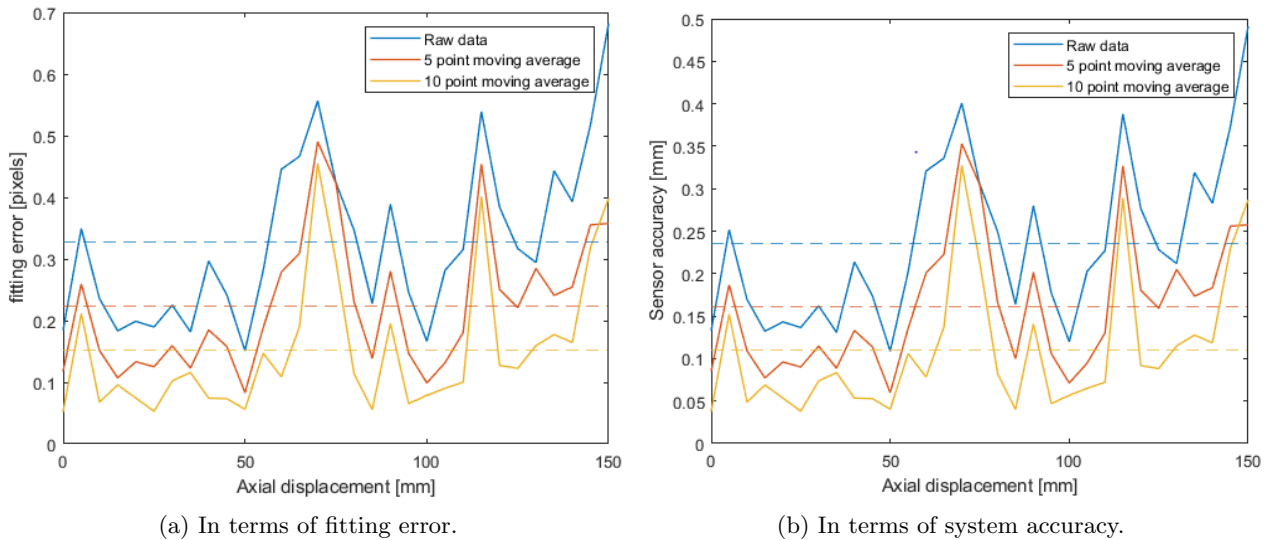


Figure 6.23: Sensor results using a moving mean at $h = 50$ mm.

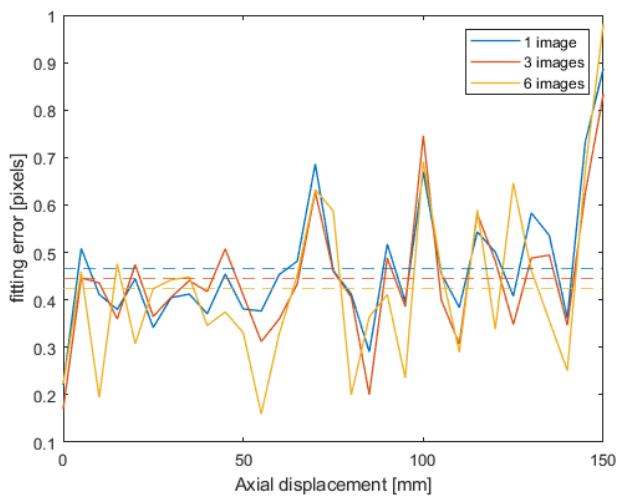


(a) In terms of fitting error.

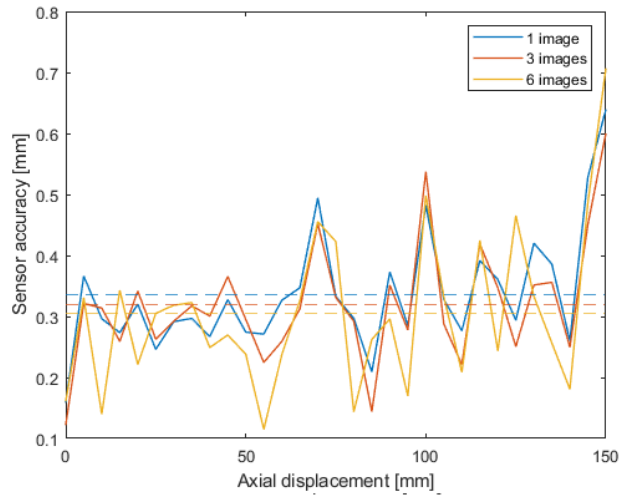
(b) In terms of system accuracy.

Figure 6.24: Fitting error and system accuracy when implementing a moving average filter on data gathered with diaphragm diameter of $D_{dia} = 6$ mm. Dotted horizontal lines show the data mean.

In section 6.3.2 it was demonstrated that the error in the fit is caused by small perturbations in the image taken by the camera over time. As such, if multiple images are combined, this error could be reduced. Since the camera images were taken at 90 FPS, and the stated requirement is 30 FPS, it will be possible to combine multiple images into one, and still meet the requirements. The results of this is shown in figure 6.25. As can be observed from this figure, there is a small but noticeable improvement in the accuracy if more images are combined.



(a) In terms of fitting error.



(b) In terms of system accuracy.

Figure 6.25: Fitting error and system accuracy on measurement obtained with $D_{dia} = 6$ mm when summing several consecutive images. Dotted line shows the data mean.

6.5 Practical applications

As mentioned in section 6.2 to investigate the practical long-term aspects of the sensor behaviour, a wall was "printed" using LMD, by depositing multiple clad tracks on top of each other. The result of this deposition are shown in figure 6.26a and 6.26b, which shows multiple layers deposited on top of each other together with the manually created geometry plot.

The processed results obtained from the CLT sensor over this multi-layer experiment, can be found for a select few layers in figure 6.27. To obtain these results, the complete dataset was split into 50 "layers" and using the known behaviour at the end of each run (acceleration moving backwards, \sim samples 900-1000) the alignment of the results was verified.

Overall when comparing the results obtained using the sensor over time, the bulge at the starting point of the wall, increases in size, while the rest of the measured geometry forms a relatively straight line. Furthermore it can be seen that the results for the fitting accuracy compare very favourably to those obtained previously during the LMD process, with an overall mean of ± 0.76 mm.

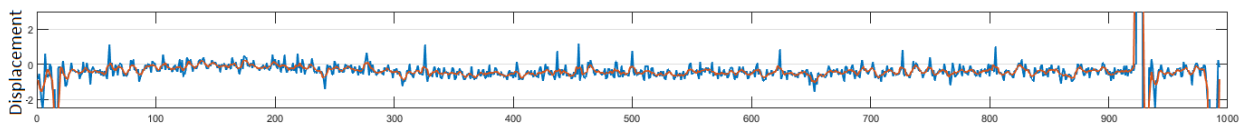


(a) Photo of deposited wall (side view), scale bar of 1 mm.

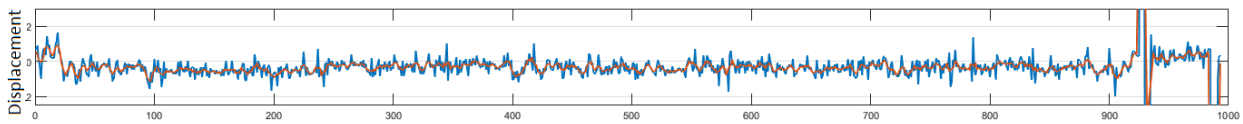


(b) Height of wall, lines are spaced 1 mm apart, arrows denote starting and ending points.

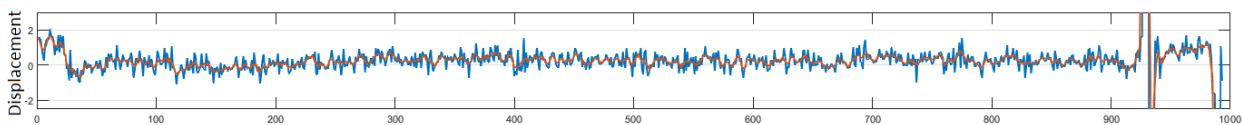
Figure 6.26: Results from depositing 50 layers on top of each other. Deposition moves from left to right.



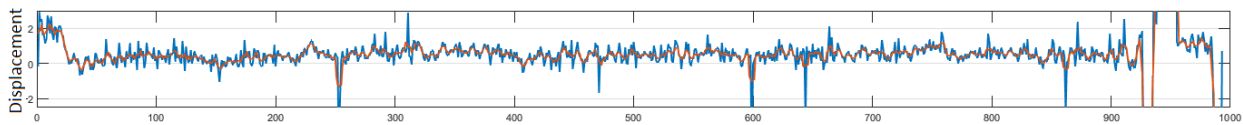
(a) Layer 1, $2\sigma = \pm 0.9$ pixels / ± 0.62 mm



(b) Layer 20, $2\sigma = \pm 1.0$ pixels / ± 0.75 mm



(c) Layer 40, $2\sigma = \pm 1.1$ pixels / ± 0.76 mm



(d) Layer 50, $2\sigma = \pm 1.6$ pixels / ± 1.1 mm

Figure 6.27: Sensor results from measurements taken during deposition, length of each run is 900 samples (100 mm at 10 mm/s and 90 FPS), fitting-accuracy is calculated for samples 100 to 900. Blue line denotes raw sensor output while the red line denotes the 5-point moving average.

6.6 Discussion

As mentioned, one of the primary aspects of the experiments was to get a clear distinction between idealized measurements taken in the static set-up, and practical measurements taken in the dynamic set-up.

In the initial phases where the calibration curves of the static set-up was compared with the results obtained from the SNR model created earlier, in figures 6.9 and 6.10 it showed that the created model correctly simulated the overall behaviour of the system, however as mentioned earlier, there are still some issues with the non-linearities not being properly modelled that have been shown to be present in the system. It is highly probable that these model issues are caused by the simulation of the diaphragm.

One of the primary aspects that became clear, was that the proposed and implemented telescope system showed a small improvement in accuracy with the 2x additional magnification, but it dramatically dropped off in performance at higher magnifications, which was shown in figure 6.16. After some investigation, the cause of this behaviour has been thought to be the decrease in image quality a telescope causes, this was worsened by the "home-brew" nature of the magnifying optics which would have increased the problem.

Another problem present was diagnosed on the dynamic set-up using the 2x telescope configuration. During these early experiments it became clear that there were issues with the measurements taken by the implemented system due to the presence of several problems. As a result of these issues, the revised set-up was implemented to ensure experimental results during LMD where in the correct ballpark.

The decreasing diameter of the diaphragm opening, as in accordance with the model, reduced the overall resolution and accuracy of the system primarily by reducing the displacement of the projected spot and by supposition, decreasing the amount (due to smaller spot) of data present to locate the centroid. Furthermore the image processing was sufficiently capable of removing the internal reflections. As such, a larger diaphragm size was preferable. An additional problem that was seen with decreasing the diaphragm, was that when its diameter became smaller than 6 mm, the amount of "flashed" observed increased, which would reduce the overall accuracy.

Another point that can be discussed, is the accuracy of the system during actual laser metal deposition. In table 6.5 and figure 6.22 those results were shown for a single clad bead. However when multiple beads were deposited on top of each other, the results show large differences in the fitting accuracy between different layers, while the mean remains the same (± 0.76 mm), with the results obtained in the single run being around the average of the multi-layer runs.

But this leads into the fact that the accuracy obtained during LMD is much lower than that obtained during "ideal" conditions (± 0.19 mm in static ideal conditions, and ± 0.37 mm in dynamic ideal conditions). This sharp reduction in accuracy is caused by the presence of further unwanted reflections not suppressed by the static background subtraction and caused by the scattering of the probe laser. Which is most easily illustrated in figure 6.22. This shows that the implemented design for the image processing is insufficient and will required another processing step that can deal with those additional reflections.

Chapter 7

Conclusion and recommendations

7.1 Conclusion

The main goal of this research was to investigate and implement, a sensor to measure the axial displacement of the clad bead deposited during a powder based LMD process. Initial investigation studied several sensors that were available to be implemented. However, due to cost and an additional desire for omni-direction movement, the choice was made to implement the currently experimental coaxial laser triangulation method.

To implement this method on the existing set-up, multiple models were created based on the geometry, optical properties and, ray-tracing, to derive the design variables required to implement the CLT method. To meet the resolution requirements, it was chosen to implement a telescope into the optical system to improve the magnification. However, the main conclusion that can be drawn from the experimental results, is that while the design shows indeed increased axial resolution, that has been countermanded by a significantly decreased overall accuracy. The primary cause of this failure is the fact that the implemented telescope degrades the image reaching the camera to such a degree, that the improved axial resolution is counterbalanced by a significant reduction in the overall accuracy of the image processing.

A later set of experiments, that were performed using a revised version of the implementation, without any magnification and with improved rigidity, showed significantly improved results in both idealized circumstances and during LMD depositing. However it could be seen that during LMD additional sources of noise present in the image, sharply decreasing the accuracy of the system. These additional sources were caused by the scattering of the probe laser on the (rough) surface of the bead and the substrate which is only partially caught by the image processing.

However another conclusion that can be drawn was that the models created to model the system behaviour, returned relatively valid results, with the exception being that the behaviour of the diaphragm diverged from the model.

The main conclusion that can thus be drawn, is that coaxial laser triangulation is a relatively simple and cheap method, that can be used to currently reach ± 0.2 mm (in ideal conditions) or ± 0.76 mm (during LMD with additional noise) of accuracy. It has further been shown that the accuracy in ideal conditions can be significantly improved to ± 0.12 mm by using a moving average filter on the sensor output. Furthermore, another 15-20% could be obtained by improving the pre- and post-processing of the images obtained by the camera.

Significant improvements could be done with a redesign, that improves the magnification and thus the axial resolution of the system, that improves the rigidity of the optical tubing and a more advanced image feature recognition algorithm.

7.2 Recommendations

The experimental results showed promise in the basic function of the sensor system, but it was noted that a redesign was required to meet the originally proposed specification.

One of the main problems that was encountered during the experiments on the dynamic set-up described in section 6.2.2, was that the optical system was of insufficient rigidity. The main recommendation to combat this lack of rigidity is to replace the compression fitting near the top-cover (figure 7.1) with a more robust connection, preferably a bolted connection as used in the adapters. Furthermore it is recommended to replace the modular SM1 threaded aluminium components with dedicated turned components that are bolted together.



Figure 7.1: The compression fit linking the processing head and the optics.

Another problem that has been noted was that the laser source used for the probe laser beam was of relatively low quality and used a very simplistic spatial filter to become circular in shape. It is recommended to either change the design to "properly" circularize the laser spot (as described in Thorlabs' documentation [43]), or as will be noted later, to replace it completely with a laser source combined with a transport fibre into a collimator.

The other main problem, as has been noted several times before, is that the axial resolution of the measurement system is not enough to meet the specifications, and that the attempt to improve this via the implementation of a Galilean telescope failed. Thus other solutions to increase the resolution must be considered. The first part of a solution is to replace the low-resolution camera (thus large pixel sizes) used in the experiments with a higher resolution camera, a short investigation yielded numerous possibilities compatible with the current set-up, that would improve the resolution with a factor two (i.e. 1.2MP instead of the current 0.3).

Another part of the solution is to increase the offset b_k of the triangulation set-up. In the current implementation this was limited to 9 mm since it was limited by the optical tubing (22 mm inner diameter). However it would be recommended to change the overall configuration of the system by moving the insertion point of the probe-laser beam from perpendicular via the beam-splitter, to parallel by mounting it directly on the modular top-cover of the optical head as shown in figure 7.2. This can be achieved by mounting the laser indirectly via the use of the aforementioned transport fibre. This will allow for a much larger baseline (up to 30-35 mm for the current Trumpf D70 optic), resulting in a significantly higher axial resolution. This will also eliminate some internal reflections since all direct reflections on optical components will be directly out of the optical path of the camera.

The third part of the recommended solution is to increase the magnification of the optical system by increasing the focal length of the camera lens. Earlier in this report this option was discarded due to the significant increase in length of the optical system (figure 4.3), However due to the failure of increasing the magnification by telescope, described in this report, this possible solution would require additional investigation, by for example investigating if the overall length can be reduced by "folding" the system using mirrors, which could result in a much shorter and thus stiffer system. An overview of this design is shown in figure 7.3.

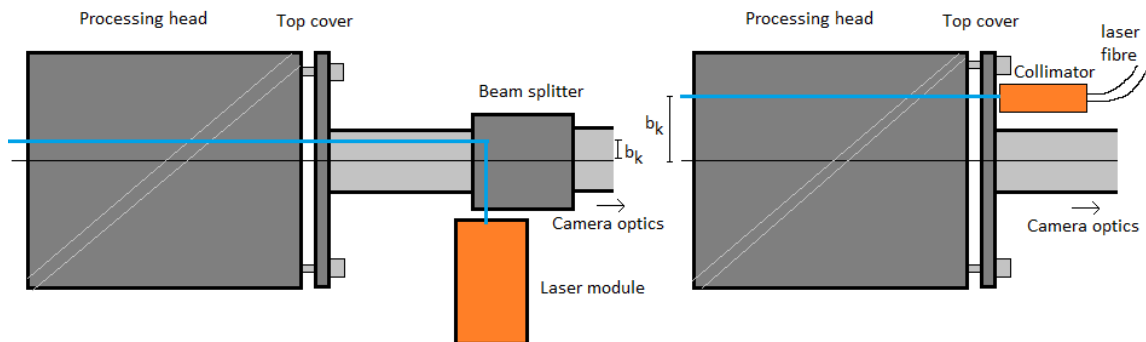


Figure 7.2: Current layout(left) and proposed alternative (right) of the laser module.

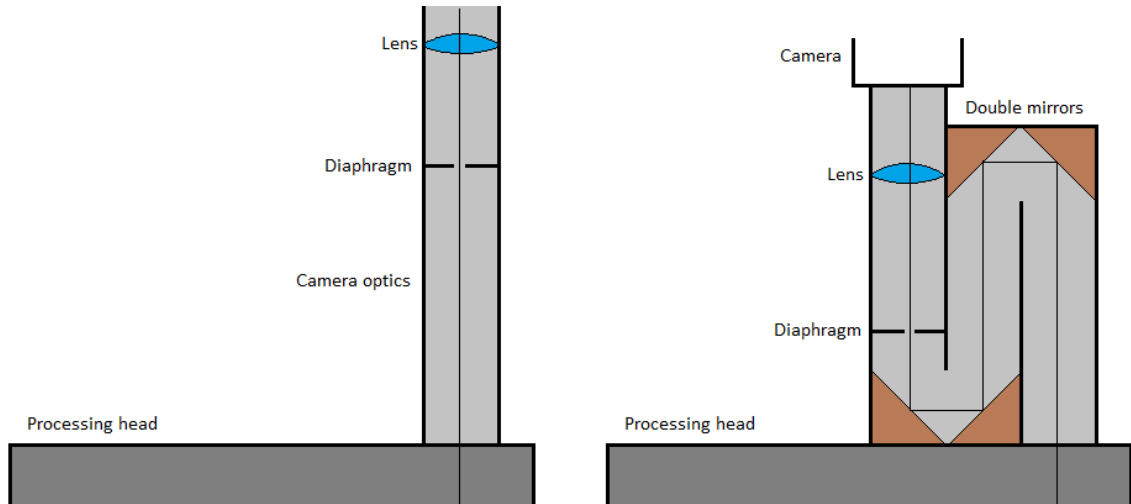


Figure 7.3: Current layout(left) and proposed "folded" alternative (right) of the optical tubing.

The last recommendation, is a more thorough investigation into locating the centre of the projected probe spot using different methods of filtering and curve fitting. Since the method utilized in this report was based on the method described in the original research [15] with background subtraction and cropping used to remove static internal reflections and with Gaussian curve fitting using Guo's algorithm [42]. Furthermore while most of the internal reflections are removed via the applied background subtraction, other more dynamic reflections, are still present and significantly reduce the accuracy. Thus another step will need to be added to the image processing, or another variant must be developed using direct feature recognition to locate the projected image.

Bibliography

- [1] S. M. Thompson, L. Bian, N. Shamsaei, and A. Yadollahi, “An overview of direct laser deposition for additive manufacturing; part i: Transport phenomena, modeling and diagnostics,” *Additive Manufacturing*, vol. 8, pp. 36 – 62, 2015.
- [2] B. Graf, S. Ammer, A. Gumenyuk, and M. Rethmeier, “Design of experiments for laser metal deposition in maintenance, repair and overhaul applications,” *Procedia CIRP*, vol. 11, pp. 245–248, 12 2013.
- [3] I. Harter, “Method of forming structures wholly of fusion deposited weld metal,” *Patent# US A*, vol. 2299747, 1942.
- [4] N. Shamsaei, A. Yadollahi, L. Bian, and S. M. Thompson, “An overview of direct laser deposition for additive manufacturing; part ii: Mechanical behavior, process parameter optimization and control,” *Additive Manufacturing*, vol. 8, pp. 12 – 35, 2015.
- [5] Fei Xing, Weijun Liu, and Tianran Wang, “Real-time sensing and control of metal powder laser forming,” in *2006 6th World Congress on Intelligent Control and Automation*, vol. 2, pp. 6661–6665, 2006.
- [6] A. Heralić, A.-K. Christiansson, M. Ottosson, and B. Lennartson, “Increased stability in laser metal wire deposition through feedback from optical measurements,” *Optics and Lasers in Engineering*, vol. 48, no. 4, pp. 478 – 485, 2010.
- [7] S. Takushima, D. Morita, N. Shinohara, H. Kawano, Y. Mizutani, and Y. Takaya, “Optical in-process height measurement system for process control of laser metal-wire deposition,” *Precision Engineering*, vol. 62, pp. 23 – 29, 2020.
- [8] D. Tyralla, H. Köhler, T. Seefeld, C. Thomy, and R. Narita, “A multi-parameter control of track geometry and melt pool size for laser metal deposition,” *Procedia CIRP*, vol. 94, pp. 430 – 435, 2020. 11th CIRP Conference on Photonic Technologies [LANE 2020].
- [9] A. Heralić, A.-K. Christiansson, and B. Lennartson, “Height control of laser metal-wire deposition based on iterative learning control and 3d scanning,” *Optics and Lasers in Engineering*, vol. 50, no. 9, pp. 1230 – 1241, 2012.
- [10] “Omc technical brief - single point optical triangulation.” https://www.optical-metrology-centre.com/Downloads/Tech_Briefs/TechBrief_SinglePtOpticalTriangulation.pdf. [Online, accessed 21-12-2020].
- [11] G. Römer, “Seam tracking for laser welding with an industrial robot,” in *Proceedings 3rd Workshop on European Scientific and Industrial Collaboration* (J. van Amerongen, J. Jonker, J. Jonker, P. Regtien, and P. Regtien, eds.), pp. 477–486, Drexel Institute for Mechatronics, 6 2001.
- [12] D. Iakovou, *Sensor development and integration for robotized laser welding*. PhD thesis, University of Twente, Netherlands, 2 2009.
- [13] I. Garmendia, J. Leunda, J. Pujana, and A. Lamikiz, “In-process height control during laser metal deposition based on structured light 3d scanning,” *Procedia CIRP*, vol. 68, pp. 375 – 380, 2018. 19th CIRP Conference on Electro Physical and Chemical Machining, 23-27 April 2017, Bilbao, Spain.
- [14] I. Garmendia, J. Pujana, A. Lamikiz, M. Madarieta, and J. Leunda, “Structured light-based height control for laser metal deposition,” *Journal of Manufacturing Processes*, vol. 42, pp. 20 – 27, 2019.

- [15] S. Donadello, M. Motta, A. G. Demir, and B. Previtali, “Coaxial laser triangulation for height monitoring in laser metal deposition,” *Procedia CIRP*, vol. 74, pp. 144 – 148, 2018. 10th CIRP Conference on Photonic Technologies [LANE 2018].
- [16] S. Donadello, M. Motta, A. G. Demir, and B. Previtali, “Monitoring of laser metal deposition height by means of coaxial laser triangulation,” *Optics and Lasers in Engineering*, vol. 112, pp. 136 – 144, 2019.
- [17] J. Mazumder, D. Dutta, N. Kikuchi, and A. Ghosh, “Closed loop direct metal deposition: art to part,” *Optics and Lasers in Engineering*, vol. 34, no. 4, pp. 397 – 414, 2000. Laser Material Processing.
- [18] J. Mazumder, J. Choi, and A. Schifferer, “Direct materials deposition: Designed macro and microstructure,” *Material Research Innovations*, vol. 3, 10 1999.
- [19] M. Asselin, E. Toyserkani, M. Irvani-Tabrizipour, and A. Khajepour, “Development of trinocular ccd-based optical detector for real-time monitoring of laser cladding,” in *IEEE International Conference Mechatronics and Automation, 2005*, vol. 3, pp. 1190–1196 Vol. 3, 2005.
- [20] M. Irvani-Tabrizipour and E. Toyserkani, “An image-based feature tracking algorithm for real-time measurement of clad height,” *Mach. Vis. Appl.*, vol. 18, pp. 343–354, 11 2007.
- [21] E. Toyserkani and A. Khajepour, “A mechatronics approach to laser powder deposition process,” *Mechatronics*, vol. 16, no. 10, pp. 631 – 641, 2006.
- [22] M. Kogel-Hollachera, M. Schoenleberb, and T. Bautzea, “Inline coherent imaging of laser processing-a new sensor approach heading for industrial applications,” 2014.
- [23] M. Kogel-Hollacher, S. André, and T. Beck, “New horizons in laser material processing: how OCT sets new standards,” in *High-Power Laser Materials Processing: Applications, Diagnostics, and Systems VIII* (S. Kaierle and S. W. Heinemann, eds.), vol. 10911, pp. 81 – 91, International Society for Optics and Photonics, SPIE, 2019.
- [24] M. Kogel-Hollacher, “Laser welding using oct imaging.” <https://www.industrial-lasers.com/welding/article/14036845/laser-welding-using-oct-imaging>, Jul 2019. [Online, accessed 3-6-2020].
- [25] K.-Y. Bae and J.-H. Park, “A study on development of inductive sensor for automatic weld seam tracking,” *Journal of Materials Processing Technology*, vol. 176, no. 1, pp. 111 – 116, 2006.
- [26] “Detection based on ”changes in eddy current” what is an inductive displacement sensor?.” https://www.keyence.eu/ss/products/sensor/sensorbasics/eddy_current/. [Online, accessed 3-9-2020].
- [27] “Ultra-fast distance measurements of almost all materials.” <https://www.precitec.com/optical-3d-metrology/technology/chromatic-confocal-sensors/>. [Online, accessed 10-2-2021].
- [28] Matthieu Desjacques, “Chromatic confocal sensors for non-destructive measurement and inspection in nanometric scales.” <https://www.sentech.nl/app/uploads/2018/11/181105-sentech-presentation-precision-fair-chromatic-confocal-stil-room20-DEF-PDF-KL.pdf>. [Online, accessed 3-10-2020].
- [29] L. Song, V. Bagavath-Singh, B. Dutta, and J. Mazumder, “Control of melt pool temperature and deposition height during direct metal deposition process,” *The International Journal of Advanced Manufacturing Technology*, vol. 58, pp. 247–256, 01 2012.
- [30] “Programmeerbare focuseeroptieken.” https://www.trumpf.com/nl_NL/producten/laser/bewerkingsoptieken/programmeerbare-focuseeroptieken/. [Online, accessed 20-7-2020].
- [31] P. GmbH, “Welding depth measurement laser welding: Precitec.” <https://www.precitec.com/laser-welding/products/process-monitoring/precitec-idm/>. [Online, accessed 13-5-2020].
- [32] L. L. GmbH, “Optical coherence tomography for laser welding.” <http://www.lessmueller.de/en/products/oct>. [Online, accessed 16-5-2020].
- [33] Lessmüller Lasertechnik, *Sensing and quality monitoring with OCT*, 2019.
- [34] M. de Graaf, *Sensor-guided robotic laser welding*. PhD thesis, University of Twente, Netherlands, 12 2007.
- [35] Baumer GmbH, *Baumer TXG User’s Guide for Gigabit Ethernet Cameras*, 2009.
- [36] A. van der Meer, “Design & implementation of a setup for the validation of a model predicting the temperature cycle and residual stresses in laser cladding,” *University of Twente*, 2018.

- [37] W. Smith, *Modern Optical Engineering: The Design of Optical Systems*. Optical Engineering Series, McGraw Hill, 2000.
- [38] “Fb500-10 Ø1” bandpass filter, $cwl = 500 \pm 2$ nm, $fwhm = 10 \pm 2$ nm.” <https://www.thorlabs.com/thorproduct.cfm?partnumber=FB500-10>. [Online, accessed 20-8-2020].
- [39] M. L. Griffith, M. E. Schlienger, and L. D. Harwell, “Thermal behavior in the lens process,” 8 1998.
- [40] “2w 450nm blue switchable ttl/analogue laser module, adjustable focus 12v (cnc engraving).” https://odicforce.com/epages/05c54fb6-7778-4d36-adc0-0098b2af7c4e.sf/en_GB/?ObjectPath=/Shops/05c54fb6-7778-4d36-adc0-0098b2af7c4e/Products/OFL419-2-TTL-ANA. [Online, accessed 29-12-2020].
- [41] Sbyrnes321, “Ray transfer matrix definitions.” <https://upload.wikimedia.org/wikipedia/commons/5/5e/RayTransferMatrixDefinitions.svg>. [Online, accessed 13-2-2021].
- [42] H. Guo, “A simple algorithm for fitting a gaussian function,” *IEEE Signal Processing Magazine*, vol. 28, pp. 134–137, 09 2011.
- [43] “Comparison of circularization techniques for elliptical beams.” https://www.thorlabs.com/newgrouppage9.cfm?objectgroup_id=11426. [Online, accessed 29-10-2020].
- [44] “M-404 precision linear stage.” <https://www.physikinstrumente.com/en/products/linear-stages/stages-with-stepper-dc-brushless-dc-bldc-motors/m-404-precision-translation-stage-701751/>. [Online, accessed 14-12-2020].
- [45] Ocean Optics, *HR4000 Spectrometer*, 2016.
- [46] Ocean Optics, *Ocean Optics Light sources catalogue*, 2016.
- [47] “Thorlabs’ threading specifications.” https://www.thorlabs.com/newgrouppage9.cfm?objectgroup_id=1524. [Online, accessed 30-12-2020].
- [48] “3-element collimating glass lens assembly coated for 445-450nm lasers.” https://odicforce.com/epages/05c54fb6-7778-4d36-adc0-0098b2af7c4e.sf/en_GB/?ObjectPath=/Shops/05c54fb6-7778-4d36-adc0-0098b2af7c4e/Products/OFL163. [Online, accessed 29-10-2020].

Appendix A

Transmission spectra

In section 4.3.1, it was discussed that the transmission spectra of the original optical component had to be determined. Because the optical properties of the TRUMPF BEO D70 optical head were not known, experiments were performed to calculate the transmission ratios of both the dichroic mirror and the camera port that will be used in the experimental setup. To calculate the transmission ratios, equation A.1 can be used. So to determine the transmission spectrum, a light source and a spectrometer are required. The background term in the equation is used. It must be noted that the transmission spectrum reference is the spectrum from the target to the coaxially placed camera. The spectrum from the processing laser to the target, is not further discussed.

$$T(\lambda) = \frac{P_{reference}(\lambda)}{P_{detected\lambda} - P_{background}(\lambda)} \quad (\text{A.1})$$

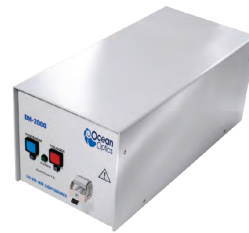
A.1 Experimental set-up

Both the used light-source and the spectrometer were sourced from the UT Microlab and are the OCEAN OPTICS HR4000 (figure A.1a) and the OCEAN OPTICS DH-2000 light source (A.1b). Using this equipment, a setup was built that aligned the glass fibre connected to the light source, with the receiving glass fibre connected to the spectrometer (figure A.2a). In order to measure the desired spectra, the parts were placed between the source and the spectrometer (figures A.2b and A.2c). In the case of the camera port this meant that only the straight (180°) path was measured, Attempts to measure the 90° path failed.

Due to the limitations of the spectrometer, the wavelength range is limited to 200-1100 nm, however because of the range of the monochromatic camera used (400-720 nm), this range is sufficient.



(a) HR4000 spectrometer [45].



(b) DH-2000 UV-VIS-NIR light source [46].

Figure A.1: The equipment used in the experiment

A.2 Results

Using the software supplied with the spectrometer used (SPECTRASUITE) to calculate the transmission spectra, a reference and a dark spectrum needs to be defined in the software. The reference set up was used to define these spectra by first taking a measurement with the source turned on (figure A.3a), and taking a measurement with the source turned off (figure A.3b). It must be noted that in some experiments, very strong peak were detected in the dark spectrum, probably caused by overhead lights turning on.

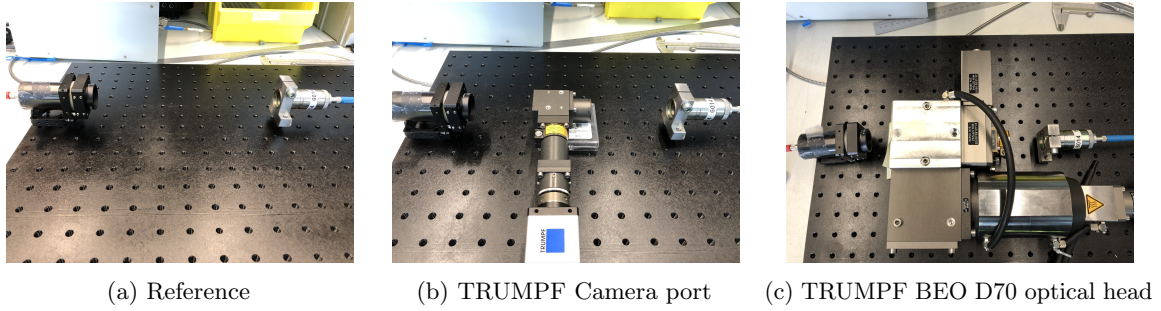


Figure A.2: The equipment used in the experiment

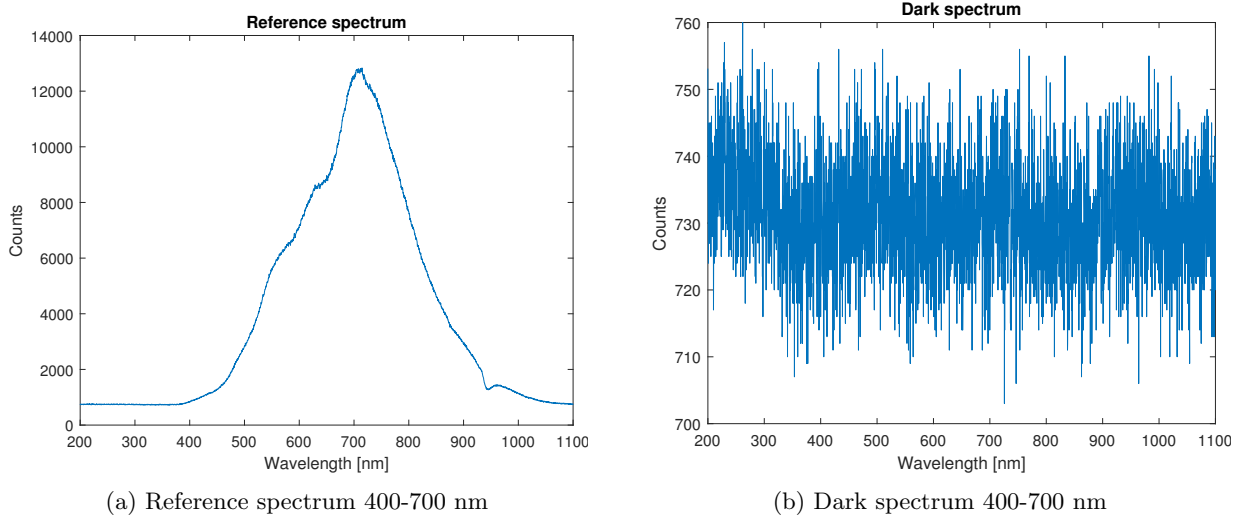


Figure A.3: The spectra used to define the input parameters for the transmission spectra measurements.

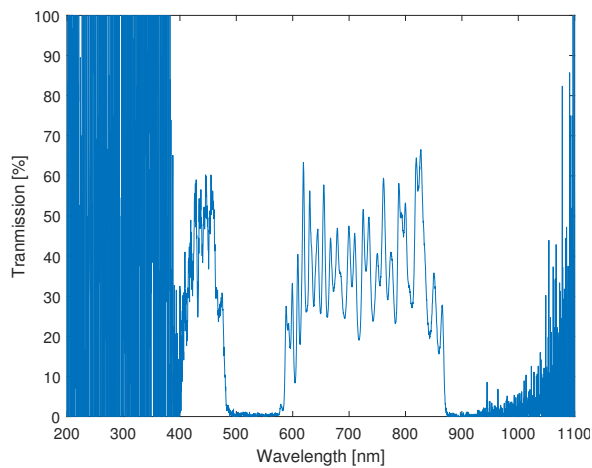
Using this data, the software used could automatically derive the transmission spectra if a optical component was inserted in the path between the source and spectrometer. The initial results are shown in figures A.4a and A.4b. These results show that below 400 nm and above 800 nm, the derived spectrum contains a lot of noise. Furthermore, the spectrum between 400 and 800 nm also shows large variances. To clean up these spectra, the range is limited from 400-800nm, and a gaussian filter is applied to smooth the signal (figures A.4c and A.4d). Multiplying these transmission spectra will yield the transmission spectrum for the combined system for later use (figure A.4e).

In the spectrum of the dichroic mirror (figures A.4a and A.4c it can be seen that multiple areas can be identified:

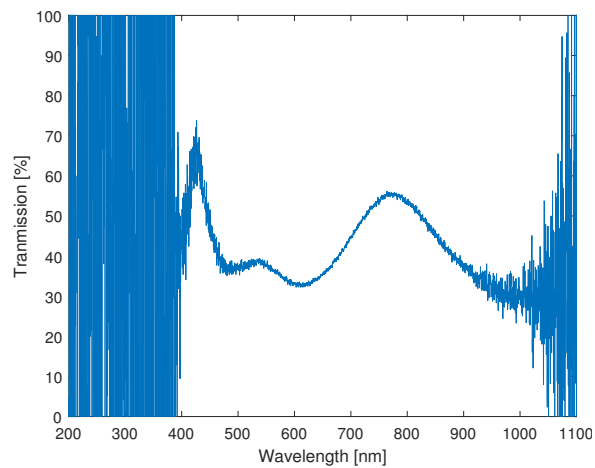
1. 400-500 nm and 600-900 nm: Areas of the spectrum that allow the light to pass through with a TR of around 45%.
2. >400, 500-600 and >900 nm: Wavelength areas that blocks light passing through the mirror.

When looking at the spectrum of the dichroic mirror, it is seen that the mirror blocks light from that main processing laser (1064 nm) from passing through to the coaxial camera. Furthermore, it also blocks the harmonic wavelengths of the processing laser (532 nm for ND:YAG). It must be noted that the transmission ratios themselves, being around 50% are relatively low, when compared to other examples. Another note must be made about the large peaks in the 600-900 nm wavelength window, these peaks are not constant, and will shift on multiple directions if the optical head itself is rotated around its axis. This behaviour indicates that there are rays bouncing around in the dichroic mirror.

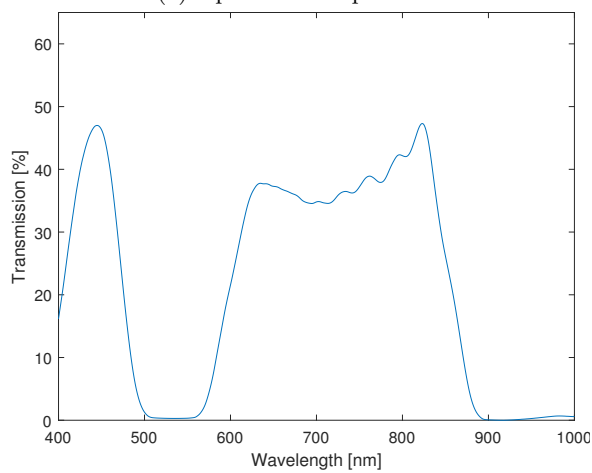
When looking at the spectrum of the camera-port (figures A.4b and A.4d), it is seen that instead of a constant 50-50 distribution, there are various minima and maxima inside the spectrum. These indicate that the camera port is not a perfect beam-splitter, which is understandable given its normal purpose.



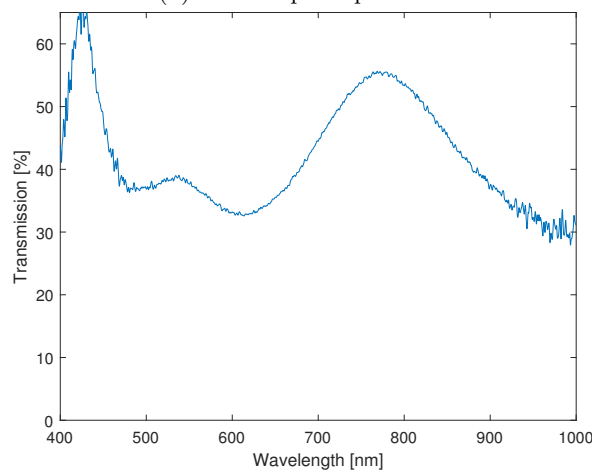
(a) Optical head spectrum



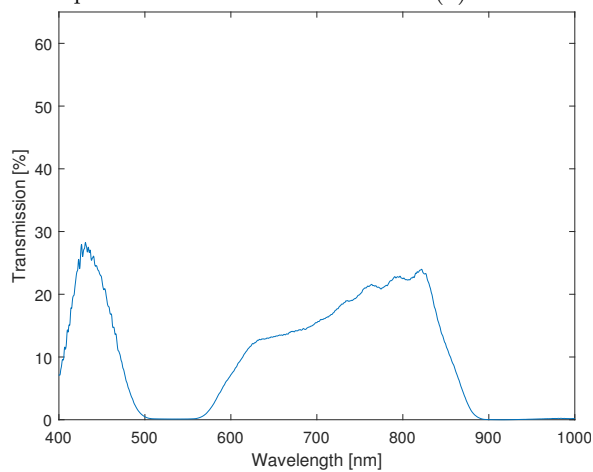
(b) Camera port spectrum



(c) Cleaned optical head spectrum



(d) Cleaned camera port spectrum



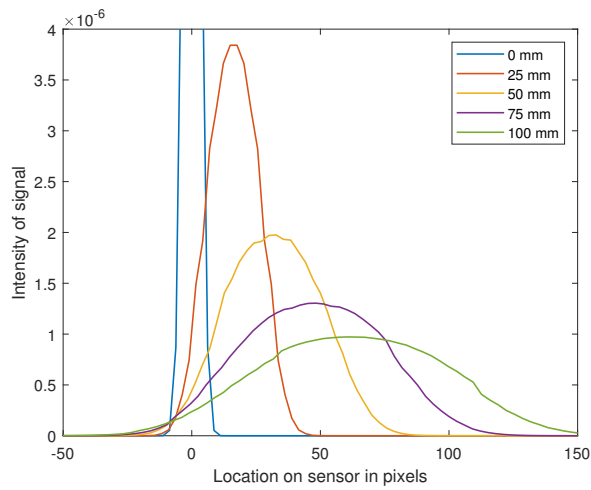
(e) Combined transmission spectra of the optical head and the camera port, from 400-900 nm

Figure A.4: The transmission spectra determined using the defined inputs, together with cleaned up results.

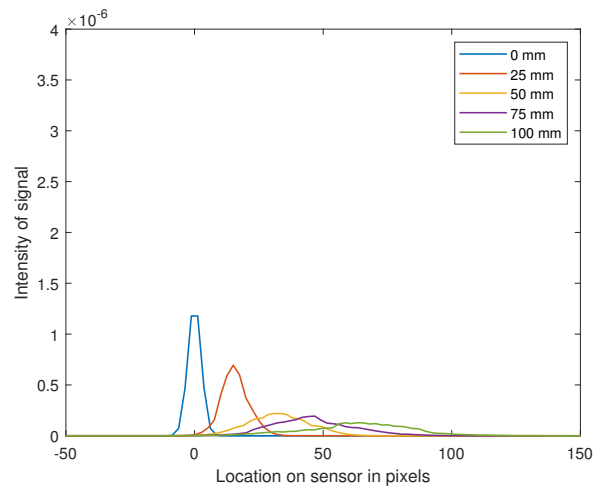
Appendix B

Model results

In this appendix the results from the model with the combined ray tracing and melt pool models can be found that are referred to in section 4.4.4. The configurations modelled are: No magnification (figure B.1), 2x additional magnification (figure B.2) and 3x additional magnification (figure B.3).

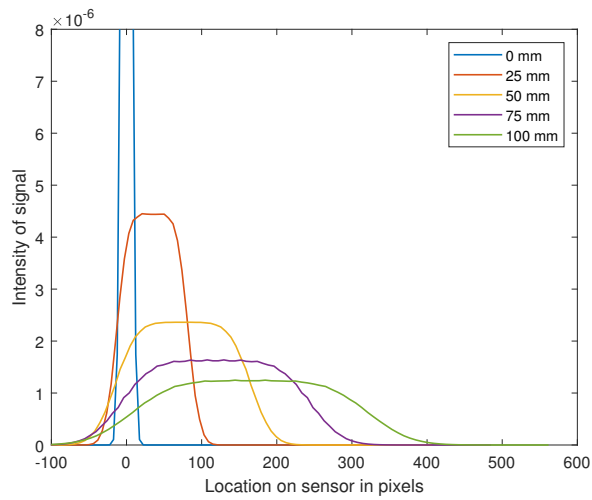


(a) Diaphragm size of 12 mm.

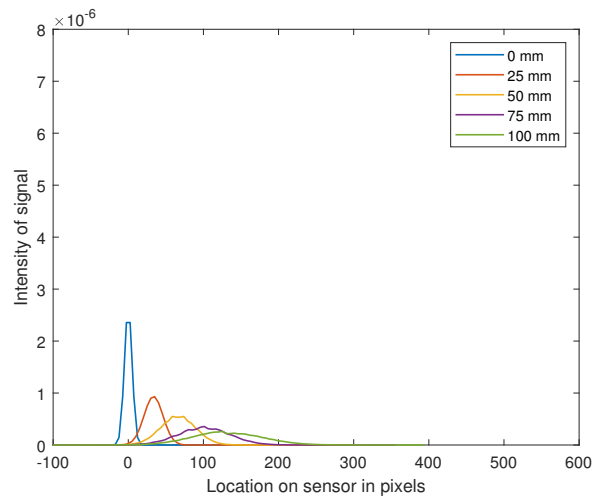


(b) Diaphragm size of 1 mm.

Figure B.1: Intensity profile of the projected image using no additional magnification at differing axial displacements.

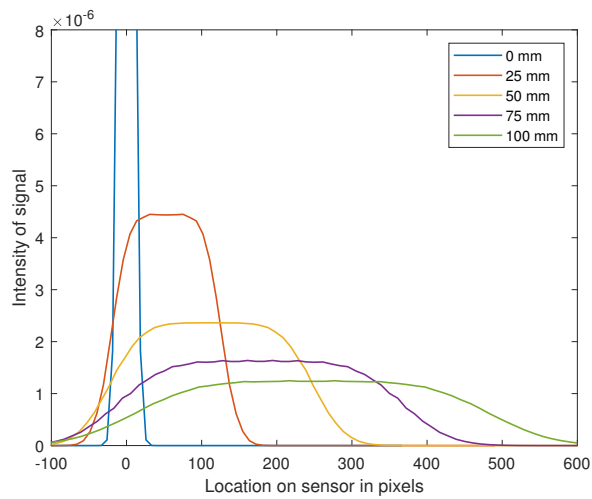


(a) Diaphragm size of 12 mm.

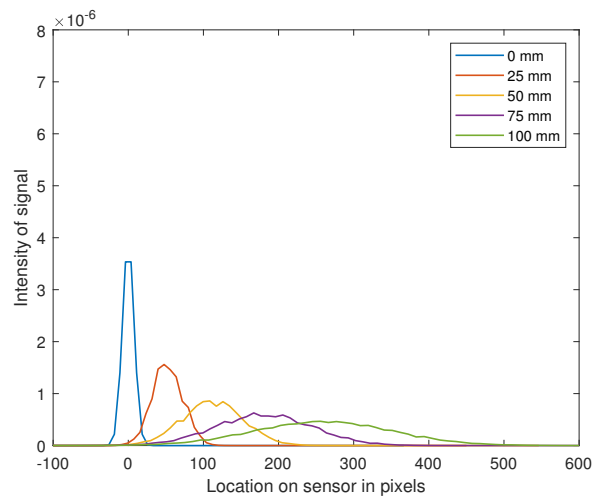


(b) Diaphragm size of 1 mm.

Figure B.2: Intensity profile of the projected image using a 2x additional magnification at differing axial displacements.



(a) Diaphragm size of 12 mm.



(b) Diaphragm size of 1 mm.

Figure B.3: Intensity profile of the projected image using a 3x additional magnification at differing axial displacements.

Appendix C

Technical drawings

In this appendix, the technical drawings of the two adapters that have been created are shown (see section 5.1). Restating their purpose:

- Cameraport-SM1 thread, used to connect the camera port (beam-splitter) to the SM1 optical tubing, used by the telescope
- SM1-Camera, used to connect the SM1 tubing with the original camera optics, furthermore, this adapter is also used to house the bandpass-filter.

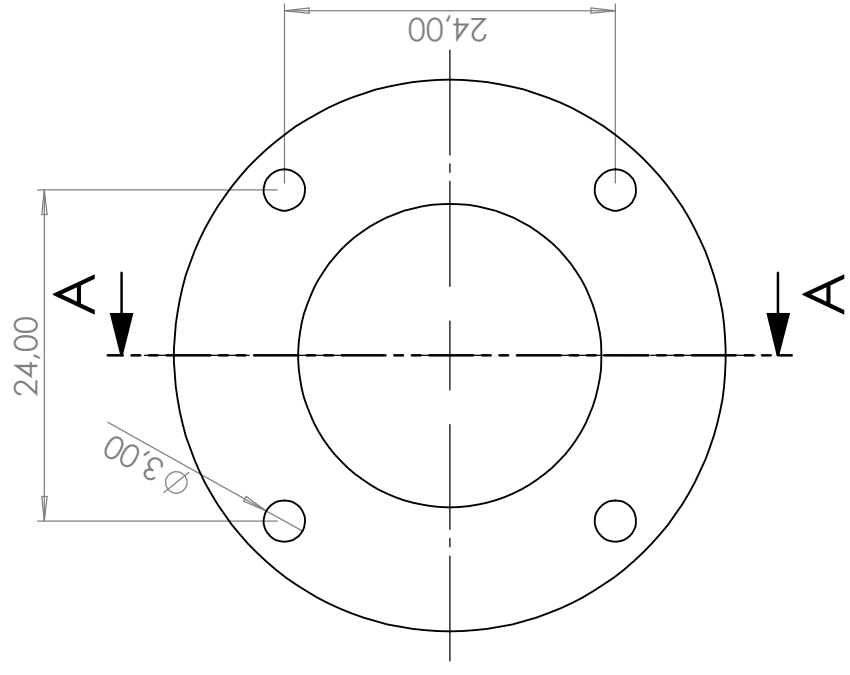
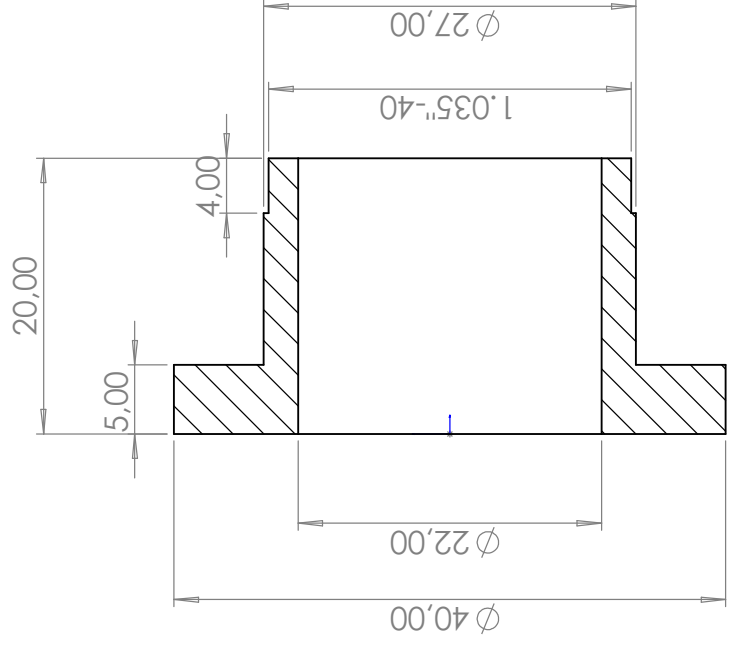
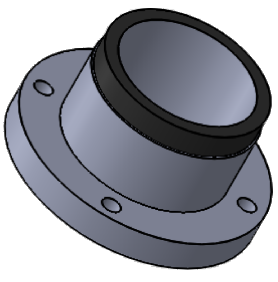
It must be noted that the adapters are largely the same shape, with one having SM1 external thread, and the other SM1 internal thread. Furthermore it must be noted that the second adapter has a deeper bore to accommodate a 1" diameter SM1 compatible Thorlabs filter, which is fixed in place by screwing in the SM1 optical tubing.

Note: these drawings show the SM1 thread as 1.035"-40, these specifications are shown in table C.1.

Table C.1: SM1 threading specifications. Source [47]

SM1 (1.035"-40,0 Threading)					
External Thread, 1.035"-40.0, UNS-2A			Internal Thread, 1.035"-40.0, UNS-2B		
	Inches	mm		Inches	mm
Max Major Diameter	1.0339"	26.261 mm	Min Major Diameter	1.0350"	26.289 mm
Min Major Diameter	1.0288"	26.132 mm	Min Pitch Diameter	1.0188"	25.878 mm
Max Pitch Diameter	1.0177"	25.850 mm	Max Pitch Diameter	1.0234"	25.994 mm
Min Pitch Diameter	1.0142"	25.761 mm	Min Minor Diameter	1.008"	25.603 mm
Max Minor Diameter	1.0068"	25.573 mm	Max Minor Diameter	1.014"	25.756 mm

1 2 3 4 5 6



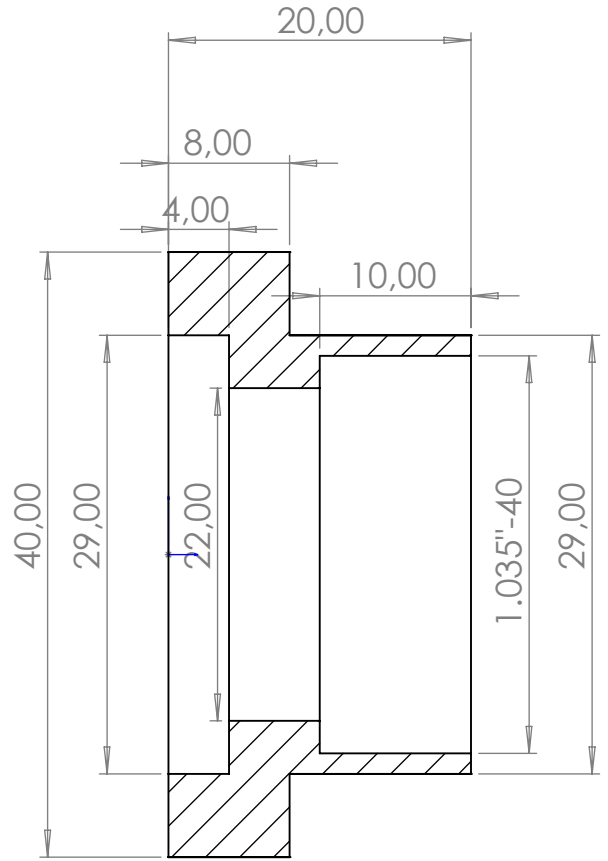
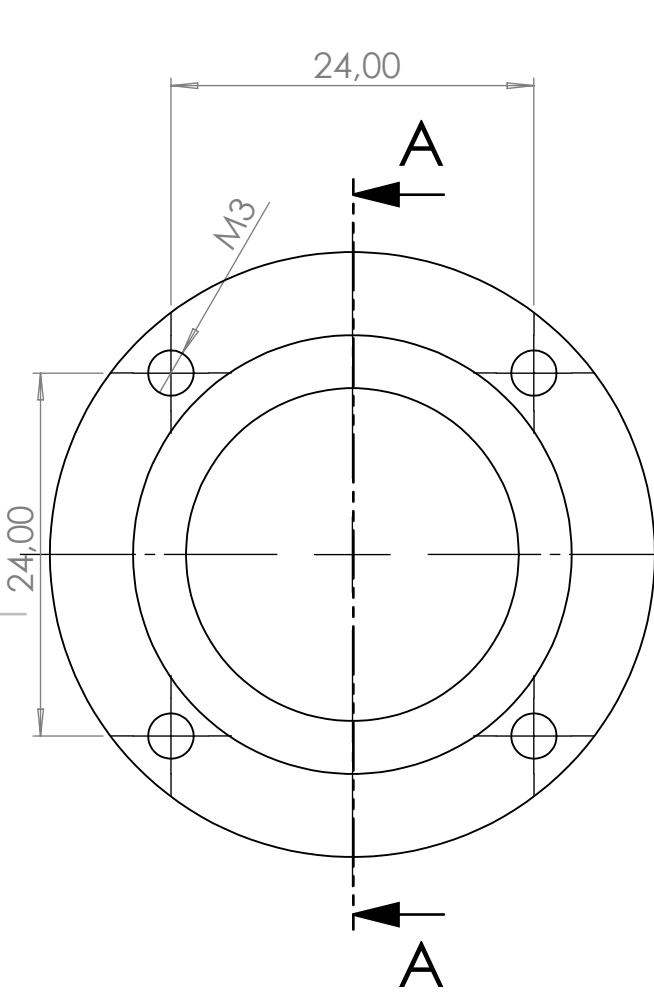
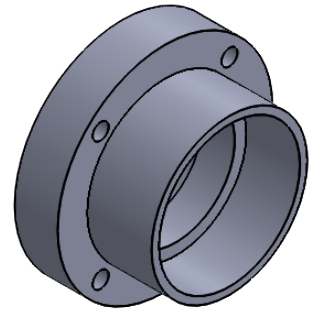
D C B A

D C B A

SECTION A-A

UNLESS OTHERWISE SPECIFIED: DIMENSIONS ARE IN MILLIMETERS SURFACE FINISH: TOLERANCES: LINEAR: ANGULAR:		FINISH:	DEBURR AND BREAK SHARP EDGES		DO NOT SCALE DRAWING	REVISION
DRAWN	NAME	SIGNATURE	DATE	TITLE	Beam splitter to SM1 thread	
CHK'D	Wouter Bos			DWG NO.	1-2	A4
APP'VD				MATERIAL:	Aluminium	
MFG				WEIGHT:		
Q.A				SCALE:2:1		SHEET 1 OF 1

1 2 3 4 5 6



SECTION A-A

UNLESS OTHERWISE SPECIFIED:
DIMENSIONS ARE IN MILLIMETERS
SURFACE FINISH:
TOLERANCES:
LINEAR:
ANGULAR:

FINISH:

DEBURR AND
BREAK SHARP
EDGES

DO NOT SCALE DRAWING

REVISION

DRAWN	NAME	SIGNATURE	DATE				
CHK'D							
APPV'D							
MFG							
Q.A							

TITLE:		lens adapter to SM1	
MATERIAL:	Aluminium	DWG NO.:	1-1
WEIGHT:		SCALE:2:1	SHEET 1 OF 1

A

A

Appendix D

Characterising the laser modules

The lasers that were used in the experimental set-up (see section 5.3.1) came with specifications attached, however due to the little information available and the cheapness of the laser modules themselves, tests were performed to characterise the laser modules.

D.1 Wavelength spectrum

Of course, the first step in evaluating the set-up, is to properly characterise the different components used in the sensor. The first aspect that will be considered, is the wavelength spectrum of the selected 450 nm laser. In the previous chapters, it has been assumed that this spectrum is at exactly 450 nm. Using the same spectrometer used as in appendix A to measure the transmission ratios of the processing optic, the spectrum of the laser modules was measured at 60% power and using a combined 95% neutral density filter to ensure that the measurement sensor was not saturated. The results can be found in figure D.1, this figure shows that the spectrum of the 2 W laser module is centred around 450 nm, while the spectrum of the 4 W module is centred around 453 nm, and saturates the spectrometer. This indicates that both lasers are usable with the 450 nm bandpass-filter.

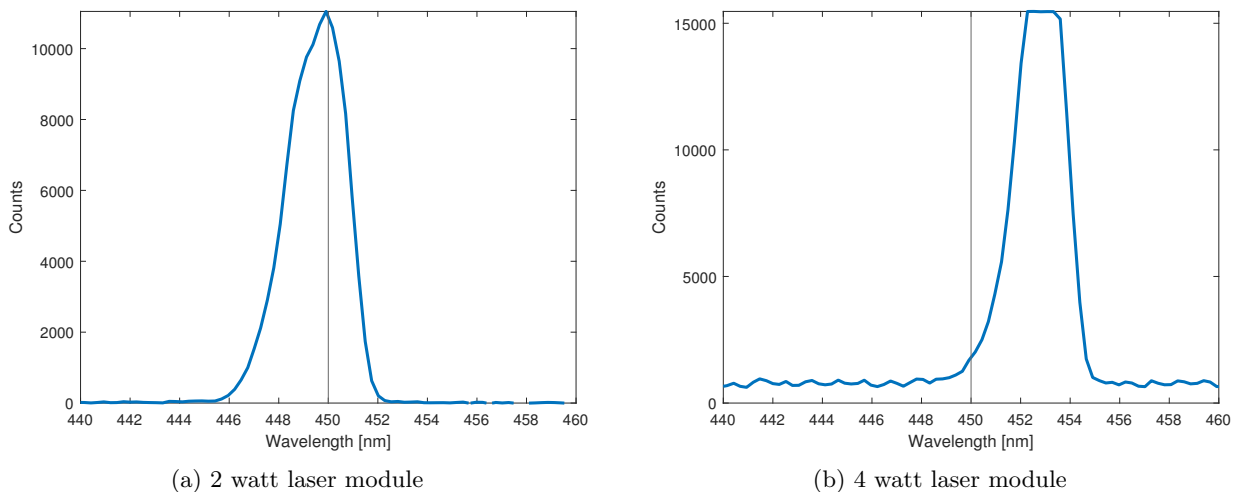


Figure D.1: Captured spectra of the 2 and 4 watt laser modules using the HR4000 spectrometer.

D.2 Beam profile

The next aspect of the laser to consider, is the shape of the laser beam itself. Since the original laser modules used, are meant for CNC engraving, they were supplied with a focussing lens. To ensure a collimated beam, this was replaced with a collimating array consisting out of three lenses (ODICFORCE OFL163 [48]). After replacing the lenses in the modules, it was discovered that the 4-watt laser module did not allow for proper collimation, due to this, and safety concerns regarding the control voltage discussed later, it was dropped from further characterisation.

Using a beam profiler (Primes Micro Spot Monitor) the collimated beam profile was measured at multiple locations, this can be found in figure D.2, it must be noted that the alignment between the profiler and the laser beam axis was slightly off, resulting in a moving image over the 100 mm displacement. In this figure, the laser module emits a beam with a rectangular shape, this is common for a laser diode, as used in the laser module.

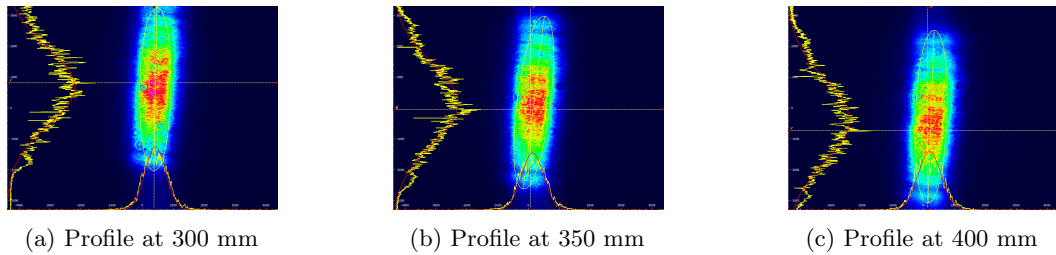


Figure D.2: Beam profiles of the collimated beam captured at several locations.

The main use of the beam-profiler will be to examine the profile of the laser beam when it is emitted from the optical head and is supposed to hit the target. This means that the beam has passed through the beam-splitter and the dichroic mirror and has been focussed by the main processing lens. The results from the beam profiler can be found in figure D.3. These results clearly show that as the axial displacement from the focal point increases, the size of the projected beam also increases. Using the information presented in the figures, the M2 of the probe beam can be calculated. Furthermore, as the shape of the beam suggests, the laser is very much astigmatic and non-Gaussian.

To solve this issue, it is preferable to circularise the laser beam to eliminate the rectangular non-Gaussian aspect, and thus improve the beam quality. The normal way to do this, is via either a cylindrical lens pair, an anamorphic prism pair or a spatial filter (see Thorlabs lab fact [43]). In the current set-up, it was decided to simply use a 2 mm circular cut-out to create a circular beam, the results from the beam profiler can be found in figure D.4.

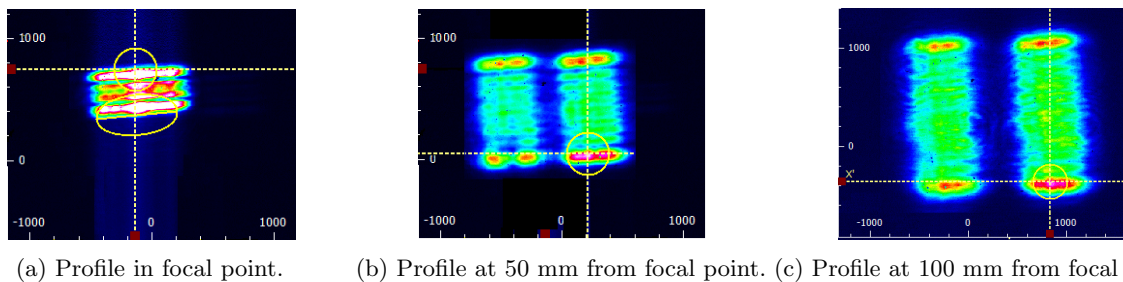
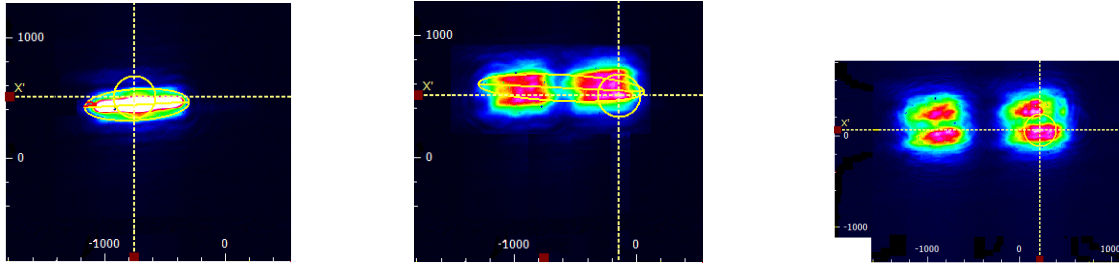


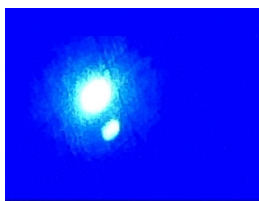
Figure D.3: Beam profiles of the focussed beam out of the processing optic at several location of the focal point. Scales are in μm with $200 \mu\text{m}$ ticks.

Another aspect that is seen in both figures, is that the beam has been split into two parts, which slightly diverge. This has been caused by the fact that the beam-splitter is of a "plate" type, which causes a second reflection when the split beam hits the back of the beam splitter. This results in a second beam being transmitted through the optical system and hitting the target (figure D.5a), furthermore, it is also possible for the beam to 'bounce' inside the plate ensuring even more reflections (figure D.5b).

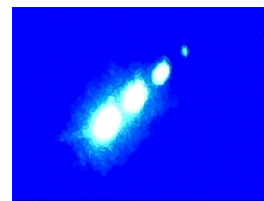


(a) Profile in focal point. (b) Profile at 50 mm from focal point. (c) Profile at 100 mm from focal point.

Figure D.4: Circularised beam profiles of the focussed beam out of the processing optic at several location of the focal point. Scales are in μm with $200 \mu m$ ticks.



(a) Single reflection



(b) 'Bouncing' reflections

Figure D.5: Photo's of the split beam hitting a piece of paper.

D.3 Analog control signal

During testing with the laser modules using the FieldMax II-TO power meter, it was noticed that they did not conform to the analogue control parameters stated in the specifications (table D.1 left). After some testing, the actual parameters were discovered (table D.1 right). These values indicate that the 2-watt laser has a maximum power of 1300 mW, which is still sufficient since 500 mW was specified, and that the 4-w module has its full rated power. However the problem with the 4-watt module is the very small control window (0-1 V) which makes it very easy to start fires with a 0.1 V adjustment capable power supply.

Another aspect to be discussed, is that the circular cut-out blocks a significant amount of power from being emitted into the optical system. The amount of power emitted into the system has been plotted in figure D.6.

Table D.1: Specified and actual control parameters of the laser modules

Stated model	Specified		Actual	
	2 watt	4 watt	2 watt	4 watt
Analogue control signal (V)	0-5	0-5	0.1-5	0-1
Power emitted (W)	0-2	0-4	0-1.3	0-4

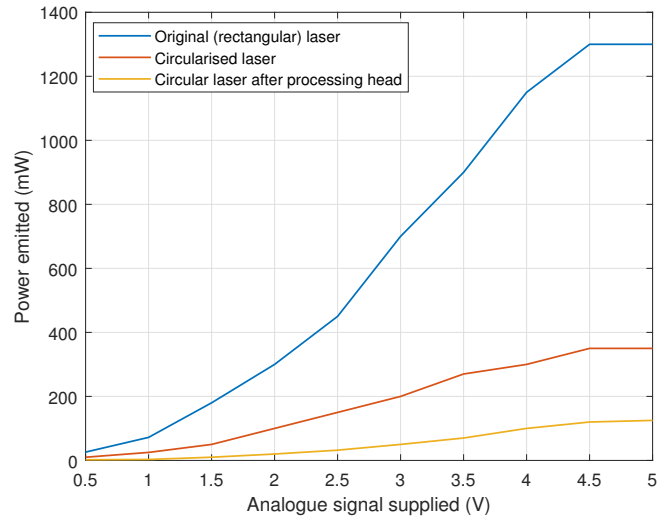


Figure D.6: Relation of voltage against emitted power for several situations